(1)

CHARACTERIZATION OF $AgGaSe_2$ AND $ZnGeP_2$ FOR FREQUENCY DOUBLING CO_2 LASER OUTPUT

THESIS

Monte D. Turner, Captain, USAF

AFIT/GEP/ENP/90D-10

DEPARTMENT OF THE AIR FORCE
AIR UNIVERSITY
AIR FORCE INSTITUTE OF TECHNOLOGY
Wright-Patterson Air Force Base, Ohio

AFIT/GEP/ENP/90D-10

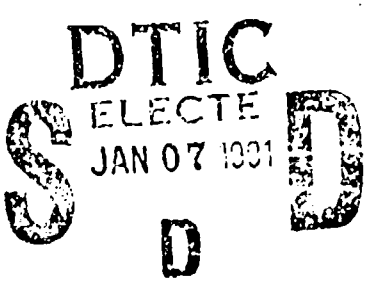

CHARACTERIZATION OF $AgGaSe_2$ AND $ZnGeP_2$ FOR FREQUENCY DOUBLING CO_2 LASER OUTPUT

THESIS

Monte D. Turner, Captain, USAF

AFIT/GEP/ENP/90D-10

Approved for public release; distribution unlimited

AFIT/GEP/ENP/90D-10

CHARACTERIZATION OF $AgGaSe_2$ AND $ZnGeP_2$ FOR FREQUENCY DOUBLING CO_2 LASER OUTPUT

Thesis

Presented to the Faculty of the School of Engineering

of the Air Force Institute of Technology

Air University

In Partial Fulfillment of the

Requirements for the Degree of

Master of Science in Engineering Physics

Monte D. Turner, B.S.

Captain, USAF

September 1990

Preface

The purpose of this study was to characterize the performance of two types of nonlinear optical crystals in their use for producing the second harmonic of 10.6 μm radiation. The crystals and laboratory facilities were provided by the Wright Research and Development Center's Electro-Optics Sources Branch, Wright Patterson AFB, Ohio.

The computational work in preparation for the experiments led to the optimal designs for characterizing each of the crystals. The results of this analysis showed that $AgGaSe_2$ has promise as a high efficiency source of doubled 10.6 μm radiation, while $ZnGeP_2$ may be more suited for other applications such as optical parametric oscillation. The work should be continued with $AgGaSe_2$ in order to more fully understand the damage mechanisms near the points of peak performance.

In performing this work, I have had a great deal of help from several individuals. I wish to thank my faculty advisor, Dr. Won B. Roh, for his guidance and assistance throughout the effort. I am very grateful to my sponsor, Dr. Kenneth L. Schepler, Wright Research Development Center Electro-Optic Sources Branch, for his direction and enthusiastic support as the work progressed. To Dr. Paul Schrieber, I owe a debt of gratitude for his help in providing insightful comments and instructing me on the use of the instrumentation. Thanks go to Gail Brown and Capt. Ges Seiger of WRDC/MLPJ for their response in spectrally characterizing the crystals and other samples. A word of thanks is owed to Robert Wade and Art Becraft for their efforts and patience in fabricating a number of components, and to Virginia MacMillan for running several FTIR scans as well. Finally, I wish to thank my family and friends for helping me to maintain a bit of sanity over the course of these past few months.

Monte D. Turner

Table of Contents

List of Figures

List of Tables

Abstract

This experiment was to characterize the nonlinear performance of $AgGaSe_2$ and $ZnGeP_2$ for frequency doubling CO_2 laser output at 10.6 μm. The experiments included a series of theoretical estimates of the source and crystal performance to define the measurements to be performed. The parameters of interest were the phase matching angles, angular acceptance, conversion efficiency and damage thresholds. The 9mm × 9mm × 29mm antireflection coted sample of $AgGaSe_2$, with a phase matching angle of $\theta = 55.02^0$ and an internal acceptance bandwidth $\Delta\theta = 0.298^0$, achieved a maximum second harmonic conversion efficiency of 20.7%. Surface damage limited the improvement of the efficiency and the threshold for the coated surface was near $4.5kW/cm^2$. Further studies were conducted using small witness samples from the crystal boule. For the case of the uncoated sample of $ZnGeP_2$, the theoretical computations point out that the performance will be poor at best due to an extremely small effective nonlinear coefficient at the temperature tuned phase matching angles. These calculations are presented though no second harmonic was observed during these experiments. Improvements to the experimental designs and theoretical estimates are cited for continued work with both of these crystals.

CHARACTERIZATION OF $AgGaSe_2$ AND $ZnGeP_2$ FOR FREQUENCY DOUBLING CO_2 LASER OUTPUT

I. Introduction

High performance and frequency agile laser sources are required for a variety of uses in optical systems and applications. Non-linear optical materials provide a means to extend the utility of these sources by converting the output frequencies from known laser systems to other regions of the optical spectrum. The carbon dioxide laser is a particularly mature technology whose high output efficiency makes it an attractive candidate for frequency conversion. There is a significant interest in the mid-infrared region near 5 μm due to a natural transmission window in the earth's atmosphere and applications in spectroscopy and remote sensing.

In the development of non-linear optical materials, their utility in the mid and far infrared regions have been limited by transmission losses due to absorption and scattering. Select materials from a class known as the chalcopyrites have been used to demonstrate second harmonic generation across a wide band of the infrared spectrum (19:1). With a relatively low intrinsic absorption in this region, scattering losses resulting from the crystal growth techniques have limited their ultimate usefulness. Recently, silver gallium selenide and zinc germanium phosphide, have been grown in a manner which significantly reduces these losses by Cleveland Crystals under contract to the Wright Research Development Center's Electro-Optic Sources Branch, Wright Patterson AFB, Ohio. Characterization of second harmonic generation using these materials is required for comparison of their relative figures of merit.

These figures of merit include conversion efficiency, angular acceptance, phase matching

angle and damage threshold. The measurements taken will provide an estimate of their usefulness in high average power frequency conversion from repetitively pulsed laser sources.

In this research, theoretical estimates of the conversion efficiency will be made using published values of the nonlinear coefficients, phase matching angles and damage limits along with measured characteristics of the pump source in order to specify the physical parameters of the experiments. Deviations in the actual measurements will highlight the differences between the present and published values as well as the shortcomings in the mathematical models employed.

The sample of $AgGaSe_2$ (9mm × 9mm × 29mm), anti-reflection coated for 10.6 and 5.3 μm, will be characterized in terms of the phase-matching angle, angular acceptance and conversion efficiency for the focussed and non-focussed cases. The uncoated sample of $ZnGeP_2$ (6.2mm × 6.2mm × 11mm) will be characterized in terms of the phase-matching angle at a given temperature, angular acceptance and conversion efficiency for the focussed case only. The repetitively pulsed CO_2 laser source provides a very stable TEM_{00} output where the temporal profile of the pulses are Gaussian. The measured efficiencies will be compared with calculations involving the measured crystal properties and literature values of the nonlinear coefficient. Finally, damage thresholds for $AgGaSe_2$ will be investigated using two 9mm × 9mm × 2mm witness samples which are coated on one side only. The threshold for damage will be related in terms of peak and average intensities for both surfaces of these samples.

This document is organized to provide the reader with sufficient background to appreciate the mathematical developments as well as the intricacies of the experiment procedures and results. Chapter II introduces the theory of nonlinear optics and the application to the phase matched conditions of second harmonic generation. The next chapter involves the characterization of the CO_2 laser source and both nonlinear crystals. Theoretical estimates of the crystals' performance follows in Chapter IV. These results are used to specify the experimental

set-ups for the non-focussed and focussed efficiency measurements and are enumerated in Chapter V. The results and discussion are presented in Chapter VI with a comprehensive Summary and Suggestions/Recommendations in the concluding chapters. Background theory of linear optics in anisotropic materials is found in Appendix A. Appendix B describes a program developed to numerically evaluate one of the theoretical estimates of second harmonic generation conversion efficiency.

II. Theory of Nonlinear Optics

In the theory of nonlinear optics, the material's response to an incident electromagnetic field, or the instantaneous polarization of the medium, will be expanded to include both the linear and nonlinear effects. In considering the linear theory of propagation of light through a medium, its speed is defined by the index of refraction of the material. In an isotropic media this value is independent of both the polarization of the light and its direction of travel. In an anisotropic medium however, the incident radiation is broken into two orthogonally polarized components whose speeds (or indices of refraction) will vary with direction. The magnitude of the variation is determined by the material properties and will correspond to the two solutions of the Fresnel equations in the medium. A review of linear anisotropic theory is found in Appendix A.

The instantaneous polarization of an anisotropic medium may be expressed in a Taylor series which includes the linear susceptibility, χ_{ij}. In tensor notation, this appears as,

$$P_i = \varepsilon_0 \chi_{ij} E_j + 2\varepsilon_0 \chi_{ijk} E_j E_k + 4\varepsilon_0 \chi_{ijkl} E_j E_k E_l + \ldots, \qquad (2.1)$$

where P_i is the ith component of the instantaneous polarization and E_i is the ith component of the instantaneous field (23:504). The linear susceptibility is shown as the first term in Eq.(2.2), while the second is the nonlinear term responsible for second harmonic generation and is generally written as $d_{ijk} = \varepsilon_0 \chi_{ijk}$. In this development, the third term in the expansion, which gives rise to such interesting effects as phase conjugation and third harmonic generation, can be considered negligible.

Note the second order term is dependent on the presence of the two field terms which will both be of the general form in Eq.(2.2). We represent the first field at ω_1 as

$$E_j^{\omega_1}(t) = \mathrm{Re}\left(E_j^{\omega_1} e^{i\omega_1 t}\right) = \frac{1}{2}\left(E_j^{\omega_1} e^{i\omega_1 t} + \mathrm{c.c.}\right) \qquad (j = x,y,z) \qquad (2.2)$$

where i, j and k refer to the field components along the principal axes x, y and z respectively. The field $E_k^{\omega_2}$ may be written similarly. If the medium is nonlinear in response, the fields will give rise to polarizations at the sum and difference frequencies of the input fields, $P_i^{\omega_3 = \omega_1 \pm \omega_2}(t)$. Restricting our attention to the case of second-harmonic generation where $\omega_1 = \omega_2$, the resulting cross terms of the complex conjugates will vanish and the second order nonlinear polarization will be

$$P_i^{2\omega} = d_{ijk} E_j^{\omega} E_k^{\omega} \tag{2.3}$$

for Type I phase matching (to be covered later). Note that the degeneracy due to the frequencies being equal is compensated by a factor of one half in Eq.(2.2) above. The second order nonlinear susceptibility tensor considered here is not a frequency dependent function and is a material dependent property often measured by second harmonic generation experiments. Since no physical significance can be assigned to changing the order of j and k in Eq.(2.3) (23:507), the second order tensor may be contracted to 18 independent elements by assuming the convention below. Note in Eq.(2.3) that although the contraction of the indices does not change the polarization, the order to the field terms themselves in the tensor notation is very important.

$$xx = 1, \qquad yy = 2, \qquad zz = 3, \tag{2.4}$$
$$yz = zy = 4, \qquad xz = zx = 5, \qquad xy = yx = 6.$$

The resulting d_{ij} forms a 3×6 matrix that operates on the crossed terms of the incident field for Type I phase matching as

$$\begin{pmatrix} P_x \\ P_y \\ P_z \end{pmatrix} = \begin{pmatrix} d_{11} & d_{12} & d_{13} & d_{14} & d_{15} & d_{16} \\ d_{21} & d_{22} & d_{23} & d_{24} & d_{25} & d_{26} \\ d_{31} & d_{32} & d_{33} & d_{34} & d_{35} & d_{36} \end{pmatrix} \begin{pmatrix} E_x^2 \\ E_y^2 \\ E_z^2 \\ 2E_yE_z \\ 2E_xE_z \\ 2E_xE_y \end{pmatrix} \tag{2.5}$$

Both of the crystals considered in this analysis fall into the crystal point group $\bar{4}2m$ where the only nonzero components are d_{14}, d_{25}, and d_{36}, where $d_{14} = d_{25}$. We now have a description of the physical properties of the material given the direction of propagation and polarization of the input field.

Interaction of Light and the Nonlinear Medium

Below, we will develop a set of expressions which quantify the interaction between the input radiation frequencies and the medium in setting up time dependent polarizations along the three coordinate axes. Consider Maxwell's equation (Eq.(A.8 - 11)) written in the form that incorporates the polarization explicitly

$$\nabla \times \vec{H} = \vec{J} + \frac{\partial}{\partial t}(\varepsilon_0 \vec{E} + \vec{P}) \tag{2.6}$$

$$\nabla \times \vec{E} = -\frac{\partial}{\partial t}(\mu_0 \vec{H}) \tag{2.7}$$

where $\vec{P} = \varepsilon_0 \chi_L \vec{E} + \vec{P}_{NL}$ and the linear susceptibility is treated as a scalar quantity and the nonlinear polarization term is taken as the second term in Eq.(2.1). Following the development in Yariv (23:516) we rewrite Eq.(2.7) as

$$\nabla \times \vec{H} = \sigma \vec{E} + \frac{\partial}{\partial t} \varepsilon \vec{E} + \frac{\partial \vec{P}_{NL}}{\partial t} \tag{2.8}$$

where the nonlinear polarization term may be written $(P_{NL})_i = 2d'_{ijk} E_j E_k$. The prime on the second order susceptibility indicates that this is a variable transformed to coincide with the direction of propagation with respect to the principal coordinate system. It is known as the effective nonlinear coefficient, d_{eff}. The current density has been rewritten in terms of the conductivity, σ, and may be regarded as a frequency dependent loss term. It may or may not

be included in developments to predict overall second harmonic generation efficiency. Taking the curl of both sides of Eq.(2.8) and replacing $\nabla \times \vec{H}$ with Eq.(A.11) along with the vector identity $\nabla \times \nabla \times \vec{E} = \nabla\nabla \cdot \vec{E} - \nabla^2\vec{E}$, yields

$$\nabla^2\vec{E} = \mu_0\sigma\frac{\partial\vec{E}}{\partial t} + \mu_0\varepsilon\frac{\partial^2\vec{E}}{\partial t^2} + \mu_0\frac{\partial^2}{\partial t^2}\vec{P}_{NL} \tag{2.9}$$

If we restrict the problem to the one dimensional case of propagation along the z-axis, the partial derivatives with respect to the x and y axes may be neglected. Considering the solutions along the three coordinate axes, where ω_1, ω_2 and ω_3 represent the frequencies, the corresponding fields in the form of travelling waves appear

$$\begin{aligned} E_i^{\omega_1}(z,t) &= \frac{1}{2}\left[E_{1i}(z)e^{i(\omega_1 t - k_1 z)} + \text{c.c.}\right] \\ E_k^{\omega_2}(z,t) &= \frac{1}{2}\left[E_{2k}(z)e^{i(\omega_2 t - k_2 z)} + \text{c.c.}\right] \\ E_j^{\omega_3}(z,t) &= \frac{1}{2}\left[E_{3j}(z)e^{i(\omega_3 t - k_3 z)} + \text{c.c.}\right] \end{aligned} \tag{2.10}$$

where the subscripts *i, j, k*, refer to the cartesian coordinate system (and may take on the values x and y) whose orientation with respect to the principal axes is accounted for by d_{eff}. The specific form of the *i*th component of the nonlinear polarization term at frequency ω_1 given the form of the travelling waves in Eq.(2.2) is

$$\left[P_{NL}^{(\omega_1)}(z,t)\right]_i = d_{ijk}E_{3j}(z)E_{2k}^{*}(z)e^{i[(\omega_3-\omega_2)t-(k_3-k_2)z]} + \text{c.c.} \tag{2.11}$$

The conservation of energy condition, $\omega_3 = \omega_1 + \omega_2$, is valid for all time *t*, and the operations specified in Eq.(2.9) may be carried out noting that the second derivative terms with respect to the spatial coordinate z are very small. The wave equation above must be satisfied by each of the three field components separately, where the form of the nonlinear polarization is Eq.(2.11), the result is

$$\frac{dE_{1i}}{dz} = -\frac{\sigma_1}{2}\sqrt{\frac{\mu_0}{\varepsilon_1}}E_{1i} - i\omega_1\sqrt{\frac{\mu_0}{\varepsilon_1}}d'_{ijk}E_{3j}E^*_{2k}e^{-i(k_3-k_2-k_1)z}$$

$$\frac{dE_{2k}^*}{dz} = -\frac{\sigma_2}{2}\sqrt{\frac{\mu_0}{\varepsilon_2}}E^*_{2k} + i\omega_2\sqrt{\frac{\mu_0}{\varepsilon_2}}d'_{kij}E_{1i}E^*_{3j}e^{-i(k_1-k_3+k_2)z} \qquad (2.12)$$

$$\frac{dE_{3j}}{dz} = -\frac{\sigma_3}{2}\sqrt{\frac{\mu_0}{\varepsilon_3}}E_{3j} - i\omega_3\sqrt{\frac{\mu_0}{\varepsilon_3}}d'_{jik}E_{1i}E_{2k}e^{-i(k_1+k_2-k_3)z}$$

This set of equations accounts for the interaction between the three fields within the media and covers all second order interactions. An alternate development would attack the problem from the aspect of the amount of energy delivered to the medium by each field as a function of time and space. Second harmonic generation is the special case where the two input frequencies are identical. These set up a nonlinear polarization at twice their value leading to a dipole radiation term at ω_3.

Optical Second Harmonic Generation

Consider the last of Eqs.(2.38) for the case of no absorption at the third frequency, $\sigma_3 = 0$, and identical input fields such that $\omega_1 = \omega_2$ and $\omega_3 = 2\omega_1$. In the initial development, we can also assume that the fields at the input frequencies are not significantly diminished by conversion to the second harmonic and thereby drop their dependence on z and write

$$\frac{dE_{3j}}{dz} = -i\frac{1}{2}\omega_3\sqrt{\frac{\mu_0}{\varepsilon_3}}d'_{ijk}E_{1i}E_{1k}\exp[i(k_3^{(j)} - k_1^{(i)} - k_1^{(k)})z] \qquad (2.13)$$

The factor of one half comes from the development of d_{eff} previously for the case of second harmonic generation. $k_1^{(i)}$ is the propagation constant for the beam at ω_1 which is polarized along the direction i. Recall that the anisotropic medium will separate the incident radiation into two eigenpolarization modes. In general, the input frequency will be a linear superposition of the two where the superscripts on k indicate that the magnitudes will depend on these

polarizations states.

Assuming a crystal of finite length, L, integrating Eq.(2.13), for the case of no initial second harmonic, $E_{3_j}(0) = 0$, the result is

$$E_{3_j}(L) = -i\frac{1}{2}\omega_3\sqrt{\frac{\mu_0}{\varepsilon_3}}d'_{ijk}E_{1_i}E_{1_k}\frac{e^{i\Delta k z}-1}{i\Delta k} \tag{2.14}$$

where $\Delta k = k_3^{(j)} - k_1^{(i)} - k_1^{(k)}$ and is often called the phase mismatch. The repeated indices indicate summations and in general there will be four separate terms in Eq.(2.14). In order to eliminate the complex terms in this equation and reduce it to a more tractable form, we can generally need only consider the two cross terms, d'_{jik} and d'_{jki} $(i \neq k)$. They will dominate the nonlinear optical tensor due to either to the phase matching conditions or large nonlinear coefficients. Multiplying both sides by the complex conjugate, recognizing the symmetry of the nonlinear tensor and the trigonometric form of the last term, the equation may be rewritten in terms of real variables

$$E^*_{3_j}(L)E_{3_j}(L) = \frac{4\mu_0}{\varepsilon_3}\omega_1^2(d'_{ijk})^2E_{1_i}^2E_{1_k}^2L^2\frac{\sin^2\frac{1}{2}\Delta kL}{\left(\frac{1}{2}\Delta kL\right)^2} \tag{2.15}$$

where $i = x$, $k = y$ (or $i = y$, $k = x$), and there is no summation over the repeated indices. Also note the fundamental frequency has been included in this equation.

In terms of power over a specified area, we may use the expression derived from the time averaged Poynting theorem

$$\frac{P^{(2\omega)}}{\text{area}} = \frac{1}{2}\sqrt{\frac{\varepsilon_3}{\mu_0}}E_{3_j}E^*_{3_j} \tag{2.16}$$

Inserting Eq.(2.14), this expression becomes

$$\frac{P_j^{(2\omega)}}{area} = 2\sqrt{\frac{\mu_0}{\varepsilon_3}}\omega_1^2(d'_{ijk})^2E_{1_i}^2E_{1_k}^2L^2\frac{\sin^2\frac{1}{2}\Delta kL}{\left(\frac{1}{2}\Delta kL\right)^2} \tag{2.17}$$

Finally, in terms of intensity, for the case when input power is divided equally between the two input fields at the same frequency, the result is

$$P^{(2\omega)} = 2\left(\frac{\mu_0}{\varepsilon_0}\right)^{\frac{3}{2}} \frac{\omega_1^2 (d_{ijk})^2 L^2}{n^3} \left(\frac{(P^{(\omega)})^2}{\text{area}}\right) \frac{\sin^2 \frac{1}{2}\Delta kL}{\left(\frac{1}{2}\Delta kL\right)^2} \tag{2.18}$$

where $\varepsilon_1 \cong \varepsilon_3 \cong \varepsilon_0 n^2$.

This expression yields the amount of power developed in the second harmonic for a continuous input beam at the fundamental frequency with no depletion or absorption. It inherently assumes the intensity level is constant across the beam and that the there is no deviation of the two fields over the length of the crystal (no walkoff). In Chapter IV, more rigorous developments will incorporate some or all of these additional considerations.

In all cases, the amount of second harmonic generated is limited by the finite coupling of the input field to the dipole nature of the crystalline material, and to the manner in which the microscopic fields add to create the output beam.

Phase Matched Conditions

For the maximum power to be generated, the phase mismatch in Eq.(2.18) must be zero, i.e. $\Delta k \equiv 0$. If $\Delta k \neq 0$, the field generated at one point within the crystal will be out of phase with that of another, resulting in an interference between the wavefronts described by the $sinc^2$ term. This may arise for a number reasons including deviations in angle, temperature fluctuations, divergence of the input beam and a finite wavelength bandwidth of the source. Recalling the definition of Δk in terms of the indices of refraction (assuming $\omega_1 = \omega_2$ and dropping the sub-scripts)

$$\Delta k = k^{(2\omega)} - 2k^{(\omega)} = \frac{2\omega}{c}(n^{(2\omega)} - n^{(\omega)}) \tag{2.19}$$

Since the index of refraction generally increases with frequency, we would ideally seek a situation where the difference between the two indices is a minimum.

If we note the representation of the index surfaces for the fundamental and the second harmonic in a uniaxial crystal, Figure 1, we see that two of the ellispes intersect at a certain

angle denoted as θ_m. These ellipses are plotted for the case of a negative uniaxial crystal ($n_e < n_o$) and it can be seen that the ordinary index of refraction for the fundamental is equal to the extraordinary index of refraction of the second harmonic at this angle.

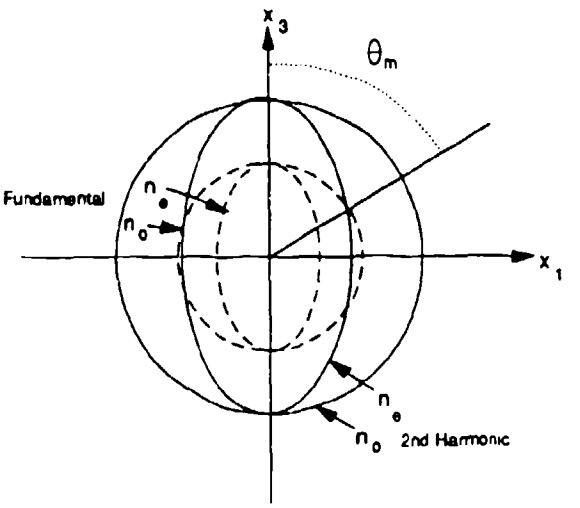

Figure 1. Phase matching condition in a negative uniaxial crystal shown in the x_1-x_3 plane (22:213). θ_m is the phase matched angle.

If we were to propagate a beam at this angle with respect to the principal axis x_3 inside the crystal, polarized perpendicular to this axis (recall, the polarizations are susceptible to the index of refraction along the axis parallel to the electric field, here the ordinary index), the orthogonal polarization at the second harmonic would have an index of equal magnitude. This is known as the phase matched angle.

Figure 1 is an example of Type I phase matching for second harmonic generation in a negative uniaxial crystal. The two input fields possess the same polarization, along x_1 (or x_2), and the output is orthogonal to both. If the two fields were input at orthogonal polarizations, and the output was parallel to either of them, it would be called Type II. Type III is very similar, where the output would fall on the other polarization. Both of the crystals characterized is in this analysis are capable of Type I phase matching only given the fundamental wavelength of

10.6 μm.

We may rewrite the equation for the extraordinary index of refraction in the uniaxial crystal in a parametric form related to the angle of propagation with respect to the optic axis (x_3), θ, for either of the two frequencies as follows

$$\frac{1}{n_e(\theta)^2} = \frac{\cos^2\theta}{n_o^2} + \frac{\sin^2\theta}{n_e^2} \tag{2.20}$$

For the case of Type I phase matching in a negative uniaxial crystal, we can equate Eq.(2.20), written for 2ω, with $1/(n_o^{(\omega)})^2$ to yield (22:213)

$$\sin^2\theta_m = \frac{(n_o^{\omega})^{-2} - (n_o^{2\omega})^{-2}}{(n_e^{2\omega})^{-2} - (n_o^{2\omega})^{-2}} \tag{2.21}$$

where θ_m is the phase matched angle. For the case of positive uniaxial crystals this becomes

$$\sin^2\theta_m = \frac{(n_o^{2\omega})^{-2} - (n_o^{\omega})^{-2}}{(n_e^{\omega})^{-2} - (n_o^{\omega})^{-2}} \tag{2.22}$$

The coupled wave equations bear out the fact that the input at the fundamental and the output at the second harmonic are orthogonally polarized for Type I phase matching, but a mechanical argument related to the dipole oscillators is in order (Note Figure 2). The calculated solutions for the specific cases of the materials to be characterized will be carried out in the next chapter.

The fundamental polarization is parallel to the dipole polarization and induces an oscillation in this plane at twice the natural frequency. Since dipole oscillators radiate a polarization perpendicular to their axis and since the two frequencies travel at the same speed (same index) through the medium, a coherent constructive field is built up. In all other directions the oscillations produce fields that destructively interfere and are not observed.

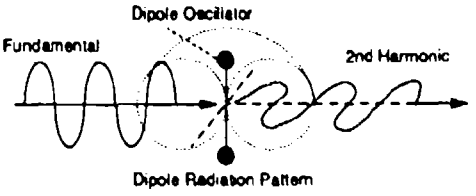

Figure 2. Dipole oscillator diagram, showing excitation parallel to the input polarization direction and the induced oscillation producing the output at the orthogonal polarization.

Figures of Merit

With a basic understanding of the theory of second harmonic generation in hand, it is now possible to begin a comparison of various materials in terms of their relative performance characteristics.

The effective nonlinear coefficient is dependent upon the nonlinear optical tensor and the direction of propagation through the medium. The specifics of its derivation are covered in Chapter IV.

The angular sensitivity, β_θ, relates the rate with which the second harmonic rolls off with a change in angle. These are found by retaining the first two terms in Taylor series expansion of Eq.(2.19) with Eq.(2.20) inserted for $n_e(\theta)$ given Type I phase matching.

$$\Delta k(\theta)L = 2\beta_\theta(\theta - \theta_m) \tag{2.23}$$

$$\beta_\theta = \frac{-\omega L}{c}\sin(2\theta_m)\frac{(n_e^{2\omega})^{-2} - (n_o^{2\omega})^{-2}}{2(n_o^{\omega})^{-3}}\text{, negative uniaxial} \tag{2.24}$$

$$\beta_\theta = \frac{-\omega L}{c}\sin(2\theta_m)\frac{(n_e^{\omega})^{-2} - (n_o^{\omega})^{-2}}{2(n_o^{2\omega})^{-3}}\text{, positive uniaxial} \tag{2.25}$$

The angular acceptance at the phase matching condition can be related to the full width at half the maximum values of the $sinc^2$ term in Eq.(2.18). The angular bandwidth can be found as twice the angle in radians which satisfies the parametric relation

$$P^{(2\omega)} \propto \frac{\sin^2 \beta_\theta(\theta - \theta_m)}{[\beta_\theta(\theta - \theta_m)]^2} = \frac{1}{2} \tag{2.26}$$

The walkoff angle between the fundamental and second harmonic in a uniaxial crystal may be expressed as

$$\tan \rho = \frac{1}{2}[n_e(\theta)]^2 \left[\frac{1}{n_E^2} - \frac{1}{n_O^2} \right] \sin 2\theta \tag{2.27}$$

where $n_e(\theta)$ is found from Eq.(2.20) and n_E and n_O are found from the Sellmeier equations for the material. In a negative uniaxial crystal, the second harmonic will deviate from the propagation direction by this angle and for a positive uniaxial crystal, it will be the fundamental.

The measured conversion efficiency, $P^{(2\omega)}/P^{(\omega)}$, will be dependent upon these parameters as well as the physical arrangement of the experiment. It is a sensitive function of the different terms contributing to the phase mismatch, intensity, focussing and the crystal properties such as absorption.

This review of the basic nonlinear theory provides a basis upon which we can develop an understanding of the experimental results.

III. Experimental Apparatus and Source Characterization

It is imperative in the theoretical predictions of the conversion efficiency, as well as the other figures of merit, that the values used to describe the physical nature of the laser beam at the fundamental wavelength and the crystal be as accurate as possible. With these parameters in hand, we are able to specify the optimum experimental arrangements for the various measurements. In addition, deviations between the experimental and theoretical values will point out shortcomings in the calculations or errors in the experimental procedure. For this reason, the experimental results of the source and crystal measurements which are used to derive the estimates of efficiency in the following chapters are presented below.

Detectors and Stages

A number of different detectors were used in this series of experiments which will be reviewed here for the sake of reference in later sections.

Continuous wave power measurements and short duration repetitively pulsed energy measurements were conducted using Scientech Model 365 one inch diameter surface absorbing disc calorimeters. The analog meters provided a 0.001 to 10 Watt (or Joule) operating range. At the lower power or energy ranges, isothermal enclosures were used to minimize the fluctuations in the measurements due to air currents in the laboratory. The surface absorbers were coated with Nextel black paint which provided a flat spectral response for all wavelengths under study in the experiment.

Temporal measurements of the repetitively pulsed fundamental and second harmonic were made using a pair of liquid nitrogen cooled resonant cavity HgCdTe detectors. The detectors and preamplifiers were originally designed for heterodyned measurements and have a bandwidth on the order to 100 MHz. With the resonant cavity design, the detectors were relatively insensitive to wavelengths other than those of interest. The outputs were captured with a 200 MHz bandwidth digital oscilloscope.

An Infrared Systems Model 700 room temperature pyroelectric vidicon camera was used to record the spatial profile of the fundamental and second harmonic beams. The vidicon tube (210x150 effect elements) is sensitive from 2μm to 20μm and has a dynamic range of 0 to 256 (8 bits, 7 useful). The camera employs a 25 Hz chopper to modulate the input beam for the pyroelectric array and an electronic suppression of this frequency. The camera is controlled via a Big Sky Software, Beamcode, IBM computer based system. Data acquired with this camera was useful for relative measurements only. It proved notoriously unreliable in performing absolute measurements on the continuous or repetitively pulsed laser source. It was able to provide a basis for judging beam and mode quality of the laser in any case.

The mechanical stages used for angular adjustments in these experiments provided sub-minute of arc accuracy and could be arranged to control any desired axis of rotation. Relative adjustments with linear translation and elevation stages were accurate to within 0.1 mm along all axes of interest.

CO_2 Laser Source & Output Characterization

The carbon-dioxide laser source used in these experiments provided continuous wave and repetitively pulsed output from an actively controlled frequency stabilized local oscillator / main amplifier design. A schematic diagram of the optical system is shown below in Figure 3. The laser is actually a comprised of two separate lasers for frequency control and power stability followed by a single pass four channel waveguide amplifier. Together they provide a high average power repetitively pulsed output beam with good mode quality and frequency stability.

On the lower left side of Figure 3, the local oscillator is a very short (14.5 cm) grating tuned cavity, 135 *l*/mm, which is tuned for the center of the *P(20)* line of CO_2. The cavity length of the oscillator is varied to maintain a resonance at 60 Mhz off of line center. At this offset, the output power is a very sensitive function of cavity length. The error signal generated to drive the piezoelectrically controlled mirror mount comes from the comparison of the detector output near the local oscillator's output port to a set reference level.

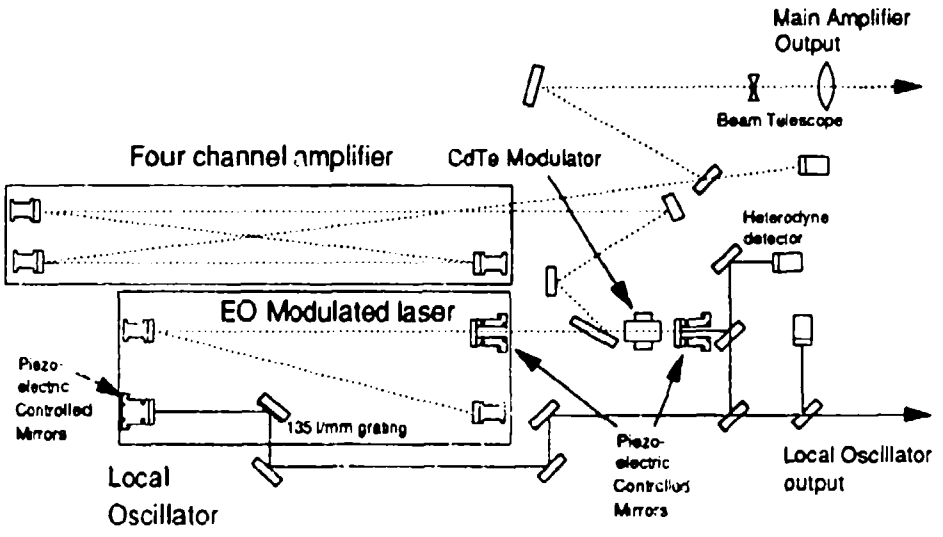

Figure 3. Schematic diagram of the CO_2 laser source. There are two separate lasers present; the grating tuned local oscillator and the electro-optically modulated amplifier / coupled cavity laser. The output from the EO-Modulated laser then passes through a four channel waveguide amplifier to the beam telescope and exits the system.

Part of the local oscillator's output is also split off to act as the frequency standard for the rest of the system while the rest exits the housing as a horizontally polarized beam.

The second laser provides the basis for the electro-optically modulated output via the intra-cavity CdTe modulator. The folded amplifier is approximately 70 cm in length where the intermediate mirror is mounted on a piezoelectrically controlled stage. The output passes into the coupled cavity through the 45% reflective ZnSe window prior to the CdTe modulator. At this point the beam is horizontally polarized and after passing through the modulator twice, the beam is vertically polarized and is sheared off by the germanium polarizer/coupler.

A small amount of the beam leaks through the high reflector in the coupled cavity to the mixed with the output from the local oscillator. The two beams are detected via heterodyning where a constant offset frequency of the local oscillator provides the error signal to the inter-

mediate cavity mirror's stage. The long term output frequency stability is maintained to within 30 MHz of the *P(20)* line. The optimum output power is maintained by the output of the pyroelectric detector after the four channel amplifier. A small dither is placed on the rear coupled cavity mirror and the error signal provides the signal for the piezoelectric stage.

The beam goes through a series of mirrors prior to passing through the four channel waveguide amplifier and existing the system through a Cassegrain beam expanding telescope. Note in Figure 3, the dotted line traces the path of the main output beam from its origin within the electro-optically modulated cavity through the output port.

The vertically polarized output beam has an average power of approximately 8 Watts CW and 7 W when modulated at 30 kHz. The output mode is TEM_{00} except for a slightly elliptic nature caused by the beam combining elements within the cavity. Two other modulation frequencies were available, 50 and 100 kHz, but not often used due to lower peak powers (though higher average powers).

Polarization of the Laser Source. The polarization of the main amplifier and the local oscillator were measured by rotating an infrared polarizer of known polarization through a 180^0 arc and noting the variation in power. According to Malus' Law, the variation can be fit to a cosine of the angle of orientation of the polarizer with respect to input beam. Both of the beams were attenuated to approximately 10 mW in order to avoid damage to the very fine grid of gold wires held between a pair of germanium windows that made up the polarizer.

According to the design of the overall laser system, the two output beams should be orthogonally polarized. As can be seen in Figure 4, the polarization of the local oscillator is approximately 15^0 off of horizontal. This does not pose a problem in the heterodyning detection inside the cavity because the two beams at that point remain in the same plane of polarization.

The output from the main amplifier is nearly vertically polarized where any small deviation should not significantly effect the amount of properly polarized power delivered to the crystal.

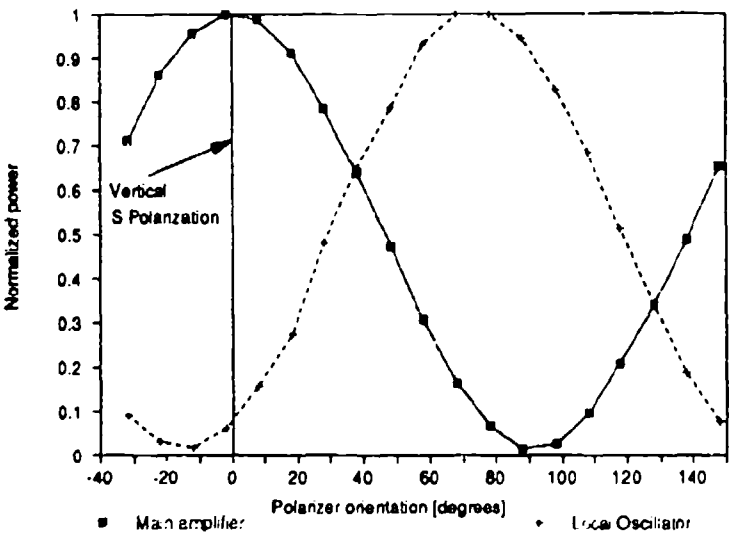

Figure 4. Polarization of the two beams fit to a cosine.

Characterization of the Beam Divergence and the Focussed Spot Sizes. As noted in the development of the phase-matching requirements for second harmonic generation, the phase mismatch, Δk, is a function of the deviation of the input beam from the optimum angle. This can be due to mechanical position or to the divergence of the laser as it passes through the crystal. At the phase-matched angle, the divergence will dominate the phase-mismatch (especially in the focussed case).

Since all of these experiments were conducted near the output port of the laser, measurements of the divergence would have to take into account the fact that we are in the near-field. For this wavelength, the far-field is a least 10 meters from the output port of the laser. Thus, measurements of the beam profile were taken at various distances from the laser and numerically fit to yield an analytic description of the divergence of the beam.

The complex beam parameter, which describes the Gaussian beam as function of wavefront's radius of curvature and the spot size is given as,

$$\frac{1}{q(z)} = \frac{1}{R(z)} - \frac{i\lambda_0}{\pi n w^2(z)} \tag{3.1}$$

This parameter can be used to describe the propagation of a Gaussian beam through an optical system with the appropriate ray transfer matrices.

In this particular arrangement, we assume the location of the beam waist to lie inside the cavity (near the output port of the waveguide amplifier), this is where the radius of curvature goes to infinity, and the complex beam parameter reduces to

$$\frac{1}{q_0} = \frac{-i\lambda_0}{\pi n w_0^2} \tag{3.2}$$

We need only to build the appropriate set of ray transfer matrices which describe the propagation of the beam from the waist to points outside the laser. All of the intervening optics between the beam waist and the output port can be disregarded because we will fit the experimental data with an analytic description. The spot size as a function of distance from the laser is described by

$$w(z) = w_0\sqrt{1 + \left(\frac{\lambda_0 z}{\pi n w_0^2}\right)^2} \tag{3.3}$$

where $z = z_2 + \text{Offset}$. The Offset is the constant distance from the output window of the laser back to the location of the beam waist, w_o, and z_2 is the distance from the laser to the point of interest.

Measurements of the continuous wave beam profiles were taken at different distances from the laser, and the waist radius was determined to be $w_o = 1.019\text{mm}$ where $\text{Offset} = 0.31\text{m}$. For the case of the repetitively pulsed beam, the waist radius was extracted from the measurements of the focussed beam spot sizes.

The spot size formed by the focussing element must be characterized accurately in order to calculate the intensity (irradiance) levels of the beam as a function of the distance from the lens. In this set of measurements, the change in power observed at a fixed position was

recorded as a knife edge is scanned across the horizontal axis of the beam. Having accurately calibrated the motion of the knife edge as a function of time, the spot size at that distance from the lens may be deduced from rate of fall in the observed power. The experimental layout for this method is shown in Figure 5.

Assuming the focussed beam is a two dimensional Gaussian beam, the spatial intensity distribution may be described by

$$I(x,y) = \frac{2P_0}{\pi w^2}\exp\left(-\frac{2x^2 + 2y^2}{w^2}\right) \tag{3.4}$$

where x and y are the axes chosen perpendicular to the beam, w is the spot size, and P_0 is the total laser power (20:2809). If we scan the beam horizontally with the razor blade, the power transmitted will be given by

$$P(x) = \int_{-\infty}^{\infty}\int_{x}^{\infty}\frac{2P_0}{\pi w^2}\exp\left(-\frac{2x^2 + 2y^2}{w^2}\right)dx\,dy \tag{3.5}$$

Integrating out the dependence along the vertical axis of the beam, assumed here to be the y-axis, the equation becomes

$$P(x) = \frac{P_0}{w}\sqrt{\frac{2}{\pi}}\int_{x}^{\infty}\exp\left(-\frac{2x^2}{w^2}\right)dx \tag{3.6}$$

which takes on the form of the error function.

As the knife edge scans across the beam, the power recorded will drop slowly at first as the blade intersects the edge of the pattern and rapidly decrease as it approaches the peak of the pattern. If we are able to easily locate the 90 % and 10 % of total average power points in the decay of the signal recorded, Eq.(2.6) above may be written in terms of this difference in time (or distance). From this distance we can easily extract the 1/e radius of the beam by

$$w = 0.7803 \quad \Delta d_{chart} \cdot v_{chart} \cdot \frac{1}{v_{blade}} \tag{3.7}$$

Δd is the distance on the chart paper it took for the power to drop from the 90% to the 10% level, v_{chart} is the chart paper speed and v_{blade} is the speed of the blade as it cuts through the beam.

Note in the diagram of the experimental apparatus, the razor blade is mounted on the stem of an electrically driven micrometer stage with 0.001 mm incremental distance readout set to a speed of 0.11 mm/sec.

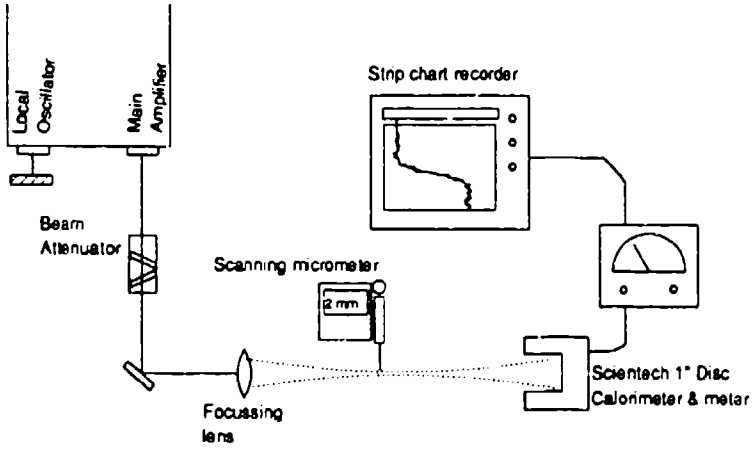

Figure 5. Experimental setup for recording the focussed spot sizes.

The power meter used to record the average power of the beam was a Scientech 1" disk calorimeter with a 0 to 100 mV full range voltage output. The voltage source had a much faster response time than the analog readout (on the order of 100 Hz) and thus allowed a Hewlett-Packard 1175A strip chart recorder to accurately depict the fall in power as the blade passed through the beam and was set to a speed of 15.0 ± 0.01cm/sec.

The separation between the lens and the micrometer stage was varied in 1 mm intervals and the blade was scanned through the beam at each point. With a series of spot sizes in hand it

was only a matter of fitting them with an analytic representation.

Beginning once again with the waist at a known position inside the laser, the spot size as a function of distance from the focussing lens is given by

$$w(z) = \frac{\lambda_0}{\pi w_0}\sqrt{\frac{A^2(\pi w_0^2/\lambda_0)^2 + B^2}{AD - BC}} \tag{3.8}$$

where A, B, C and D refer to the components of the ABCD ray transfer matrix for the Gaussian beam. It is the result of the multiplication of the matrices shown below

$$\begin{pmatrix} A & B \\ C & D \end{pmatrix} = \begin{pmatrix} 1 & z_3 \\ 0 & 1 \end{pmatrix} \begin{pmatrix} 1 & 0 \\ -\frac{1}{f} & 1 \end{pmatrix} \begin{pmatrix} 1 & z_2 + \text{Offset} \\ 0 & 1 \end{pmatrix} \tag{3.9}$$

This last matrix in Eq.(2.9) accounts for the propagation over a distance z_2 from the front of the laser to the lens, through a focussing element of focal length f, and finally a propagation over a distance z_3 to the point of interest (where the razor cut through the focussing beam).

The fit to the measured points is found by varying the f in Eq.(2.9) and w_0 in Eq.(2.10) using the known values of the distances z_2 and z_3. The results of this analysis are shown in Figure 6. Using this same beam waist radius, similar results were achieved for a different lens of a shorter focal length as shown in Figure 7.

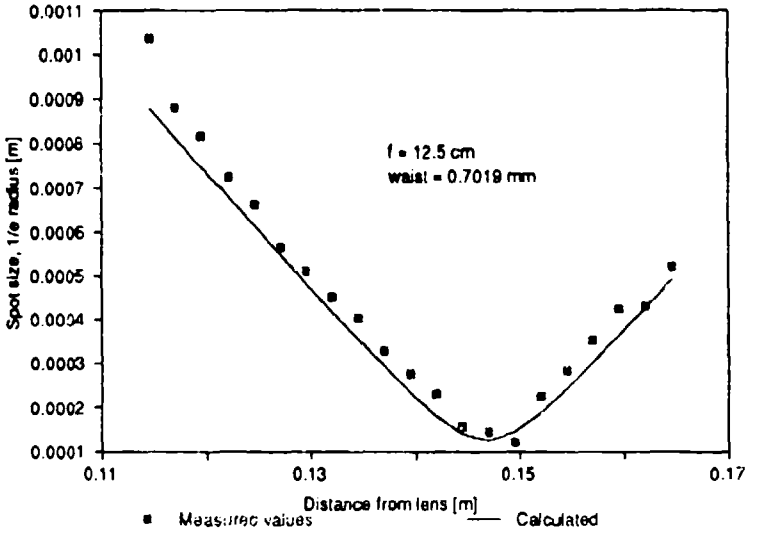

Figure 6. Focussed spot size where $w_0 = 0.7019\text{mm}$ and $f = 12.5\text{cm}$ as a function of distance, z_3, from the lens.

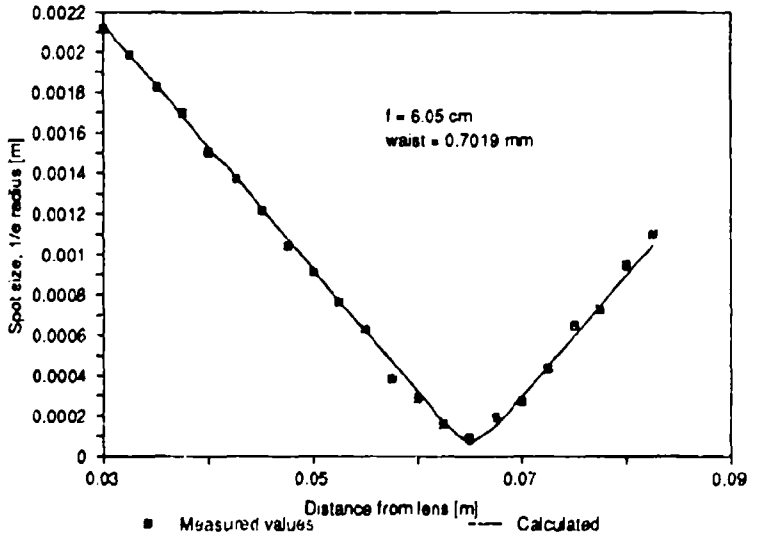

Figure 7. Focussed spot size where $w_0 = 0.7019\text{mm}$ and $f = 6.05\text{cm}$ as a function of distance, z_3, from the lens.

This leads us to consider that the divergence of the laser in the repetitively pulsed mode is larger than the CW mode. Since the measurements of the focussed spot sizes were conducted at a pulse repetition frequency of 30 KHz, and the calculated spot sizes agreed well with the data, the beam waist derived in this analysis will be used in the theoretical estimates of the efficiency. The change in divergence is most likely attributable to the electro-optic modulator in operation (in the CW mode the electric field applied is static).

Pulse Repetition Formats. The CdTe electro-optic modulator preceding the four channel waveguide amplifier allows for three high repetition rate pulsed formats at 30, 50 and 100 kHz. The modulator provides for a smooth Gaussian envelope in time as opposed to the pulse shape of most Q-switched lasers. The temporal profile for the three different pulse repetition frequencies is shown in Figure 8.

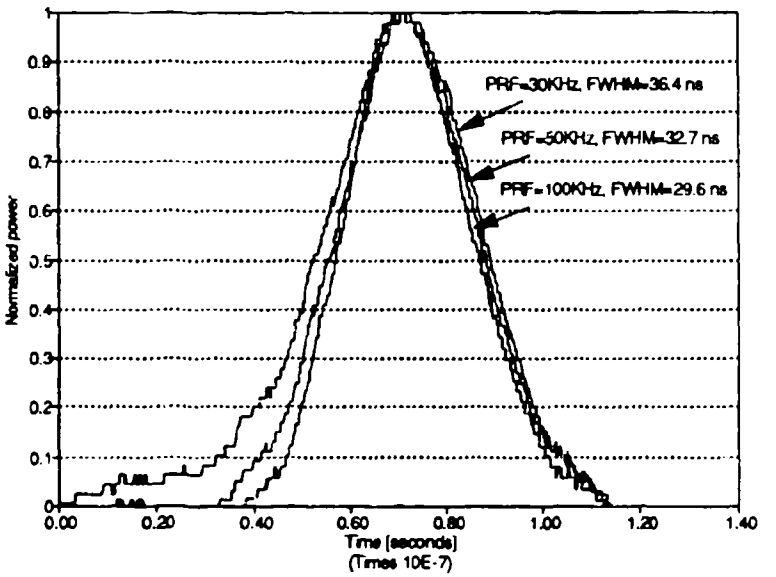

Figure 8. Temporal format of the repetitively pulsed source.

The temporal profiles were recorded with the liquid nitrogen cooled resonant cavity HgCdTe detectors. The average power increases with the higher modulation frequencies, but the peak

powers decrease. Since the theoretical estimates of efficiency for pulsed sources are proportional to the peak irradiance values, most of the efficiency measurements were completed using the 30 kHz modulation frequency.

Frequency Stability. The frequency stability was characterized by two methods. The first involved the observation of the main amplifier's output through an infrared grating spectrometer designed for carbon-dioxide laser wavelengths. Only the *P(20)* line at 10.6 μm was observed. The second method involved heterodyning the main amplifier and local oscillator beams. The constant offset frequency of 60 MHz was observed after careful alignment of the optical system.

Spatial Profiles. The two-dimensional spatial profile of the repetitively pulsed formats were observed using the pyroelectric vidicon camera system once the beam had been attenuated to less by 10 mW/cm^2; approximately three orders of magnitude of attenuation were required to observe the unfocussed beam at 30 cm from the output port of the laser. A representative spatial profile is shown in Figure 9.

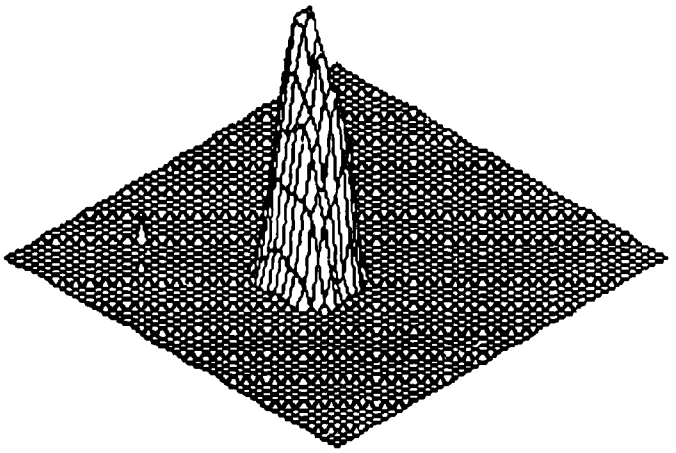

Figure 9. Spatial profile of the repetitively pulsed main amplifier at 30 kHz. The diagram represents the entire field of view of the infrared vidicon camera where the effective area is 6 mm square.

The beam appears to be Gaussian (TEM_{00}) with only minor local deviations. This provides confidence in the calculations of the focussed spot sizes since the theory of optical matrix transformations as outlined above is applicable to the Gaussian mode.

Characterization of the Crystals

The sample of $AgGaSe_2$ was provided under contract to the Wright Research Development Center's Electro-Optic Sources Branch by Cleveland Crystals, Cleveland OH. The 9mm × 9mm × 29mm crystal was provided with a two layer λ/4 (PbF_2 and ThF_2 based) anti-reflection coating for 10.6μm and 5.3μm and was cut from the boule at 57.17° with respect to the optic axis (their calculated phase matching angle); note Figure 10.

The 6.2mm × 6.2mm × 11mm sample of $ZnGeP_2$ was an uncoated sample which was cut for non-critical phase matching with the face perpendicular to the x-axis (also the [010] direction); note Figure 11.

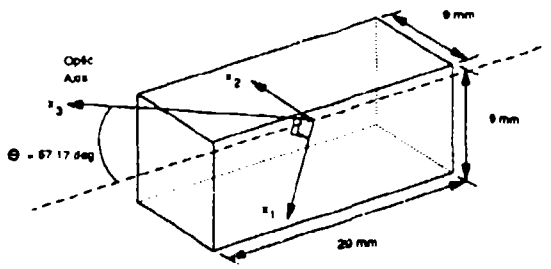

Figure 10. $AgGaSe_2$ crystal cut for Type I phase matching at 57.17°.

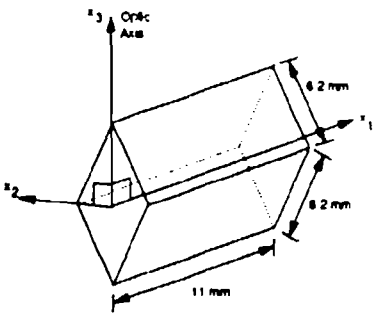

Figure 11. $ZnGeP_2$ crystal cut for Type I phase matching at 90°.

The crystals were characterized by spectral scans as well as direct absorptivity measurements using the smaller, low power beam of the local oscillator.

Absorptivity Measurements. In order to avoid errors that would be introduced under the assumption that the laser source possessed a long term amplitude stability, this measure-

ment was conducted in three separate parts (26:5). Note the definitions established in Figure 12 for the components of the incident beam of intensity, *I*, and the various reflected and transmitted portions.

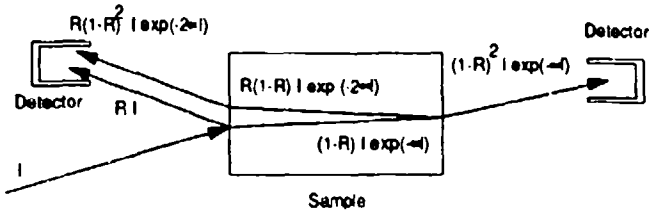

Figure 12. Calculation of the absorption/scattering loss. R is the reflectivity of the crystal surface (assumed to be equal on both ends), I is the incident intensity, *L* is the length of the crystal and α is the loss per unit length of the material.

We seek to establish an experimental method which will remove *I* from the calculations of the absorptivity, α. From the three measurements taken in the manner as shown in Figure 13, note that the ratios are not functions of the intensity of the incident beam and will thus remove the uncertainty in the long term amplitude stability of the source.

If we establish the ratio

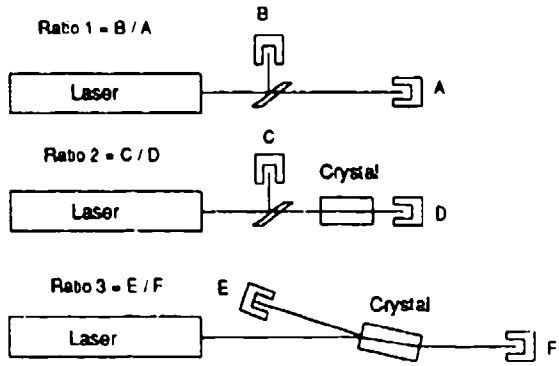

Figure 13. Three sets of measurements to be taken in determining the absorptivity.

$$T = \frac{\text{Ratio-1}}{\text{Ratio-2}} = (1 - R)^2 \exp(-\alpha L) \tag{3.10}$$

and note the specific definition of the terms that make up Ratio-3 as

$$\text{Ratio-3} = \frac{R + R(1 - R)^2 \exp(-2\alpha L)}{(1 - R)^2 \exp(-\alpha L)} \tag{3.11}$$

we note that Eq.(2.10) can be substituted into Eq.(2.11) to yield a parametric equation with respect to the reflectivity of the surface of the crystal R.

$$R = \frac{(\text{Ratio-3})T}{1 + T^2/(1 - R)^2} \tag{3.12}$$

It is a straight forward matter to iteratively solve for the R and subsequently solve of the absorptivity by

$$\alpha = -\frac{1}{L} \ln\left(\frac{T}{(1 - R)^2}\right) \tag{3.13}$$

An alternative method of measuring the absorptivity simply involves the measurement shown in Figure 13 for Ratio-3 given that we have a reasonably good estimate of the surface reflectivity. In general, we can use that defined by the previous analysis as a good starting point. This second method involves measuring the transmittance of the crystal directly and applying Eq.(2.13).

The low power continuous wave output of the local oscillator was used to conduct these measurements, where the beam was apertured down such that the physical dimensions of the crystal did not obscure the beam and lead to erroneously high values of the absorptivity.

The results of the measurements of the two crystals is shown in the table below. Note that the measured values for both of the methods agree very well. The error is rather large due to the uncertainty in the surface reflectivity.

Table 1.

Results of the absorptivity measurements

	$AgGaSe_2$	$ZnGeP_2$
Absorptivity measured by method 1	0.0267 ± 0.0270 /cm	0.681 ± 0.0650 /cm
Surface reflectivity of the sample	0.0055 ± 0.0005	0.248 ± 0.025
Absorptivity measured by method 2	0.0271 ± 0.0038 /cm	0.661 ± 0.0623 /cm

Spectrographic Measurements. The samples were scanned with a Fourier transform infrared spectrometer in order to establish a relative value of the absorptivity at the second harmonic's frequency as well as provide an additional check for the measurements above.

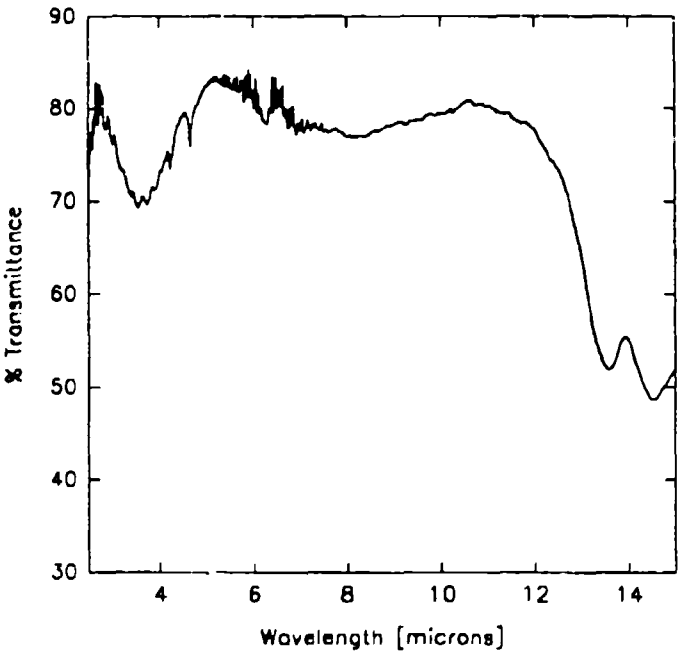

Figure 14. Infrared transmission spectrum of the $AgGaSe_2$ crystal.

In both crystals, the transmission (which can be related to the absorptivity) is relatively constant across the region of interest from 5.3μm to 10.6μm. With the laser source and the crystals to be studied well characterized, we are able to continue with the theoretical estimates of the crystal performance and the experimental designs.

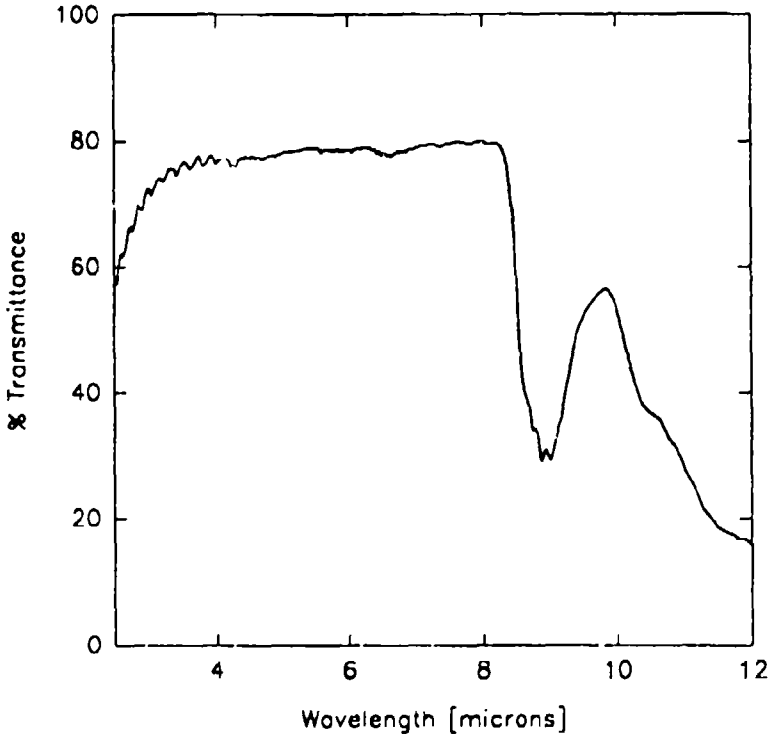

Figure 15. Infrared transmission spectrum of the $ZnGeP_2$ crystal.

IV. Theoretical Calculations of Crystal Performance

To begin the experiments to characterize, and hopefully optimize, the performance of the crystals used in the second harmonic generation of 10.6 μm radiation, a number of calculations will prove useful in establishing the experimental design. Given the constraints of available equipment, a primary concern was establishing the intensity levels of the non-focussed and focussed beam at the face and center of the crystal. With this, we are able to estimate the efficiencies and compare the values of peak and average power to published damage thresholds. They also provide a means to approximate the temperature profiles generated during exposure. This would provide an estimate of the stresses being placed on the crystal.

Presented below are the various mathematical developments for the calculation of conversion efficiency under different experimental conditions. Comparison to the experimental data are carried out in Chapter VI.

Nondepleted Plane Wave Approximation

As an initial estimate of the conversion efficiencies, we begin by analyzing the dependences noted in Eq.(2.18). Written in terms of the angular sensitivity, β_θ, the conversion efficiency, $P^{(2\omega)}/P^{(\omega)}$, becomes

$$\eta = 2\left(\frac{\mu_0}{\varepsilon_0}\right)^{3/2}\frac{\omega_1^2 L^2}{n^3}\left(\frac{(P^{(\omega)})}{\text{area}}\right)(d_{\text{eff}})^2\frac{\sin^2\beta_\theta(\theta_m-\theta)}{(\beta_\theta(\theta_m-\theta))^2} \tag{4.1}$$

where $d_{\text{eff}} = d'_{ijk}$ is the effective nonlinear coefficient from the previous development.

This solution was derived under the assumption that the plane wave incident on the crystal is not affected by the development of the second harmonic (non-depleted input approximation). The wavefront is assumed to be infinite in extent and have a constant amplitude in both time and space. The efficiency is proportional to the intensity, $P^{(\omega)}$/area, and to the square of the crystal length, L. The dependence upon the direction of propagation is accounted for in two separate terms. The deviation from the phase-matching angle, θ_m, produces the characteristic

$sinc^2$ drop off, and d_{eff} possesses an angular dependence determined by the crystal symmetry and the corresponding nonlinear optical tensor.

In this experiment, we have control over some of these variables, such as the intensity levels and the angular orientation of the crystals, but little control over the constants such as crystal length, phase matching angle and d_{eff}. For this reason, we will have to determine the values for these constants in order to specify the appropriate magnitudes for the variables.

Calculation of Beam Parameters - Peak and Average Intensities

Given the spot size of the laser at some point, we are able to estimate the peak intensity (fluence, or irradiance) of the spatial profile at the temporal peak. From the characterization of the laser source, we are able to approximate the pulses to be Gaussian in space and time. For the case of the 30 kHz repetition frequency, the measured FWHM (full width at half of the maximum value) is 36.4 ns (see Figure 8) which leads to a characteristic time at the 1/e point of the pulse of $\tau = 21.86ns$. The power of a single pulse as a function of time is

$$P(t) = P_{Peak} e^{-(t/\tau)^2} \tag{4.2}$$

where P_{Peak} is the peak power. Given a value for the average power, P_{AVG}, and the pulse repetition frequency, ν_{rep}, the peak power may then be written (9:663)

$$P_{Peak} = \frac{P_{AVG}}{\nu_{rep}} \left(\int_{-\infty}^{\infty} e^{-(t/\tau)^2} dt \right)^{-1} = \frac{P_{AVG}}{\sqrt{\pi} \nu_{rep} \tau} \tag{4.3}$$

This is the total power at the temporal peak of the pulse. It can be related to the intensity given a specified area through which the power will pass. Given the equation for the radial intensity distribution of a Gaussian beam

$$I(r,\theta) = I_{Peak} e^{-(r/w)^2} \tag{4.4}$$

The total power is given as the integral of this function over all space and is equal to the peak power derived above.

$$P_{Peak} = I_{Peak} \int_0^{2\pi} \int_0^{\infty} r \cdot e^{-(r/w)^2} \, dr d\theta = I_{Peak} (\pi w^2) \tag{4.5}$$

Thus, the peak intensity may be written (15:302)

$$I_{Peak} = \frac{P_{AVG}}{\pi^{3/2} w^2 \nu_{rep} \tau} \tag{4.6}$$

where, in general, the spot size, w, will be a function of distance from the laser or the focussing element.

Eq.(2.8) yields the spot size as a function of the distance from the laser with or without a focussing element and can be used to find the intensity at the face of the crystal. In order to find the values at the center, we must use the transformation matrix resulting from

$$\begin{pmatrix} A & B \\ C & D \end{pmatrix} = \begin{pmatrix} 1 & \frac{L}{2} \\ 0 & 1 \end{pmatrix} \begin{pmatrix} 1 & 0 \\ 0 & \frac{n_1}{n_2} \end{pmatrix} \begin{pmatrix} 1 & z_3 \\ 0 & 1 \end{pmatrix} \begin{pmatrix} 1 & 0 \\ -\frac{1}{f} & 1 \end{pmatrix} \begin{pmatrix} 1 & z_2 + \text{Offset} \\ 0 & 1 \end{pmatrix} \tag{4.7}$$

where the ratio of the indices accounts for the interface of the crystal, n_2, of length L. Figures 16 and 17 show the spot sizes and the peak and average powers for the unfocussed case.

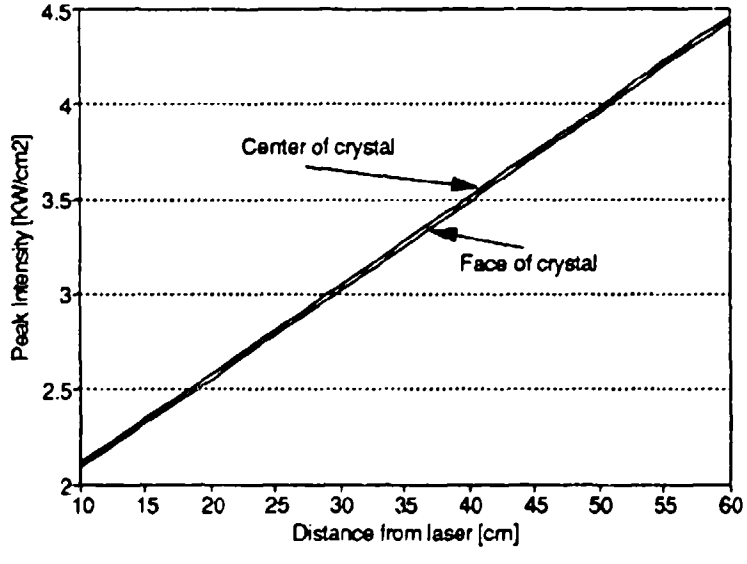

Figure 16. Spot size as a function of distance from the output port of the laser at the face and center of the $AgGaSe_2$ crystal.

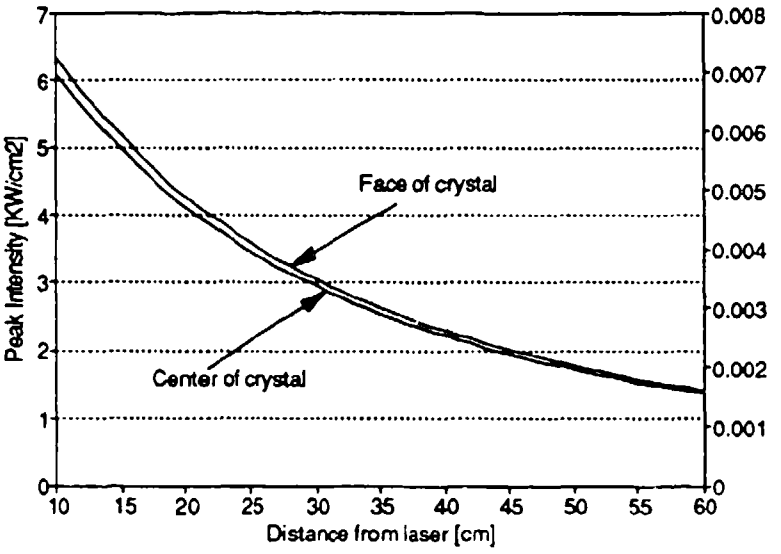

Figure 17. Peak and average intensity at the center of the beam as a function of distance from the output port of the laser given for the face and center of the $AgGaSe_2$ crystal.

The calculations for the focussed case are summarized in Figures 18 through 22 for the face and center of the two crystals for two different distances from the laser. These plots are normalized for an average power of 1 Watt at a pulse repetition frequency of 30 kHz (FWHM = 36.4 ns) such that the values can be interpreted given the experimental setup.

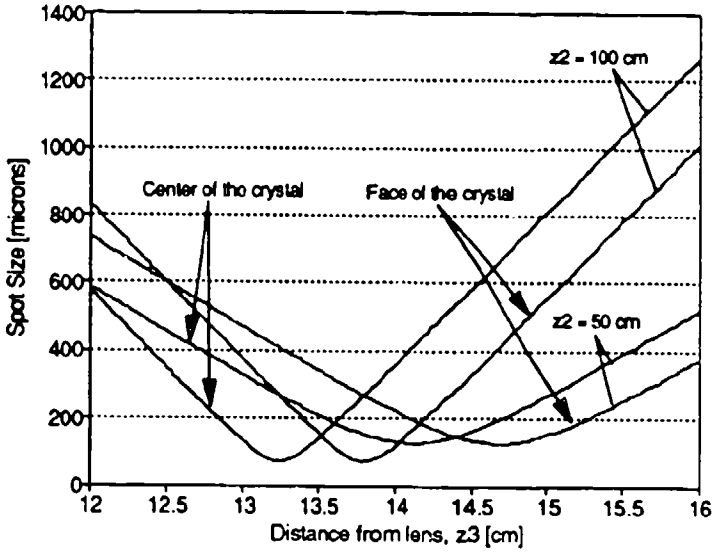

Figure 18. For a focal length of 12.5 cm, the plot shows the spot size as a function of the distance from the focussing element, z_3, at the face and center of the $AgGaSe_2$ crystal for values of z_2 (distance from the laser to the lens) of 0.5 m and 1 m. Note the distance z_3 is to the face of the crystal, thus as the crystal is moved towards the focus (away from the lens) the beam waist passes through the center of the crystal first.

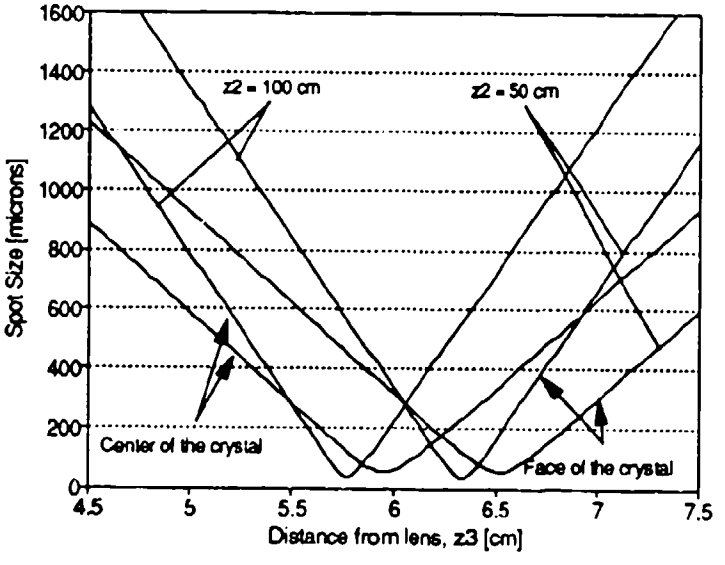

Figure 19. For a focal length of 6.05 cm, the plot shows the spot size as a function of the distance from the focussing element, z_3, at the face and center of the $AgGaSe_2$ crystal for values of z_2 (distance from the laser to the lens) of 0.5 m and 1 m.

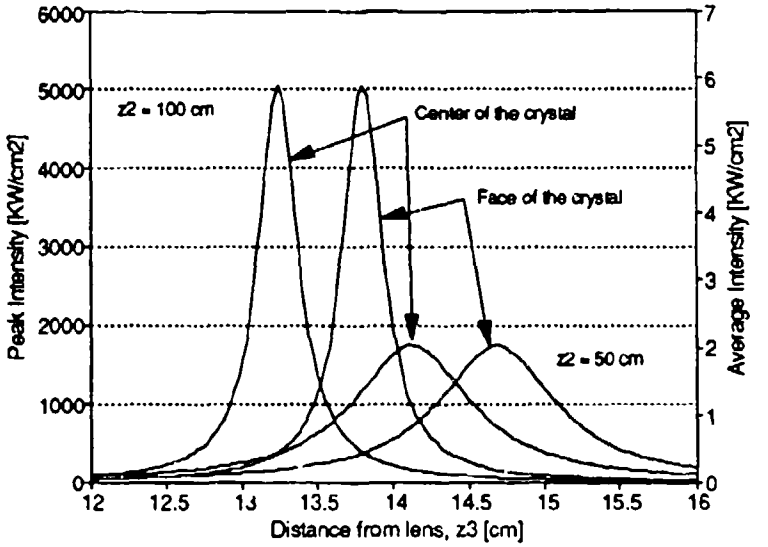

Figure 20. For a focal length of 12.5 cm, the plot shows the peak and average intensity as a function of the distance from the focussing element, z_3, at the face and center of the $AgGaSe_2$ crystal for values of z_2 (distance from the laser to the lens) of 0.5 m and 1 m. These values have been normalized to an average power 1 Watt at a pulse repetition frequency of 30 kHz.

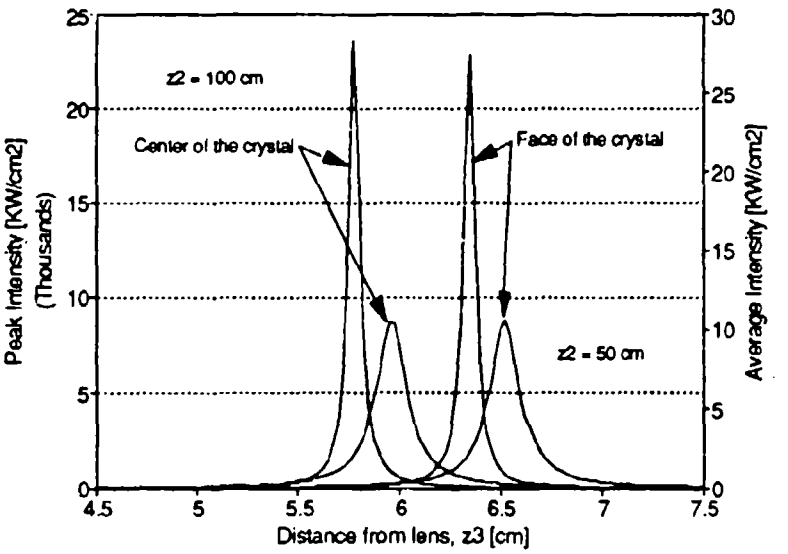

Figure 21. For a focal length of 6.05 cm, the plot shows the peak and average intensity as a function of the distance from the focussing element, z_3, at the face and center of the $AgGaSe_2$ crystal for values of z_2 (distance from the laser to the lens) of 0.5 m and 1 m. These values have been normalized to an average power of 1 Watt at a pulse repetition frequency of 30 kHz.

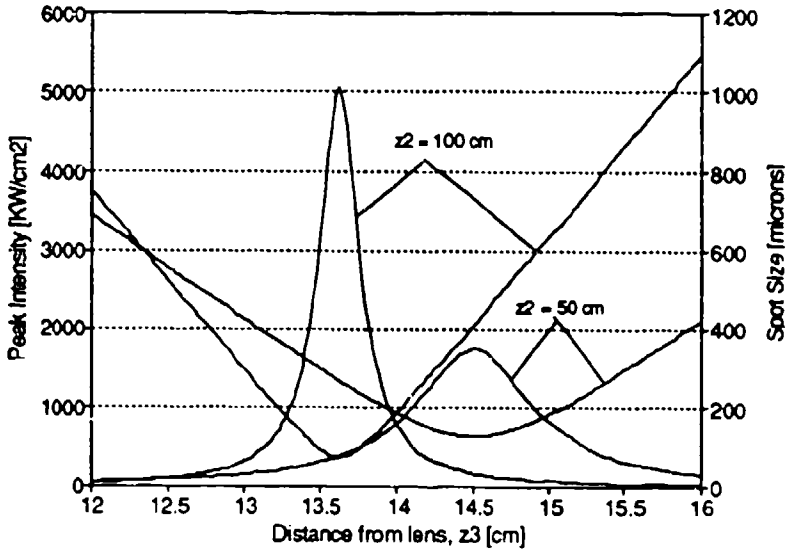

Figure 22. For a focal length of 12.5 cm, the plot shows the peak intensity and spot size as a function of the distance from the focussing element, z_3, at the center of the $ZnGeP_2$ crystal for values of z_2 = 0.5 m (distance from the laser to the lens). These values have been normalized to an average power of 1 Watt at a pulse repetition frequency of 30 kHz.

These for the spot sizes, peak and average intensities may then be applied to the theoretical estimates of the conversion efficiency. Note in Figure 18, that the focussed waist radius is not changed by the introduction of the crystal, only its position is moved in accordance with the change in slope n_1/n_2.

Phasematched Condition and the Effective Nonlinear Coefficient

The phase matched condition is a value which can be derived as the numerical solution to Eqs.(A.24) in Appendix A. We will restrict our attention to reference the principal coordinate system and redefine the subscripts 1,2 and 3 in this set to refer to the components of the field vectors parallel to the principal axes x, y and z respectively. If we consider the direction of propagation in a spherical coordinate system, the directions cosines may be written

$$s_x = \frac{k_x}{|\vec{k}|} = \sin\theta\cos\phi$$

$$s_y = \frac{k_y}{|\vec{k}|} = \sin\theta\sin\phi \qquad (4.8)$$

$$s_z = \frac{k_z}{|\vec{k}|} = \cos\theta$$

where θ is the angle between the propagation vector and the z axis and ϕ is the angle between the projection of the propagation vector onto the x-y plane and the x axis.

Recall that for the non-trivial solution, the determinant of the matrix for this set must be equal to zero. When multiplied out, it reduces to a form which is quadratic in n^2. If we normalize the first term and consider the cases of the fundamental and second harmonic separately, the two separate solutions take on the forms

$$x_1^2 + B_1 x_1 + C_1 = 0, \qquad x_1 = n_\omega^{-2} \qquad (4.9)$$

$$x_2^2 + B_2 x_2 + C_2 = 0, \qquad x_2 = n_{2\omega}^{-2} \qquad (4.10)$$

The constants in the equations above are

$$B_1 = -s_x^2(n_{y,\omega}^{-2} + n_{z,\omega}^{-2}) - s_y^2(n_{x,\omega}^{-2} + n_{z,\omega}^{-2}) - s_z^2(n_{x,\omega}^{-2} + n_{y,\omega}^{-2}) \qquad (4.11)$$

$$C_1 = s_x^2 n_{y,\omega}^{-2} n_{z,\omega}^{-2} + s_y^2 n_{x,\omega}^{-2} n_{z,\omega}^{-2} + s_z^2 n_{x,\omega}^{-2} n_{y,\omega}^{-2} \qquad (4.12)$$

$$B_2 = -s_x^2(n_{y,2\omega}^{-2} + n_{z,2\omega}^{-2}) - s_y^2(n_{x,2\omega}^{-2} + n_{z,2\omega}^{-2}) - s_z^2(n_{x,2\omega}^{-2} + n_{y,2\omega}^{-2}) \qquad (4.13)$$

$$C_2 = s_x^2 n_{y,2\omega}^{-2} n_{z,2\omega}^{-2} + s_y^2 n_{x,2\omega}^{-2} n_{z,2\omega}^{-2} + s_z^2 n_{x,2\omega}^{-2} n_{y,2\omega}^{-2} \qquad (4.14)$$

The indices of refraction refer to their values along the respective principal axes for a given frequency, ω or 2ω, and temperature.

The solutions to Eq.(4.9) and Eq.(4.10) are

$$n_{\omega,i} = \frac{\sqrt{2}}{\sqrt{-B_1 \pm \sqrt{B_1^2 - 4C_1}}} \qquad (4.15)$$

$$n_{2\omega,i} = \frac{\sqrt{2}}{\sqrt{-B_2 \pm \sqrt{B_2^2 - 4C_2}}} \qquad (4.16)$$

where i = 1 or 2, refers to the solution for the case of the square root term being positive or negative respectively (24:65).

Note for all classes of crystals (biaxial, positive and negative uniaxial), $n_{\omega,2} > n_{\omega,1}$ and $n_{2\omega,2} > n_{2\omega,1}$. For Type I phase matching, $n_{\omega,2} = n_{2\omega,1}$, resulting in

$$\frac{\sqrt{2}}{\sqrt{-B_1 - \sqrt{B_1^2 - 4C_1}}} = \frac{\sqrt{2}}{\sqrt{-B_2 + \sqrt{B_2^2 - 4C_2}}} \tag{4.17}$$

For the case of a uniaxial crystal, the ordinary and extraordinary indices of refraction at the fundamental relate to the indices in the solution to the phase-matched condition by $n_{x,\omega} = n_{y,\omega} = n_{o,\omega}$ and $n_{z,\omega} = n_{e,\omega}$. This is true for 2ω as well, and by inserting Eqs.(4.11-14) into Eq.(4.17), the phase-matched angle for $AgGaSe_2$ which satisfies this relation is $\theta = 55.022^0$. The graphical representation of this solution is shown in Figure 23. The phase matching angle corresponds to the intersection of the ordinary index of refraction for ω with the extraordinary index for 2ω. Note that there is no dependence of the solution on ϕ for uniaxial crystals because $n_{x,\omega} = n_{y,\omega}$. The optimum value for ϕ is determined by the effective nonlinear coefficient. The general solution to the Type I phase-matched condition in negative uniaxial crystals reduces to Eq.(2.21) and for positive uniaxial crystals to Eq.(2.22).

which may be satisfied for some particular direction of propagation defined by θ and ϕ.

The indices of refraction to the fundamental and second harmonic are generally derived from the appropriate Sellmeier equations and material dependent constants which are listed in the table below. The nominal indices of refraction at 10.6 μm for the two crystals considered in this study are 2.59 for $AgGaSe_2$ and 3.11 for $ZnGeP_2$.

Table 2.

Sellmeier coefficients for $AgGaSe_2$ and the temperature dependent $ZnGeP_2$
(Note : $n^2 = A + B/(1-C/\lambda^2) + D/(1-E/\lambda^2)$)
λ is in micrometers, and E (the square of the fundamental lattice vibration frequency) is generally a constant, and temperature is in degrees Centigrade.

Crystal & E Value (μm^2)	Temperature (°C)	Polarization	A	B	C	D
$AgGaSe_2$ (1600.00)	25	o	3.9362	2.9113	0.1507	1.7954
		e	3.3132	3.3616	0.1459	1.7677
$ZnGeP_2$ (662.55)	400	o	4.6171	5.4709	0.1495	1.4912
		e	4.6791	5.6826	0.1567	1.4577
	200	o	4.5654	5.3382	0.1419	1.4913
		e	4.6732	5.4842	0.1499	1.4581
	100	o	4.5209	5.2917	0.1376	1.4911
		e	4.6559	5.4001	0.1460	1.4580
	-100	o	4.3761	5.2540	0.1275	1.4903
		e	4.5801	5.2747	0.1368	1.4576

Adapted from Kildal (16:317) and Bhar (3:839)

For the case of $ZnGeP_2$, whose indices of refraction are given as functions of the temperature, the phase-matched angle is found in the same manner. The only difference lies in that this is a positive uniaxial crystal and the solution will be the intersection of extraordinary index of refraction at the fundamental and the ordinary at the second harmonic. Knowing that the temperature required for non-critical phase-matching at 10.6μm is near 140°C (3:541), we can

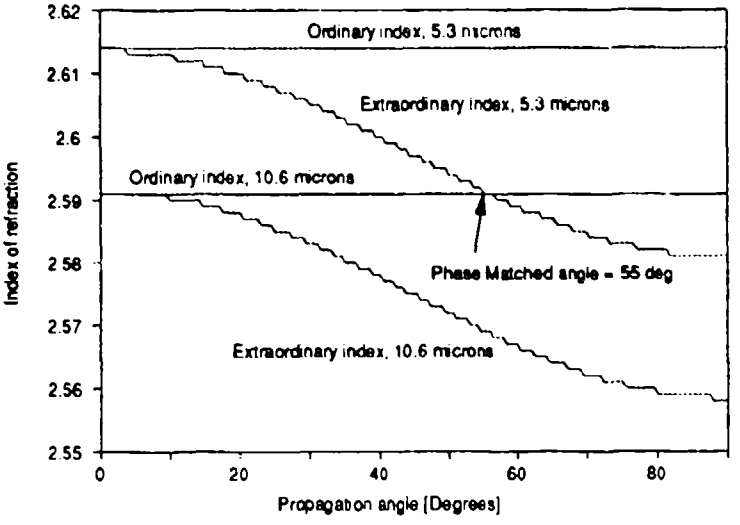

Figure 23. Graphical solution to the phase-matching angle in $AgGaSe_2$. Note the intersection of the extraordinary index of refraction at the second harmonic frequency with the ordinary index of the fundamental. Note, the lines are staggered due to the limited accuracy of the published indices of refraction.

fit a second order polynomial to the Sellmeier coefficients as cited in Table 3 for the three higher temperatures. Table 4 shows the coefficients of these fits over the range from 100°C to 400°C.

These temperature dependent coefficients can be substituted into the same form of the Sellmeier equation cited with Table 3 leading to a temperature dependent phase matching angle. The results of this analysis are shown in Figure 24. The analysis says the material is non-critically phase matched over a large temperature range, from 130°C to 190°C. The discontinuity in the solution can be attributed to the limited accuracy of the computational routine employed to find the intersections of the temperature dependent indices of refraction.

Table 3.

Constants of the second order polynomials
describing the temperature dependence of the
Sellmeier coefficients for $ZnGeP_2$ over the range from 100°C to 400°C
Note: (Coefficient(T) = $\mathcal{A}T^2$ + $\mathcal{B}T$ + C)
T, temperature, is in degrees Centigrade.

Coefficient	Polarization	$\mathcal{A}$	$\mathcal{B}$	C
A (T)	o	-6.2167×10^{-7}	6.315×10^{-4}	4.46397
	e	-4.7833×10^{-7}	3.165×10^{-4}	4.62903
B (T)	o	6.6167×10^{-7}	2.665×10^{-4}	5.25843
	e	5.0333×10^{-7}	6.900×10^{-4}	5.32607
C (T)	o	-1.6667×10^{-8}	4.800×10^{-5}	0.132967
	e	-1.6667×10^{-8}	4.400×10^{-5}	0.141767
D (T)	o	1.4917×10^{-6}	-7.455×10^{-4}	1.55073
	e	1.0000×10^{-8}	4.000×10^{-6}	1.45770
E (T)	o	0.0	0.0	662.55
	e	0.0	0.0	662.55

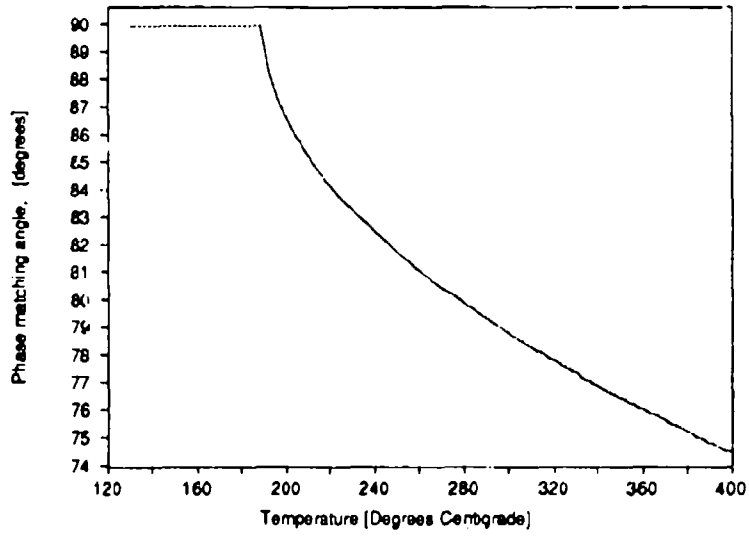

Figure 24. Phase matched angle as a function of temperature for $ZnGeP_2$. Note that the phase-matched angle is nearly $\pi/2$ over a relatively wide angular range. This is the case of non-critical phase matching in this positive uniaxial crystal.

These solutions for both types of crystals tell us the angle of propagation required to minimize the phase mismatch Δk and thus maximize the $sinc^2$ term. There is an angular dependence included in the effective nonlinear coefficient which has yet to be determined.

Returning to the set of simultaneous equations (Eqs.(2.24)) from which the phase-matching conditions were derived, we are now interested in the electric field components of the fundamental and second harmonic waves. We can express these components in terms of the cosines of the angles, α, β, and γ, with respect to each of the principal axes, x, y and z respectively, as

$$\vec{E}_{m\omega,i}(\cos\alpha_{m\omega,i}, \cos\beta_{m\omega,i}\cos\gamma_{m\omega,i}) \tag{4.18}$$

where m = 1 and 2 indicate fundamental and second harmonic, and i = 1 or 2, indicate the two possible values of the refractive indices (24:56). For second harmonic generation, two of these field components will be the same. Given a direction of propagation in the principal coordinate system, the direction cosines may be found for this set of equations under the restriction

$$(\cos\alpha_{m\omega,i})^2 + (\cos\beta_{m\omega,i})^2 + (\cos\gamma_{m\omega,i})^2 = 1 \tag{4.19}$$

Recall Eq.(2.3), the second order polarization, which may be written in terms of these direction cosines and the two applied electric fields as (24:66)

$$P^{2\omega} = a_i d_{ijk} a_j a_k E_j(\omega) E_k(\omega) \tag{4.20}$$

For Type I phase matching we have

$$a_j a_k = \begin{pmatrix} \cos^2\alpha_{\omega,2} \\ \cos^2\beta_{\omega,2} \\ \cos^2\gamma_{\omega,2} \\ 2\cos\beta_{\omega,2}\cos\gamma_{\omega,2} \\ 2\cos\alpha_{\omega,2}\cos\gamma_{\omega,2} \\ 2\cos\alpha_{\omega,2}\cos\beta_{\omega,2} \end{pmatrix} \tag{4.21}$$

and for the $\bar{4}2m$ class crystals,

$$d_{ijk} = \begin{pmatrix} 0 & 0 & 0 & d_{14} & 0 & 0 \\ 0 & 0 & 0 & 0 & d_{14} & 0 \\ 0 & 0 & 0 & 0 & 0 & d_{36} \end{pmatrix} \tag{4.22}$$

$$a_i = (\cos\alpha_{2\omega,1}, \cos\beta_{2\omega,1}, \cos\gamma_{2\omega,1}) \tag{4.23}$$

Completing the matrix multiplications indicated, we find

$$\begin{aligned} d_{eff} &= 2d_{14}\cos\alpha_{2\omega,1}\cos\beta_{\omega,2}\cos\gamma_{\omega,2} \\ &+ 2d_{14}\cos\beta_{2\omega,1}\cos\alpha_{\omega,2}\cos\gamma_{\omega,2} \\ &+ 2d_{36}\cos\gamma_{2\omega,1}\cos\alpha_{\omega,2}\cos\beta_{\omega,2} \end{aligned} \tag{4.24}$$

For $AgGaSe_2$, a negative uniaxial crystal, the solution to the phase matching conditions requires the fundamental to be perpendicular to the optic axis (an ordinary wave). This makes $\gamma_{\omega,2} = \pi/2$ and all terms containing $\cos\gamma_{\omega,2}$ go to zero. Only the third term in Eq.(4.24) survives, which is dependent upon d_{36}. We can relate the direction cosines of the electric field to the angles describing the propagation direction by the following

$$\gamma_{2\omega,1} = \frac{\pi}{2} - \theta \qquad \alpha_{\omega,2} = \frac{\pi}{2} - \phi \qquad \beta_{\omega,2} = \pi - \phi \tag{4.25}$$

under the restriction that the electric field of the fundamental lies in the x-y plane. d_{eff} then becomes

$$d_{eff} = 2d_{36}\cos\left(\frac{\pi}{2} - \theta\right)\cos\left(\frac{\pi}{2} - \phi\right)\cos(\pi - \phi) \tag{4.26}$$

which can be related by trigonometric identities to the more familiar form quoted for negative uniaxial crystals of this class (25:64)

$$d_{eff} = -d_{36}\sin\theta\sin 2\phi \tag{4.27}$$

where $d_{36} = 43 \times 10^{-12}$ pm/V for $AgGaSe_2$ (11:788). This is a relatively insensitive function of ϕ near $\phi = \pi/4$.

Similar arguments may be applied to the case for $ZnGeP_2$, which is a positive uniaxial crystal and the electric field of the fundamental is restricted to lie perpendicular to the x-y plane. Only the first term of Eq.(4.24) survives and it may be related to the angles describing the propagation direction in a similar manner to obtain

$$d_{eff} = d_{14}\sin 2\theta\cos 2\phi \tag{4.28}$$

where $d_{14} = 111 \times 10^{-12}$ pm/V for $ZnGeP_2$ (4:302).

An immediate source of concern with the solution for $ZnGeP_2$ lies in that at relatively moderate temperatures, less that 200°C, the phase matching angle is approximately $\pi/2$, which makes d_{eff} very small. In fact, in order to take advantage of the relatively high nonlinear coefficient d_{14}, we would like to operate at an angle close to $\theta = \pi/4$ and $\phi = 0$. If we note the orientation of the principal axes in Figure 11, it will very difficult to achieve angles approaching these values in the actual experiment. The specifics of these limitations will be discussed in the next chapter. Plots of the d_{eff} for both of the crystals are shown in Figures 25 and 26 as a function of θ and ϕ. Note that Type II phase matching is not possible with either of these crystals.

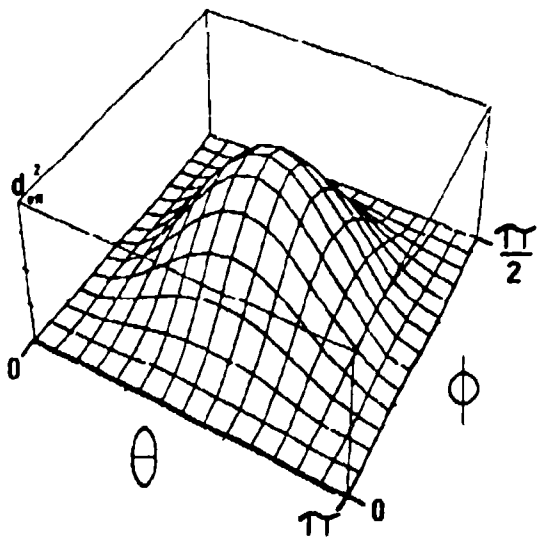

Figure 25. First quadrant of the d_{eff}^2 surface for $AgGaSe_2$. The plot ranges from $0 \leq \theta \leq \pi$ and $0 \leq \phi \leq \pi/2$, where the peak value is $d_{36}^2 = (43\text{pm/V})^2$.

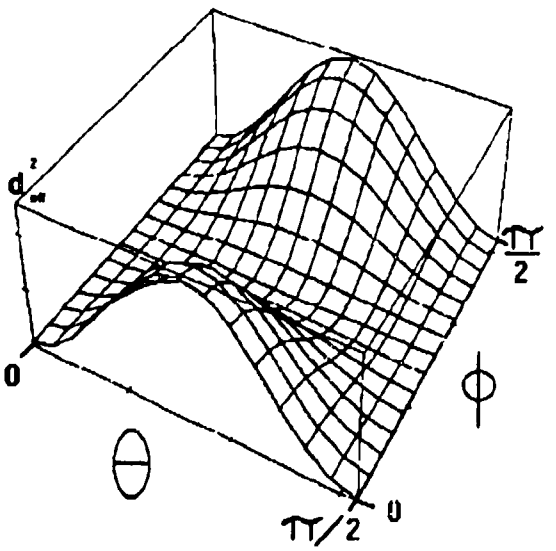

Figure 26. First quadrant of the d_{eff}^2 surface for $ZnGeP_2$. The plot ranges from $0 \leq \theta \leq \pi/2$ and x to $0 \leq \phi \leq \pi/2$, where the peak value is $d_{36}^2 = (111\text{pm/V})^2$.

Bringing the developments of the effective nonlinear coefficients and the angular sensitivities together, the first order approximation to the conversion efficiency, Eq.(4.1), may be written in terms of the direction of propagation in the principal coordinate system, the physical dimensions of the crystal and average intensities (CW input). A summary of the calculated material parameters which will be used in the following sections is shown in Table 5.

Table 4.

Calculated Material Parameters for $AgGaSe_2$ and $ZnGeP_2$. Values for $ZnGeP_2$ calculated for the phase matched condition at 211°C.

	$AgGaSe_2$	$ZnGeP_2$ (at 211°C)
Ordinary index of refraction		
at 10.6μm	2.5915	3.1020
at 5.3μm	2.6136	3.1426
Extraordinary index of refraction		
at 10.6μm	2.5585	3.1430
at 5.3μm	2.5809	3.1833
Phase matching angle, θ_m	55.02°	85.16°
Angular acceptance, $\Delta\theta$ (for a 29mm $AgGaSe_2$ crystal and a 11mm $ZnGeP_2$ crystal)	0.304°	0.678°
Angular sensitivity, β_θ (length of the crystals, L, not included, note Eqs.(2.24-25))	-18089.8 rad/m	4166.2 rad/m
Birefringent walkoff angle, ρ	0.67°	-0.13°

Eq.(4.1) will be valid for relatively low conversion efficiencies in the non-focussed case (plane wave). The solution is misleading in that it prompts the use of longer crystals for higher efficiencies. In the next section it will be shown that as the power in the second harmonic grows, it gives rise to a dipole oscillation at the fundamental frequency which reradiates in the phase-matched direction.

Plane-Wave Solutions - Depleted Input

Eq.(4.1) provides an initial estimate of the overall conversion efficiency, but does not include several important parameters of interest. If we retain z dependence of the fundamental field in the solution, we are able to track the amplitude of the second harmonic as a function of distance as well as the depletion of the fundamental. The development in Yariv (23:528) yields the form

$$\frac{P^{(2\omega)}}{P^{(\omega)}} = \tanh^2\left[\sqrt{\frac{n_1}{2\omega_1}}E_1(0)\kappa z\right] \tag{4.29}$$

where $E_1(0)$ is the amplitude of the fundamental at $z = 0$, and κ is defined by

$$\kappa = d'_{123}\sqrt{\frac{\mu_0}{\epsilon_o}\frac{\omega_1\omega_2\omega_3}{n_1n_2n_3}} \tag{4.30}$$

In the limit that the argument of the hyperbolic tangent approaches infinity, the solution approaches 1/2. Conservation of energy requires that no more than one half as many photons can be produced at the second harmonic than those input at the fundamental. It concludes that with longer crystals, the closer the final product will come to this value.

In a more exhaustive development, the divergence of the pump beam, its degradation through the crystal and the angular acceptance of the material play major roles in accurately predicting the efficiency and limiting values.

If we considered the case of a single pulse at the frequency of the fundamental propagating through the crystal, it gives rise to a dipole oscillation at the second harmonic frequency. This oscillation radiates a field whose amplitude grows in the phase matched direction as function of distance. Given that the energy coupling of the fundamental pulse to the dipole radiators is proportional to the instantaneous power, the temporal peak of the pulse will be degraded as it gives up its energy to the crystal. The spatial peak will be degraded as well, but we will assume that the incident monochromatic plane wave possesses a constant spatial intensity profile. If we disregard the local variations in the temporal shape of the pulse due to this

factor, we can expect the $tanh^2$ argument in Eq.(4.29) to describe the limit of this coupling.

The exact solution to the coupled wave equations (Eqs.(2.12)), however, describes the secondary reaction of the dipole oscillation in the media. The field at the second harmonic will promote an oscillation at the fundamental frequency which will in turn cause reradiation at this wavelength. This rise and fall is caused by the competing wave interaction of the two fields can be described by a general class of solutions known as solitons (solitary wave solutions). This back conversion to the fundamental frequency brings about a limitation on the useful length of material in producing the second harmonic.

For Type I phase matching, the equations describing the interaction of the first and second harmonics for a single pulse with an input intensity, I, and a crystal thickness L have been solved (1:1925) to give the form (13:576),

$$\eta = \tanh^2\left[\frac{1}{2}\tanh^{-1}(sn[2\eta_0^{1/2}, \quad 1 + \delta^2/4\eta_0])\right] \tag{4.31}$$

where the nonlinear drive, η_0, and the dephasing terms, δ, are given by

$$\eta_0 = C^2 I L^2 \tag{4.32}$$

$$\delta = (1/2)\Delta k L \quad . \tag{4.33}$$

The coupling, C, given in units of $GW^{-1/2}$ is shown below, and sn in Eq.(4.31) is the Jacobi elliptic function.

$$C = 5.46 \quad d_{eff}(\text{pm/V}) \quad / \quad \lambda_1(\mu m)(n_1 n_2 n_3)^{1/2} \tag{4.34}$$

Depletion of the input beam due to conversion to the second harmonic is included in this development, but losses due to absorption have been omitted. In the limit of a small nonlinear drive term, η_0, this function reduces to the $sinc^2$ dependence of Eq.(4.1) and is a direct measure of the phase-matched conversion efficiency (13:576). For larger drives, the fundamental pulse is more strongly depleted, and the point where $\eta_0 = 1$ can be considered as the point where

saturation begins. This non-periodic function shows the strong dependence of this process on the beam parameters used. The contour plot shown in Figure 27 is very instructive in tracking the predicted conversion efficiency for different experimental arrangements.

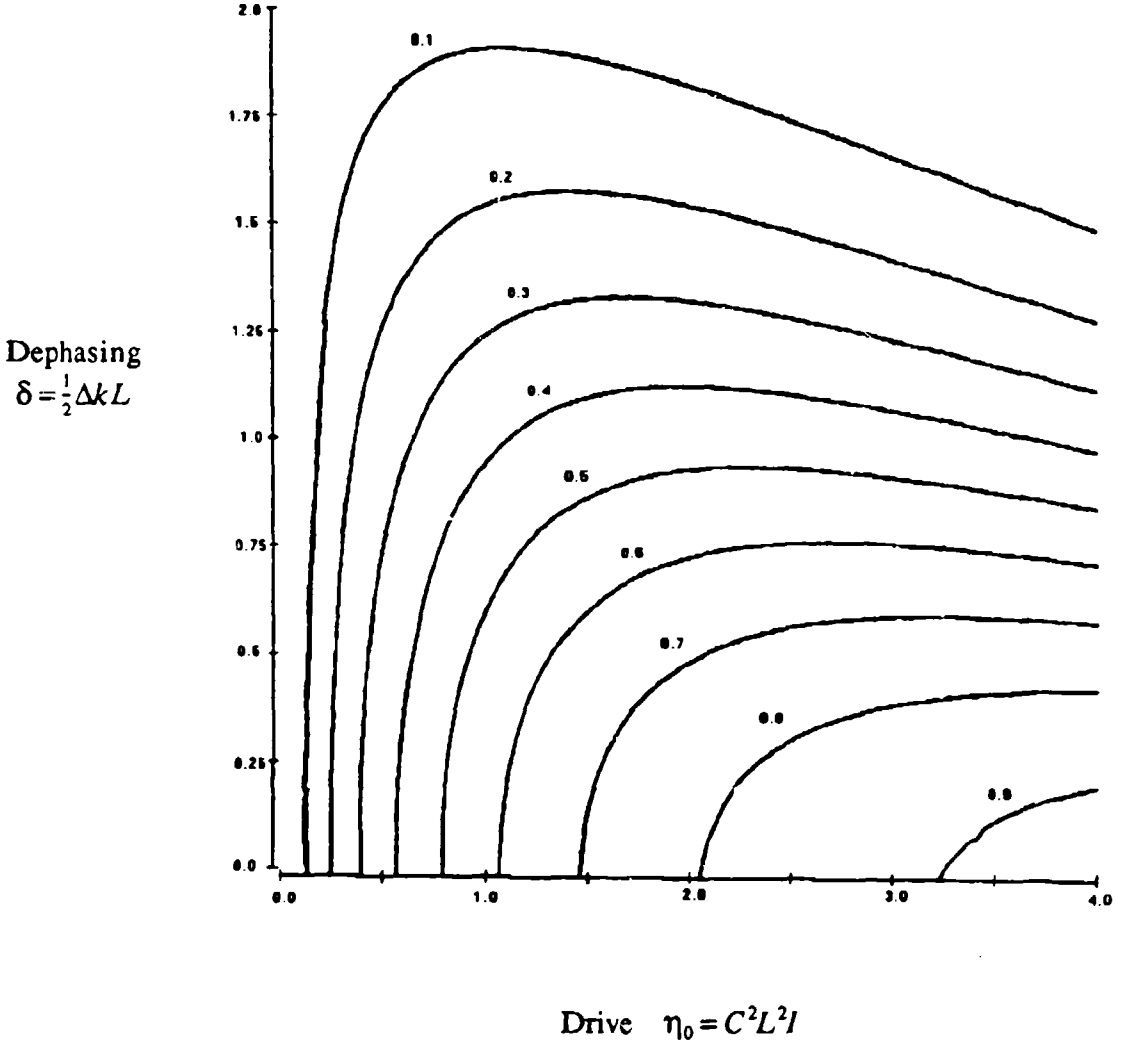

Figure 27. Contour plot of conversion efficiency as a function of the dimensionless drive and dephasing terms derived using the Jacobi elliptic. There are nine contours corresponding to efficiencies from 0.1 to 0.9 over the range of the plot.

The Jacobi elliptic function in Eq.(4.31) may be written explicitly as a series expansion (15:575) of the nome $q = \exp(-\pi K'/K)$ and the argument $v = \pi u/(2K)$

$$sn(u \mid m) = \frac{2\pi}{m^{1/2}K} \sum_{n=0}^{\infty} \frac{q^{n+1/2}}{1-q^{2n+1}} \sin(2n+1)v \tag{4.35}$$

The variables K and K' are functions of the real parameter m and may thus be written without the complex notation in K' as

$$K = \int_0^{\pi/2} \frac{1}{\sqrt{1-m\sin^2\theta}} d\theta \quad \text{and} \quad K' = \int_0^{\pi/2} \frac{1}{\sqrt{1-(1-m)\sin^2\theta}} d\theta \tag{4.36}$$

In general, the m in Eq.(4.35) must be less than one in order for the series to converge. Note the specific forms of the parameters of the Jacobi elliptic in Eqs.(4.32-33), where $1+\delta^2/4\eta_0$ will always be greater than one. By Jacobi's real transformation (15:573)

$$sn(u \mid m) = \mu^{1/2} sn(v \mid \mu) \qquad \text{where} \qquad m>0, \quad \mu = m^{1/2}, \quad v = um^{1/2} \tag{4.37}$$

Eq.(4.31) may be rewritten in the form

$$\eta = \tanh^2\left[\frac{1}{2}\tanh^{-1}\left(\frac{1}{\sqrt{1+\delta^2/4\eta_0}} sn\left[2\sqrt{\eta_0(1+\delta^2/4\eta_0)}, \frac{1}{\sqrt{1+\delta^2/4\eta_0}}\right]\right)\right] \tag{4.38}$$

where the nonlinear drive and dephasing terms are defined above.

Figure 27 describes the dependences of the efficiency on the crystal length, peak intensity (of the temporal and spatial profile) and the phase mismatch. If we consider the case of second harmonic generation at the phase matched angle, we will still have finite contributions to the dephasing from the far-field divergence half angle of the beam (in air), $\delta\theta$,

$$\Delta k = \beta_e \delta\theta + \beta'' \delta\theta^2 \tag{4.39}$$

For critically phase-matched materials, such as $AgGaSe_2$ whose the phase matching angle $\theta \neq \pi/2$, the first term dominates and Δk is linear in $\delta\theta$. For non-critically phase matched materials, $ZnGeP_2$ below 200°C, the first term goes to zero and the dephasing is quadratic in divergence.

In Figure 27, one may be misled to conclude that higher intensity levels will lead to better conversion efficiencies. Telescoping the beam down would provide this, but the increase is

accompanied by a corresponding increase in the divergence. As an estimate of the efficiencies expected with the focussing lenses and intensity levels proposed, note the relations between the beam and crystal dimensions in the nonlinear drive term

$$\eta_0 = C^2L^2I = C^2(L^2/area)P_{Peak} \tag{4.40}$$

where the *area* may be approximated by πw^2 at the center of the crystal. w may be interpreted as the minimum spot size in the focussed case. Doubling the dimensions of the beam and crystal has no affect on the drive (13:577). The peak intensity must, however, be chosen to avoid the damage thresholds of the material.

The dephasing term may be expressed as

$$\delta = \frac{1}{2}\Delta kL = \frac{1}{2}(\beta_0\lambda)Q \tag{4.41}$$

where Q is the beam quality and is the ratio of the far-field divergence half angle to the diffraction limited divergence (both taken inside the crystal)

$$Q = \frac{\delta\theta}{\delta_0} = \frac{\delta\theta}{\lambda/(\pi n w)} \tag{4.42}$$

By eliminating the crystal thickness from Eqs.(4.33-34), the condition for high efficiency (in excess of 50%), independent of the crystal length, is given by (13:577)

$$P_{Peak} \geq (\beta_0\lambda/C)^2 \ (\eta_0/4\delta^2) \cdot Q^2 \tag{4.43}$$

In $AgGaSe_2$ we can estimate this value with a few minor computations. The only assumption with regard to the spatial intensity (Gaussian) pattern of the beam will be in calculating the peak intensity of the pulse. If we consider the case of focussed second harmonic generation using a lens of focal length 12.5 cm, with a minimum spot size (peak intensity) as given in Figure 18, we can find the far-field divergence as one half of the numerical (or analytic) derivative of Eq.(3.8).

$$Q = \frac{\delta\theta}{\lambda/\pi n w} = \frac{10.39\text{mrad}/2}{10.6\mu m/(\pi(2.5915)(125.3\mu m))} = 0.500 \text{ rad} \tag{4.44}$$

The other factors work out as follows:

$$\beta_\theta = \frac{\omega}{c}\sin(2\theta_m)\frac{(n_e^{2\omega})^{-2} - (n_o^{2\omega})^{-2}}{2(n_o^{\omega})^{-3}} \qquad \text{for} \quad n_e < n_o \tag{4.45}$$

$$\beta_\theta = \frac{1.77\times10^{14}\text{rad/sec}}{3\times10^{8}\text{m/sec}}\sin(2\cdot 0.9603\text{rad})\frac{(2.5809)^{-2} - (2.6136)^{-2}}{2(2.5^{0}15)^{-3}} = 18089.76\text{rad/m}$$

Note that β_θ, as written, is not a function of the crystal length.

$$C = \frac{5.46 \quad d_{36} \quad \sin\theta_m \quad [\text{pm/V}]}{\lambda \quad [\mu m] \quad (n_1 n_2 n_3)^{1/2}} \tag{4.46}$$

$$C = \frac{5.46 \cdot 43\text{pm/V} \quad \sin(0.9603\text{rad})}{10.6\mu m \cdot (2.5915)^{3/2}} = 4.3502 \quad \text{GW}^{-1/2}$$

For a nominal average power of 5 Watts, the peak intensity can be extracted from Figure 20,

$$\eta_0 = C^2 I L^2 = C^2 L^2 \frac{P_{Peak}}{\pi w^2} \tag{4.47}$$

$$\eta_0 = (4.3502 \quad [\text{GW}^{-1/2}])^2 \quad (0.029\text{m})^2 \quad 87.21 \quad [\text{GW/m}^2] = 1.388$$

$$\delta = \frac{1}{2}\Delta k L = \frac{1}{2}\beta_\theta \delta\theta L \tag{4.48}$$

$$\delta = \frac{1}{2}(18089.76\text{rad/m})(5.195\text{mrad})(0.029\text{m}) = 1.363\text{rad}^2$$

Finally, inserting all of the terms into Eq.(4.43),

$$P_{Peak} \geq \left(\frac{18089.76\text{rad/m} \quad 10.6\mu\text{m}}{4.3502\text{GW}^{-1/2}}\right)^2\left(\frac{1.388}{4(1.363\text{rad}^2)^2}\right)(0.500\text{rad})^2 = 9.076\times10^{-5}\text{GW} \tag{4.49}$$

which says that the peak power in the pulse must be greater than 90.7kW in order to achieve high conversion efficiency in this configuration. In our case, the peak powers range for 4kW to 8kW and we will not observe conversion efficiencies quite this high.

In order to maximize the efficiency, we wish to operate with as small of a dephasing term as

possible while maintaining a value for the nonlinear drive term as near to optimum as possible, but below the damage threshold. In actuality, this configuration for $AgGaSe_2$, given the available power and the 12.5 cm focal length lens, is near optimum.

Improvements to Plane Wave Solutions - Radial Intensity Profile

In both of the solutions above, the spatial intensity profile of the CW beam or pulse was assumed to be constant. In the initial derivation of the efficiency calculations, we are able to include this variation in a rather simple fashion by rewriting Eq.(2.15) as (23:528)

$$|E^{(2\omega)}|^2 = \frac{4\mu_0}{\varepsilon}\omega^2(d_{ijk}')^2|E^{(\omega)}|^4L^2\frac{\sin^2\frac{1}{2}\Delta kL}{\left(\frac{1}{2}\Delta kL\right)^2} \tag{4.50}$$

where

$$E_{1i}^2 := E_{1k}^2 = E^{(\omega)}(r) \equiv E_0e^{-r^2/w_0^2} \tag{4.51}$$

If we allow the power in the fundamental to be described by

$$P^{(\omega)} = \frac{1}{2}\sqrt{\frac{\varepsilon}{\mu_0}}\int\int_{\text{cross section}}|E^{(\omega)}|^2dxdy = \sqrt{\frac{\varepsilon}{\mu_0}}E_0^2\frac{1}{4}\pi w_0^2 \tag{4.52}$$

w_0 is the minimum beam waist for the focussed case. Combining Eq.(4.50) and Eq.(4.52)

$$\eta = \frac{P^{(2\omega)}}{P^{(\omega)}} = 8\left(\frac{\mu_0}{\varepsilon_0}\right)^{3/2}\frac{\omega^2(d_{ijk}')^2L^2}{n^3}\frac{P^{(\omega)}}{\pi w_0^2}\frac{\sin^2\frac{1}{2}\Delta kL}{\left(\frac{1}{2}\Delta kL\right)^2} \tag{4.53}$$

which is identical to Eq.(4.1) except that it was derived for a Gaussian beam input with $z_0 \gg L$, and is accounted for in the factor area $=\frac{1}{4}\pi w_0^2$ (13:530). z_0 is the Rayleigh range defined by $z_0 = \pi w_0^2 n/\lambda$. This solution is applicable to focussed second harmonic generation as suggested in Figure 28.

The efficiency will increase with the length of the crystal up to the point where $z_0 \equiv L$, at which point the divergence of the beam over the length of the crystal becomes appreciatable. The optimum condition exists for $z_0 \equiv L/2$ (22:217). For the case of $AgGaSe_2$, with a lens of focal length 12.5 cm placed 50 cm from the laser

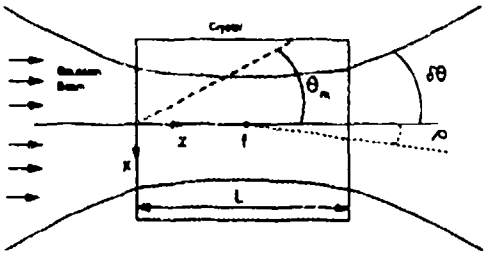

Figure 28. Gaussian beam focussed inside a nonlinear optical crystal.

$$L \cong 2[\pi(125.3\mu m)^2(2.5915)]/10.6\mu m = 2.412 \text{ cm} \tag{4.54}$$

which suggests that a slightly weaker focussing case would bring us closer to the optimum efficiency. This agrees with the exact analysis in the sense that with a large focussed spot size, we would have a lower divergence (and dephasing term) leading to higher overall efficiencies. Eq.(4.53) is applicable for relatively short crystal lengths at moderate intensity levels in the CW harmonic generation.

For pulsed second harmonic generation, the exact solution (Eq. (4.38)) does not easily lend itself easily to folding in the radial intensity distribution of the beam. A rough approximation can be achieved by segmenting the radial pattern into discrete rings at different intensity levels, weighting their contribution to the total efficiency by the amount of energy in each and summing the components. We can describe the Gaussian radial intensity distribution by

$$I^{(\omega)}(r) = I_{Peak} e^{-r^2/w_0^2} \tag{4.55}$$

We can then sum a series of discrete evaluations of the efficiency using the exact solution and weight each by the integral of the total power in Δr by

$$\eta_{Total} = \sum_{r=0}^{\infty} \frac{\eta(I^{(\omega)}(r))_{Exact}}{\pi w_0^2} \int_0^{2\pi} \int_r^{r+\Delta r} \rho \exp(-\rho^2/w_0^2) \, d\rho \, d\theta \tag{4.56}$$

The steps, Δr, and final value for the summation in r are determined to yield an accurate result in a reasonable amount of computation time.

Numerical Approximation to the Focussed Beam Solution

Implicit in the previous derivations was the assumption that the focussed spots at the fundamental and second harmonic frequencies overlap over the entire length of the crystal. Recall from the discussion of the anisotropic properties of these crystals, one of the two orthogonally polarized beams may walkoff from the other. This deviation is accounted for in the solution presented below which numerically tracks the spatial development of the field at 2ω over the length of the crystal. It takes into account diffraction, double refraction and absorption exactly within the limit of the paraxial approximation.

Following the development in Boyd (5:3600) and Eckardt (12:5), we define the conversion efficiency in Eq.(4.57) in terms of the integral expression shown in Eq.(4.61). This theory was originally developed for CW second harmonic generation (5:3600) and has been modified for the pulsed case with two different approximations. Assuming a Gaussian shaped pulse in time, a factor of $1/\sqrt{2}$ was introduced to derive an effective average power over the length of the exposure. A second factor, R_{Sat}, was used to account for saturation of the medium (10:925).

$$\eta = \left\{2\sqrt{2}\left(\frac{\omega_1 d_{eff}}{nc}\right)^2\left(\frac{1}{\varepsilon_0 c \lambda_0}\right)\right\} R_{Sat} e^{(-\alpha' L)} L P_1(0) h(\sigma, \beta, \kappa, \xi, \mu) \tag{4.57}$$

where

ω_1	Fundamental frequency, *radians/sec*
d_{eff}	Effective nonlinear coefficient, *m/V*
λ_0	Free space wavelength, *m*
L	Length of the crystal, *m*
n	Nominal index of refraction

The fundamental power at the peak of the temporal profile is defined by,

$$P_1(0) = \frac{P_{Average}}{\sqrt{\pi}\tau\nu_{rep}} \tag{4.58}$$

where τ is the $1/e$ point of the pulse (characteristic time) and ν_{rep} is the pulse repetition frequency. Saturation is accounted by

$$R_{Sat} = \frac{\eta_{calc}}{\eta_{calc}+1} \tag{4.59}$$

This factor is ge erally included once the rest of the computations have been completed and leads to a favorable approximation of the pulsed efficiency up to about 50%. We go on to define

$$h(\sigma,\beta,\kappa,\xi,\mu) = (\pi^2/\xi)e^{\mu\alpha L}F(\sigma,\beta,\kappa,\xi,\mu) \tag{4.60}$$

$$F(\sigma,\beta,\kappa,\xi,\mu) = \frac{2}{\sqrt{\pi}}\int_{-\infty}^{\infty}|H(\sigma+4\beta s,\kappa,\xi,\mu)|^2\exp(-4s^2)ds \tag{4.61}$$

We can define $\sigma' = \sigma + 4\beta s$ such that (5:3602)

$$|H(\sigma',\kappa,\xi,\mu)|^2 = \frac{1}{4\pi^2}[R(\sigma',\kappa,\xi,\mu)^2 + I(\sigma',\kappa,\xi,\mu)^2] \tag{4.62}$$

The real and imaginary parts (17:379) may be written as

$$R(\sigma',\kappa,\xi,\mu) = \int_{-\xi(1-\mu)}^{\xi(1+\mu)}\frac{d\tau}{1+\tau^2}(\cos\sigma'\tau + \tau\sin\sigma'\tau)e^{-\kappa\tau} \tag{4.63}$$

$$I(\sigma',\kappa,\xi,\mu) = \int_{-\xi(1-\mu)}^{\xi(1+\mu)}\frac{d\tau}{1+\tau^2}(\sin\sigma'\tau - \tau\cos\sigma'\tau)e^{-\kappa\tau} \tag{4.64}$$

The parameters are defined as;

$$\sigma = \frac{1}{2}b\Delta k \quad \text{, phase mismatch} \tag{4.65}$$

$$\beta \approx B\xi^{-1/2} \quad \text{, ratio of } \rho/\delta_0 \tag{4.66}$$

$$\kappa = \frac{1}{2}\alpha b \quad \text{, absorption} \tag{4.67}$$

$$\xi = L/b \quad \text{, focussing parameter} \tag{4.68}$$

$$b = w_0^2 k_1 \quad \text{, confocal parameter} \tag{4.69}$$

$$\mu = (L - 2f)/L \quad \text{, focal position} \tag{4.70}$$

$$\alpha = \alpha_1 - \frac{1}{2}\alpha_2 \quad \text{and} \quad \alpha' = \alpha_1 + \frac{1}{2}\alpha_2 \tag{4.71}$$

α_1 and α_2 are the absorptivities at the fundamental and second harmonic respectively and w_0 is the focussed minimum spot size. The integral generally yields a single peak for a given value of the double refraction parameter,

$$B = \rho(Lk_1)^{1/2}/2 \tag{4.72}$$

where ρ is the walkoff angle in radians, and k_1 is the propagation constant inside the media. This theory is written for the case of negative uniaxial crystals and may be extended to the positive uniaxial case. These computations may be completed using Romberg integration routines for both of the expressions above (See Appendix B).

For a specified crystal type and physical dimensions, this expression yields a single maximum for the optimum focussing conditions. Our $AgGaSe_2$ crystal, which is 2.9 cm in length, has a walkoff angle of 11.69 mrad and $B = 1.234$. The corresponding optimum focussing parameter, extracted from Figure 4 of Boyd, is $\xi = 1.775$ which leads to an optimum focussed spot size of

$$w_0 = \sqrt{\frac{L\lambda}{2\pi n \xi_m}} = \sqrt{\frac{0.029\text{m} \quad 10.6\mu\text{m}}{2\pi(2.5915)(1.775)}} = 103.1 \quad \mu m \tag{4.73}$$

This value is smaller than that predicted earlier by the confocal focussing condition, and is smaller than the set-up involving the 12.5 cm focal length lens placed 50 cm from the laser. We can easily reach this value by moving the lens further from the CO_2 source ($z_2 = 65$cm, and this was accomplished in the latter portions of the experiment.

For the 1.1 cm sample of $ZnGeP_2$ heated to 211°C, at the critically phase matched angle of 85.1°, $\rho = 0.13^0$ and $B = 0.155$, leads to an optimum focussing parameter of $\xi_m = 2.82$. This yields an optimum spot size of 74.8μm which can be achieved with the available experimental setup.

Heating Estimates and Damage Thresholds

As a precursor to the actual experiments, a first order study of the heating in the crystal caused by the absorption of the fundamental as a function of the average input power was conducted. The temperature rise can be estimated by the amount of energy absorbed at a particular point over a specified time duration via the heat capacity, C, and absorptivity of the material of mass m by

$$\Delta T = \frac{\Delta Q}{mC} \tag{4.74}$$

ΔQ is the amount of energy absorbed and we will relate it to the power by considering a 1 sec exposure to the beam. We use the time averaged energy, or power, because of the very high repetition rates of the CO_2 source. If we consider the absorptivity to be constant, we can integrate the total energy absorbed in 1 mm thick slices along the length of the crystal by

$$\Delta Q(l) = P_{Avg}\Delta t \int_{l}^{l+\Delta l} [\exp(-\alpha l) - \exp(-\alpha(l+\Delta l/10))]\ dl \tag{4.75}$$

where l can range from 0 to L = 29 mm, $\Delta l = 0.1$ mm, $\Delta t = 1$ sec and the absorptivity is defined per millimeter. If we were to integrate this expression over the length of the crystal, we would get the total energy absorbed.

To fold in the radial dependence of the energy distribution, we considered the energy absorbed by a particular segment of the crystal and write in the from of a radial Gaussian distribution as

$$Q(r,l) = \frac{Q(l)}{\pi w^2}\ e^{-r^2/w^2} \tag{4.76}$$

Finally the temperature profile at a given point within the crystal as a function of radius may be written

$$\Delta T(r,l) = \frac{Q(l)}{\pi w^2(mC)}\ e^{-r^2/w^2} \tag{4.77}$$

The heat capacity is generally given in J/mole/°C and the mass, m, can be found from the density of the material and the given area of integration (consider a long cylinder where the cross-sectional area cancels out in the computation). For the case of the AgGaSe2 crystal, with $C = 104$J/mole/°C and $\rho = 5.7$g/cm^3, the temperature profile for three spot sizes, w, at the center of the crystal with $\alpha = 0.0027$ /mm are shown in Figure 29.

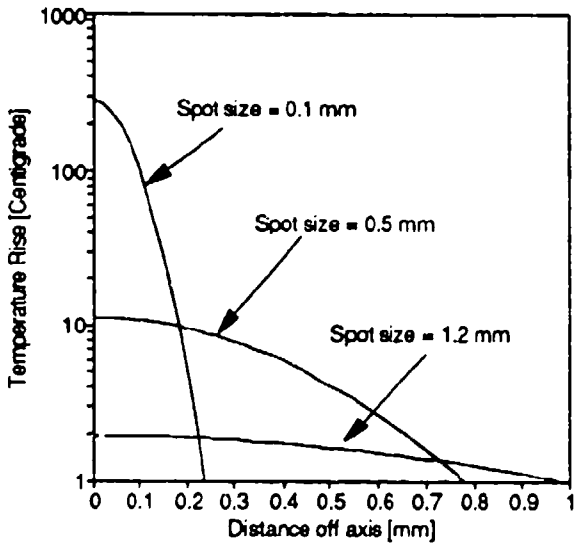

Figure 29. Temperature profiles for a one second exposure at 30 kHz, nominal average power of 6.0 Watts at the center of the $AgGaSe_2$ crystal. Note that conduction of the heat was not considered in this estimate.

These profiles appear very steep, as they are shown for the center 0.2 mm radius of the beam, and although no thermal conductivity was taken into account, we can expect reasonably high stress within the material when exposed to these kinds of power. A more rigorous exploration would relate the energy absorbed to the thermal conductivity and expansion coefficients to deduce the stresses. For our purposes, this gives us a feel for limiting the exposure durations at high powers in light of the anticipated temperature build up.

From the variety of analytic and numerical approximations to the expected conversion efficiency, we can now estimate the optimum experimental parameters under which to test and

characterize the materials. The heating studies only give us a crude idea of the stresses on the material but are useful in comparing to known damage thresholds of the two crystals. These will be reviewed in the next chapter with the experimental method.

V. Experimental Procedure

With the review of the theoretical calculations in hand, we are able to describe the experimental methods employed in determining each of the figures of merit. The various dependences of the conversion efficiency on the peak and average powers, direction of propagation and focussing were further explored.

As noted in the derivation of the effective nonlinear coefficients, the conversion efficiency of both crystals will be heavily dependent upon the direction of propagation with respect to the optic axis, θ, and relatively insensitive to the angle ϕ. The critically phase matched $AgGaSe_2$ will have a very small angular acceptance and demand precise movement about the crystal's central axis to accurately measure the conversion efficiency's dependence on this angle. We anticipate being able to measure SHG in the non-focussed and focussed cases as functions of angle of incidence with respect to the principal axes, intensity levels (position of the crystal with respect to the lens) and dephasing (different lenses).

The experiments with $ZnGeP_2$ will prove a bit more involved due to the requirement for temperature tuning. Physically mounting the heating oven will restrict the limits of angular deviation from perpendicular to the face. Recall, this is a non-critically phase-matched material over a reasonably large temperature range, but we anticipate extremely low conversion efficiencies due the magnitude of d_{eff} near $\theta = \pi/2$. We do not anticipate observing any second harmonic with the low intensity levels of the non-focussed case, thus these experiments will be restricted to the focussed case only. Additionally, in order to boost d_{eff}, we must elevate the temperature of the crystal so that $\theta_m < \pi/2$. The major disadvantage this produces is that the material becomes critically phase-matched and these oblique angles of incidence will prove more difficult to align with the oven in place.

Non-Focussed Second Harmonic Generation in $AgGaSe_2$

The initial experiments were conducted without the use of a focussing element in order to compare the results to the theoretical calculations involving the plane wave solutions as well as to avoid any unforeseen heating or damage mechanisms that may have been encountered.

From the calculated spot size and peak intensity values for the unfocussed laser beam, at these relatively low intensity values, the closer we operate to the output port, the higher the conversion efficiency. We must also consider the physical size of the crystal face in order to ensure that most of energy traverses the crystal's length without being clipped. If the spot size is less than one quarter of the width of the crystal face, 2.25 mm, approximately 98% of the energy will pass through the crystal. This restricted the operating distance to within 15 cm of the output port of the laser. In Figures 30 and 31, the measurements of the unfocussed conversion efficiency were taken at this point.

An electrically operated mechanical shutter was incorporated into the design in order to limit the exposure durations. It was generally repeatable to within ±0.05sec for exposures longer than 0.5 seconds. The timing and actuator circuit was foot activated and had to be isolated from the power sources within the room in order to reduce the EMI produced. In later experiments, the exposure duration was directly measured with a small HeNe laser and photovoltaic detector.

In the non-focussed experiments, two methods were used, the difference being that the first involved a series of energy measurements using a single detector and the second involved power measurements using two detectors. Initially, we were not able to acquire two energy meters and were forced to conduct the energy experiment with a single 1" disk calorimeter. Note Figure 30, where the energy in the fundamental was measured for the 0.5 sec exposure before and after the crystal was placed on the stage. The energy at the second harmonic was recorded and compared to these fixed values to derive an efficiency as a function of the angle θ.

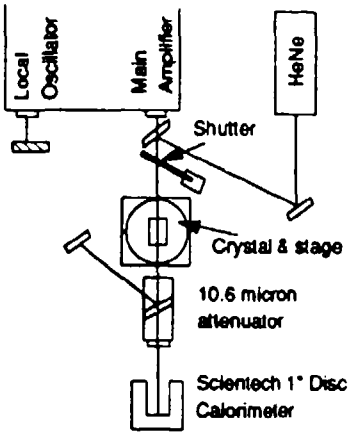

Figure 30. Experimental set-up for measuring the non-focussed conversion efficiency as a function of angle of incidence, θ, using energy measurements of a single meter.

The second set of measurements at this same distance were taken in terms of power. Figure 31 shows the second calorimeter, a 1" diameter Coherent Radiation laser power head and meter, was used to measure the fundamental reflected from the 10.6 μm attenuator (discussed later) after it passed through the crystal. By taking into account the absorptivity of the crystal, this can be used to relate the power incident to the second harmonic power produced. At these very low efficiencies, depletion of the fundamental was be negligible.

Note the small laser used for alignment purposes in all of these experiments was a 1.0 mW HeNe operating at 547 nm. Since the CO_2 beam is difficult to track through the system without disturbing the optics, the visible alignment laser was an essential tool.

After the beam passed through the crystal, the second harmonic and fundamental were separated by the filter stack composed of a 10.6μm reflective interference coating (reflects 99% of the fundamental) on a ZnSe substrate, followed by a 1/8" thick sapphire plate. The sapphire plate blocks all wavelengths longer than approximately 6μm. The transmission spectrum of this filter stack was measured using a FTIR and is shown in Figure 32. In recording

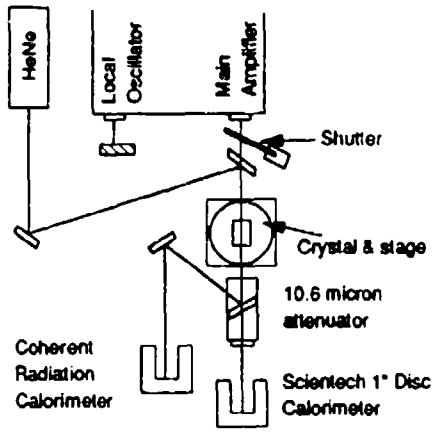

Figure 31. Experimental set-up for measuring the non-focussed conversion efficiency as a function of angle of incidence, θ using power measurements with two meters.

the background and sample scan with the FTIR, a polarizer aligned parallel to the anticipated output polarization of the second harmonic (parallel to the table top) was placed in the path of the beam. This helped to remove the ambiguities in the transmission introduced by the use of an interference filter.

The mounting stage provided control of the angular orientation θ to within ±3 min and ϕ to ±0.5 min. An absolute measure of the distance between the laser and the crystal face could be made with an accuracy of ±1 mm while relative measurements made with a micrometer stage were ±0.005 mm. Lateral movement of the crystal was included to compensate for the movement of the crystal face as it was slewed about its central axis. As a reference point, note Figure 33 which depicts the various axes and directions of movement over which we had control. They are denoted by letters for reference in Chapter IV.

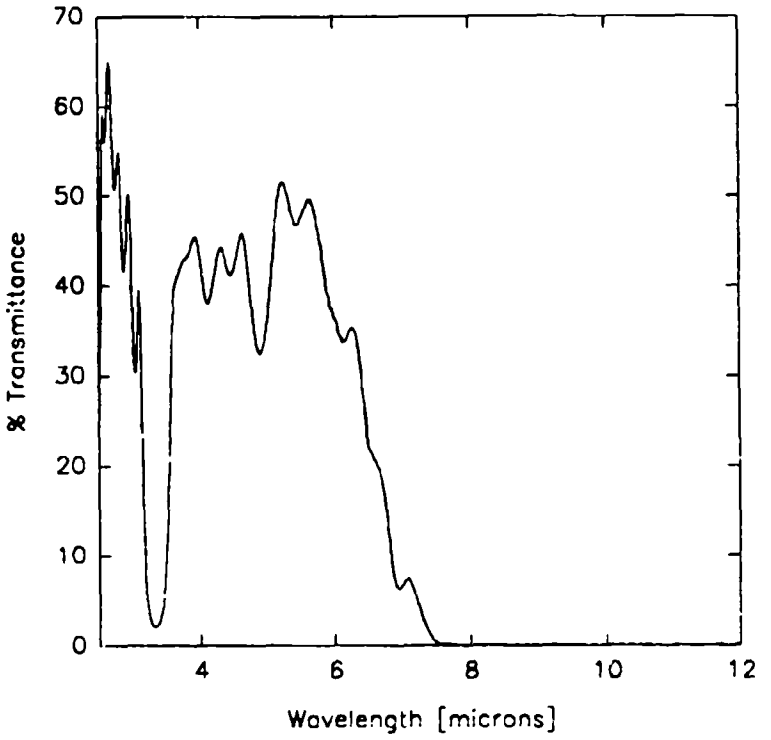

Figure 32. Infrared transmission spectrum of the pair of filters used to block the fundamental wavelength at 10.6 μm and pass the second harmonic at 5.3 μm where the transmission is 49.8%.

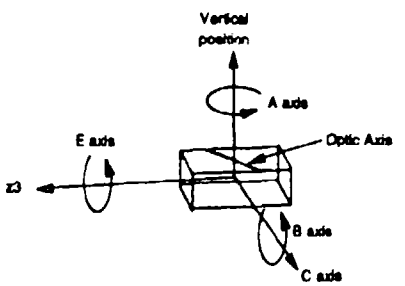

Figure 33. Diagram showing the axes of rotation and translation for the $AgGaSe_2$ crystal.

At the point of peak conversion efficiency, the temporal waveforms of the fundamental and second harmonic were recorded using the high speed LN_2 cooled HgCdTe detectors. The detectors were simply placed where the calorimeter heads resided and at these moderate conversion efficiencies, the signal strength of the second harmonic was at the appropriate level for detection. It is interesting to note the resonant cavity detectors cut for the fundamental wavelength were very sensitive to the 5.3 μm radiation as well.

The procedure for taking each of the measurements included several steps. The energy meters tended to drift with the thermal fluctuations in the room caused by air flows especially when taking measurements on the more sensitive ranges (0.01 J or less). They required continuous observation despite their isothermal enclosures. Once they had settled on a reliable zero reading, the next step was to ensure the laser was running in a stable mode. This was done by observing the loop error meters monitoring the piezoelectrically controlled mirrors of the three oscillators. Once both the meters and laser were stabilized, the crystal, in the proper orientation, was exposed by depressing a foot switch to activate the mechanical shutter. The energy in the fundamental and second harmonic were then recorded. The meters were reset and the zero points observed to ensure no fluctuations had taken place during the exposure.

Focussed efficiency measurements of $AgGaSe_2$

In the design of the focussed beam experiments, we are given greater flexibility in arranging the components since the constraints on the placement of the crystal with respect to the laser have been lifted. The initial bulk of the experiments were conducted with the focussing element 50 cm from the laser since at this distance, the spot size of the laser is just less than 1/4 of the diameter of the 1" diameter ZnSe positive meniscus focussing lens. Also, the calculated values for the peak and average intensities would be below published damage thresholds for $AgGaSe_2$. In previous studies, the surface damage for an uncoated sample occurred for a peak intensity level of 12 MW/cm^2 (11:788) in a single pulsed mode and 14.7 MW/cm^2 (12:10) in a repetitively pulsed format. The average power damage thresholds at the high repetition rates

was given as 19.4 kW/cm^2 given a spot size a the crystal face of 164μm (12:10). In the case of the 12.5 cm focal length lens, with a minimum focussed spot size of 125.3 μm (placed 50 cm from the laser), the average power seen at the crystal face would have to exceed 9.6 W in order to reach the average power damage threshold. The average power at 30kHz seen through the focussing lens is below 6 Watts.

Energy measurements using 1 second exposures were used in the initial investigations. In order to investigate any transient heating effects during exposure, a copper-constantine thermocouple was incorporated into the crystal mount and the temperature was recorded during various exposures. The thermocouple was sensitive to ±0.1°C changes in temperature and there was no obse vable rise during exposures ranging up to 5 seconds in duration. For this reason, average power measurements of the conversion efficiency were conducted as well. Here, exposures up to 20 seconds were taken as the meters at points I and II (set to measure power) settled on the average power readings.

Since the average energy from the laser tended to fluctuate slowly over time, the energy, or power, incident on the crystal was measured as a function of that reflected from the beam splitter placed near the shutter (Note Figure 34). Without the crystal in place, the energy detected at point II was calibrated against that detected at point I over a given exposure duration. The energy could be related to the average power using this exposure time and a similar calibration between the two meters with the shutter held open. This calibration was conducted with each set of experiments in order to ensure the accuracy of the results.

The physical arrangement of the experimental apparatus is shown in Figure 34. With the additional room provided by placing the lens far from the laser, we were able to incorporate several other elements to control the beam. The ZnSe beamsplitters were used to vary the peak and average intensity levels while the chopper, shown near the mechanical shutter, allowed for adjustment of the average intensity without affecting the peak intensity of the transmitted power.

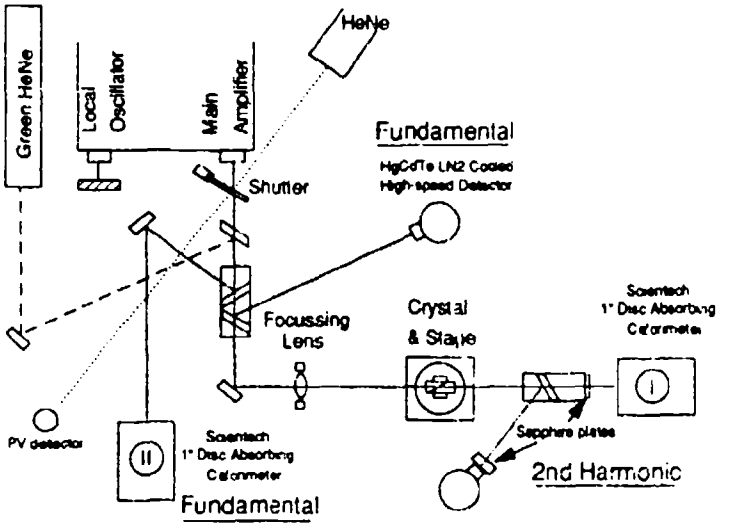

Figure 34. Experimental arrangement for the focussed beam conversion efficiency measurements in $AgGaSe_2$.

The second HeNe laser was used to measure the exposure duration. When the shutter was open, the signal detected by the silicon photovoltaic detector was viewed on an oscilloscope and the FWHM measured.

The HgCdTe detectors were used to measure the relative temporal profiles of the fundamental and second harmonic at various intensity levels and crystal orientations. The sapphire plate in front of one of the detectors indicates which was used to record the 5.3 μm signal.

Recording the spatial profiles of the fundamental and second harmonic was a straight forward procedure of placing the pyroelectric vidicon camera in the position of the energy meters and adjusting the intensity of the beam to the appropriate level for a non-saturated response.

The procedure for exposure was the same as that for the non-focussed case. Variations in the chopper frequency and duty cycle were investigated as well.

Focussed Efficiency Measurements of $ZnGeP_2$

In the case of $ZnGeP_2$, the temperature controlled oven was incorporated into the design. From the calculations of d_{eff}, the direction of propagation with respect to the optic axis, θ,

would be the crucial determinant of the conversion efficiency. Near the noncritical phase-matching angle and temperature, we expect very poor results and are forced to go to higher temperatures. Although at these temperatures the material is critically phase-matched, we hoped to observe some output as the temperature passes through the phase-matching point for a given orientation. The feedback loop for the oven control circuit is shown in Figure 35.

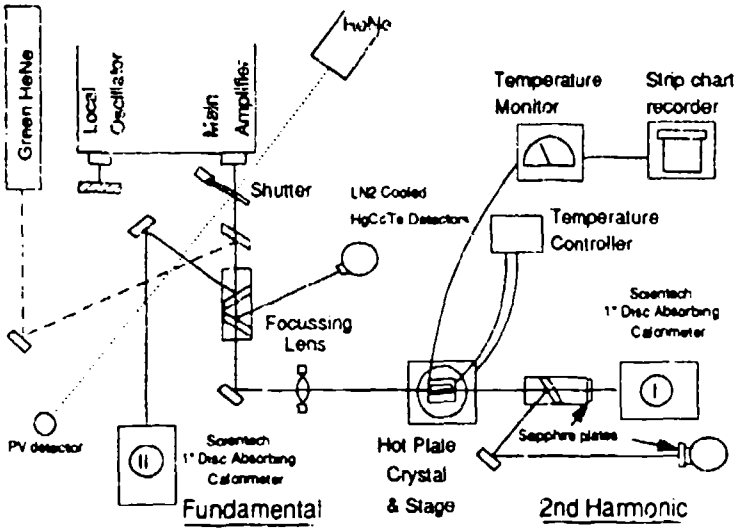

Figure 35. Experimental arrangement for the focussed beam conversion efficiency measurements in $ZnGeP_2$.

The hot plate is operated in a full on/off manner by a single set point thermistor gauge monitor reading the temperature with a copper-constantine thermocouple mounted near the crystal in a copper heat sink. During initial warm-up there is a fair amount of overshoot in temperature because of the thermal mass of the hot plate and copper block. Once settled, the thermistor is able to maintain a set temperature to with $\pm 5^{\circ}C$. A second thermocouple mounted on the opposite side of the crystal monitors the temperature at this point with an output connected to a strip chart recorder.

The crystal orientation may be varied in θ (an external angle in this case) up to approximately 15^{0} where the hot plate begins to obscure the beam impinging on the crystal.

The internal angle, θ, at this point is $\theta_{outside}/n_{ZnGeP_2} \cong 0.087 rad$, or 5° of arc. The phase matching temperature at this point is 211°C and is easily attainable with this hot plate. There were no windows around the crystal to help maintain a low temperature gradient, so the overshoot in the temperature control may have been to our advantage.

Once the orientation and position of the crystal behind the lens was set and the temperature was near the critical value the exposure procedure was the same as the previous cases.

Damage Studies of $AgGaSe_2$

Damage point data for $AgGaSe_2$ is limited in the open literature due to the expense and rarity of the material at this point. The threshold values may vary widely with crystal quality, surface coatings and in some instances, interplay between the average and peak power damage mechanisms. There may be instances where it is influenced by long term fatigue due to repeated exposures at the same point. Although damage occurred with the original sample at two points in the efficiency measurements, small witness samples were provided with coated and non-coated surfaces for this specific purpose of determining these thresholds.

The published threshold limits may be reached or exceeded by using the 6.05 cm focal length Ge lens or by moving the 12.5 cm focal length ZnSe lens to a point further from the laser. For each of the samples it is then a matter of translating their position with respect to the position of the focus until damage occurs. The threshold can be characterized in terms of peak and average intensities, spot size and burn spot diameters.

The experimental procedures outlined here provide a reference for the results and discussion of the measurements taken. The specifics of each case are included and generally involve the adjustment of the intensity level of the beam or the crystal orientation in various manners.

VI. Results and Discussion

With these developments, we are able to compare the experimental and theoretical results under different conditions.

Non-Focussed Second Harmonic Generation with $AgGaSe_2$

The first exposures of the $AgGaSe_2$ crystal were conducted in the non-focussed case, 15.2 cm from the output port of the laser, with an average input power of approximately 8.2 Watts. Energy measurements were limited to one-half second exposures, and in this case, there was not a second energy calorimeter available to monitor the energy at the fundamental. The efficiencies extracted were referred to measurements of the energy at the fundamental before and after the experiment without the crystal in place. This added uncertainty is reflected in the calculated error bars as well as some odd behavior in the data points shown in Figure 36.

With these results, we can compare the theoretical estimates of the conversion efficiency developed in Chapter IV. We note that the simple theory, Eq.(4.1), is directly applicable while the exact solution, Eq.(4.38), must be modified slightly to incorporate the angular phase mismatch. This can be accomplished by rewriting the dephasing term, Eq.(4.33) as

$$\delta = \frac{1}{2}\Delta k L = \frac{1}{2}(\beta_\theta \delta\theta + 2\beta_\theta(\theta - \theta_m)) \tag{6.1}$$

Using this form, Eq.(4.1) and Eq.(4.38) can be directly compared. As we note in Figures 36 and 37, a constant multiplier is used with each to account for deviations between the measured and calculated values. Although the direct results of these calculations are on the same order of magnitude as the data, they are difficult to compare to the data without these correction factors.

The drop in the efficiency at the angle 0.01^0 can most likely be attributed to a variation in the laser power. Note that the data points in Figure 36 are shown a function of the deviation from the phase-matched angle which was assumed to lie at the peak of this pattern. This angle

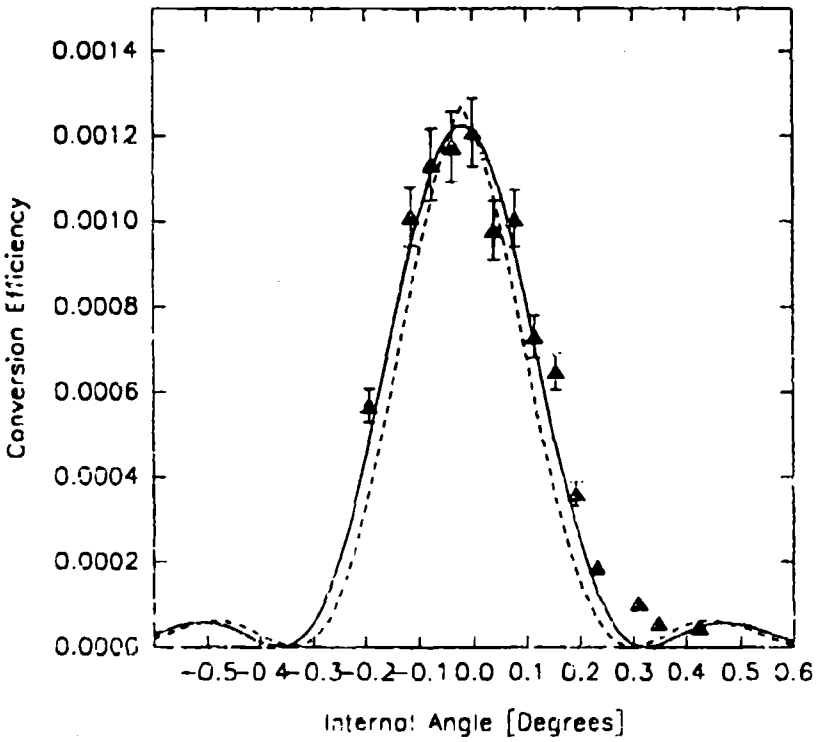

Figure 36. Efficiency as a function of the internal angle of propagation, θ, using energy measurements of the non-focussed second harmonic generation in *AgGaSe*$_2$. Distance from the laser was 15.2 cm, with an average input power of 9.53 W. The data points are shown as the filled triangles along with the calculated error bars (2:59). (———) Fit to the data using Eq.(4.1) modified by a factor of 0.27. (---------) Fit to data using Eq.(4.38) modified by a factor of 0.17.

was 5.25° ± 0.05° away from perpendicular to the face in the direction of the optic axis. The manufacturer cut the crystal for a phase-matched angle of 57.17°, which would lead to a phase-matched input at 10.805 μm (Note calculations in Chapter IV). At 10.6 μm, if we divide 5.25° by the index of refraction, 2.5915, the peak of the efficiency pattern (55.14°) agrees well with the phase matched angle of 55.02° calculated from the Sellmeier equations. The oblique angle of incidence pays off in the sense that there is no feedback to the laser by the energy reflected from the crystal surface.

The asymmetric appearance of the measured pattern about the phase matched angle can be

accounted for in a number of ways. The fact that the phase-matched angle does not lie perpendicular to the face may account for some this, but the majority is due the variation in the average output power of the laser source. This was not directly measured in this set-up due to the lack of a second energy meter.

Noting that the short exposures had no damaging effects on the crystal, the same experiment was repeated taking power measurements instead. In this case we were able to track the input power at the fundamental using a second power meter. This removed the uncertainty in the input power levels and led to a more symmetric set of points about the phase-matched angle (Figure 37).

The average power of 7.0 W is lower than the previous set of measurements, but the efficiencies are comparable. We note the width of this pattern is a bit larger than the calculated value. This may be due to crystal inhomogeneity or heating affects during these long exposures.

The width of the pattern calculated using the exact solution drops off with a steeper slope about the center peak than Eq.(4.1), but both display the $sinc^2$ dependence found in the original developments.

All of the calculations fall in the same order of magnitude of as the measured data, but each suffers different combinations of assumptions and approximations. These may attributed to several sources. The published values for the nonlinear optical coefficients vary by nearly a factor of two (11:788). At oblique angles of incidence, less energy than calculated may be passing into the crystal, although the anti-reflection coatings should significantly reduce this problem. Finally, the beam may be clipped by the physical extent of the crystal face resulting in a lower overall conversion efficiency.

If we include the radially dependent intensity profile in the exact solution (Eq.(4.56)), the efficiency calculated for an average power of 7.0 W, using the far-field half angle divergence at the phase-matched angle is 0.29%. At these extremely low values of efficiency, this esti-

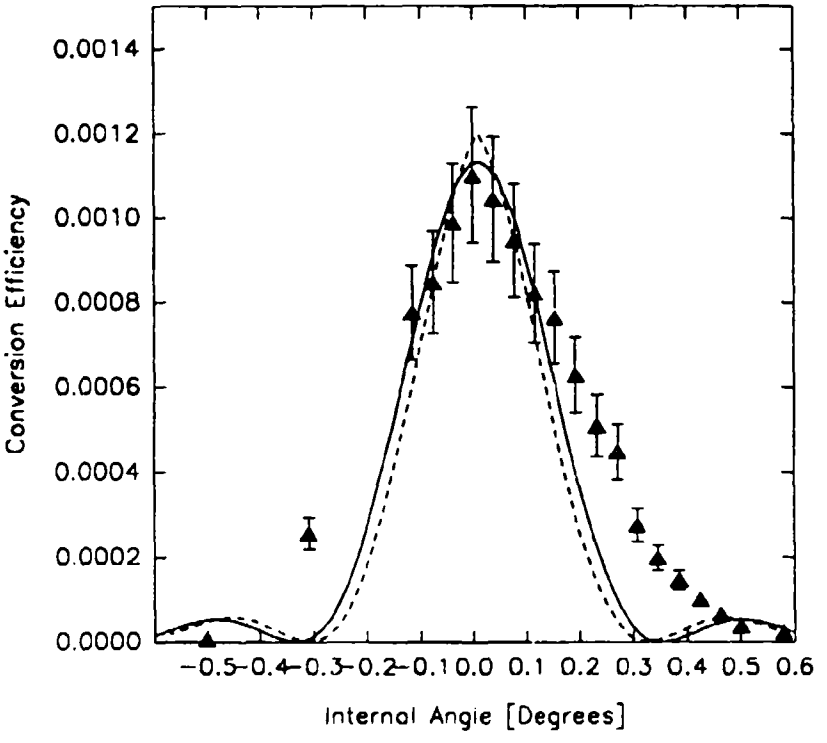

Figure 37. Efficiency as a function of the internal angle of propagation, θ, using power measurements of the non-focussed second harmonic generation in $AgGaSe_2$. The crystal was placed 15.2 cm from the laser, with an average input power of 7.0 W. The data points are shown as the filled triangles with the calculated error bars. (———) Fit to the data using Eq.(4.1) modified by a factor of 0.34. (---------) Fit to data using Eq.(4.38) modified by a factor of 0.22.

mate is reasonably close to the peak value of 0.11% for the same conditions considered in the power measurements. This calculation proves to be very tedious and is summarized in Figures 38 and 39.

In Figure 38, the radially dependent conversion efficiency is the exact solution calculated given the intensity level at the specified values of the radius, r, in Eq.(4.56). The weighting factor is the integral expression of this equation. The integral of the area under the curve in Figure 39 is the total efficiency.

The temporal waveforms of the fundamental and second harmonic pulses at the angle of

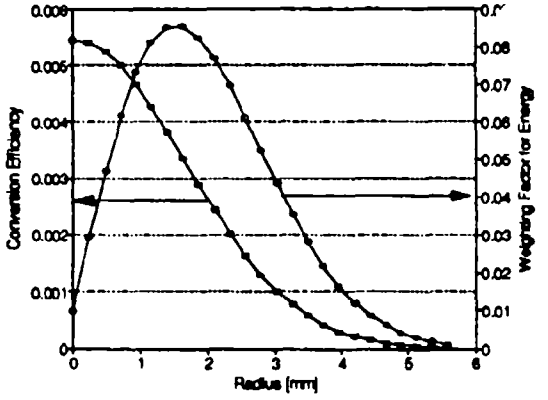

Figure 38. Plot of the components of Eq.(4.56) as a function of the radius.

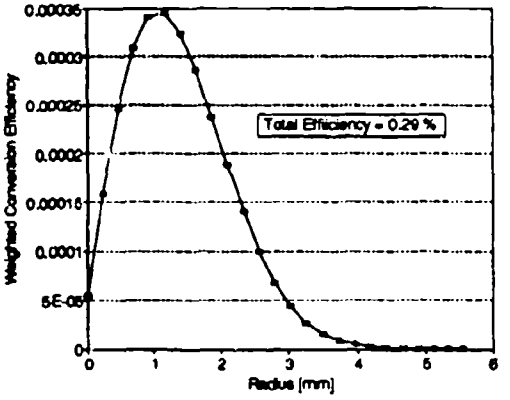

Figure 39. Result of multiplying the components point by point.

peak efficiency at the same distance as the measurements above were recorded in the three pulse repetition formats available from the source. Each is shown in Figures 40, 41 and 42 for the 30, 50 and 100 kHz pulse repetition formats respectively. In all the cases, the second harmonic pulse increases efficiency with the instantaneous power of the pulse to peak at the temporal peak of the fundamental.

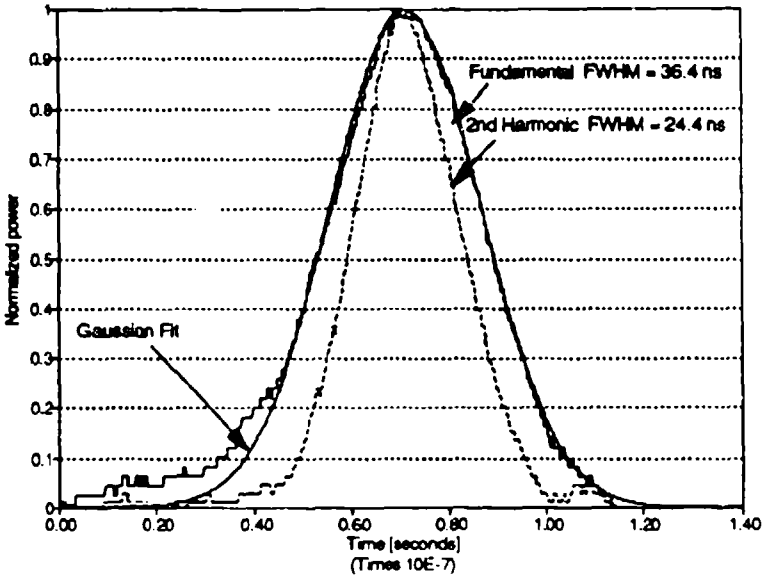

Figure 40. Normalized amplitude of the fundamental and second harmonic pulses as a function of time for the 30 kHz pulse repetition frequency. Average input power = 7.4 W. The Gaussian fit to the fundamental pulse has a characteristic time of 21.86 ns.

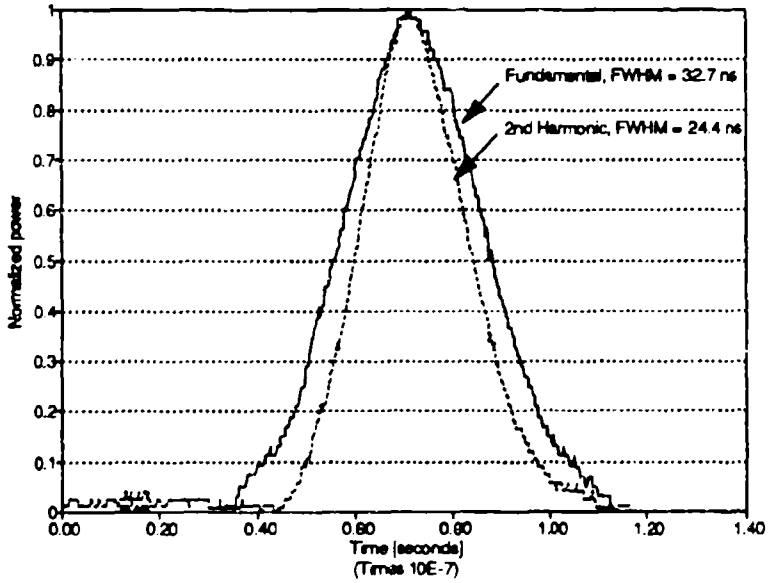

Figure 41. Normalized amplitude of the fundamental and second harmonic pulses as a function of time for the 50 kHz pulse repetition frequency. Average input power = 11.6 W.

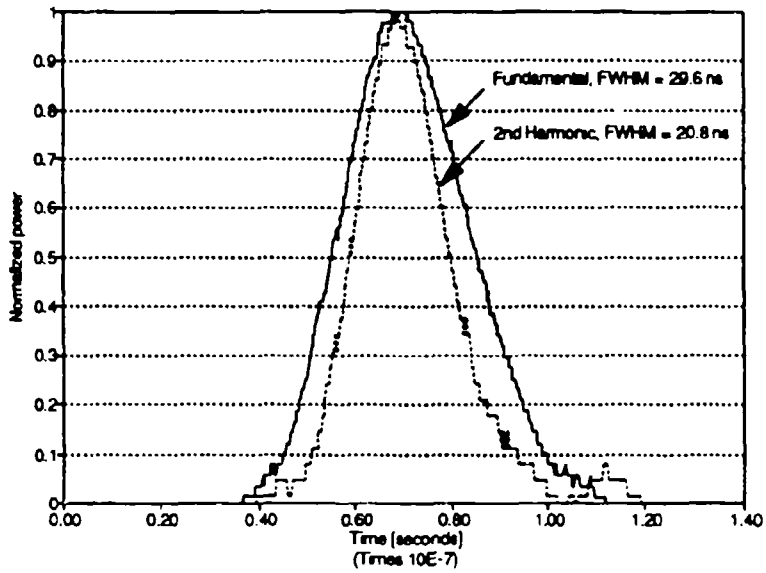

Figure 42. Normalized amplitude of the fundamental and second harmonic pulses as a function of time for the 100 kHz pulse repetition frequency. Average input power = 17.0 W.

The spatial profiles of the fundamental and second harmonic beams recorded using the pyroelectric infrared vidicon camera are shown in Figures 43 and 44. Since the conversion efficiency is so low, there is little unusual structure in either of the surfaces. At higher efficiencies, we may would expect to see asymmetric depletion of the fundamental as the two beams deviate from one another c ver the length of the crystal.

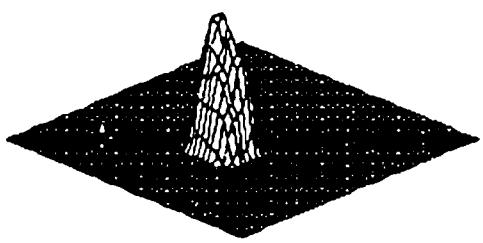

Figure 43. Surface plot of the intensity profile of the fundamental after passing through the $AgGaSe_2$ crystal.

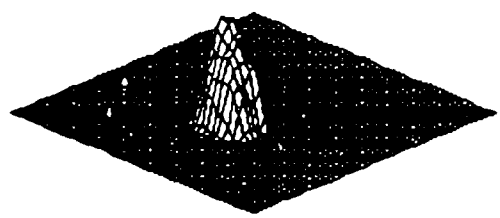

Figure 44. Surface plot of the intensity profile of the second harmonic produced by $AgGaSe_2$ crystal.

Focussed Second Harmonic Generation with $AgGaSe_2$

Using the 12.5 cm focal length lens, the initial focussed efficiency measurements were taken at a distance which would avoid any chance of early damage to the crystal. Second harmonic energy produced over the course of a series of 1 second exposures was recorded as a function of the angle of propagation θ in the media and the results are shown in Figure 45.

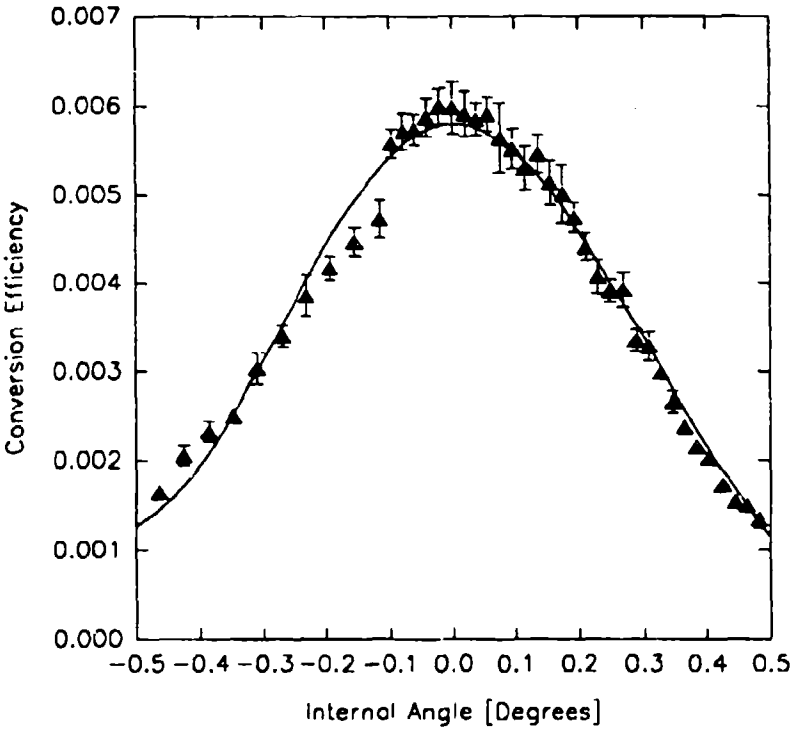

Figure 45. Efficiency as a function of the internal angle θ for the focussed case, f = 12.5 cm, distance from the laser to the lens, z_2 = 50 cm, distance from the lens to the crystal face, z_3 = 11.1 cm and a nominal average power of 6.0 W. The solid line is an eight order polynomial fit.

In these measurements, versus θ, for the non-focussed and focussed cases, the angular acceptance can be extracted as the internal angular bandwidth over which the efficiency drops to a value of one half the peak. For the three methods of measurement, the results are shown in Table 6.

Table 5.

Phase matched angles and angular acceptance results for the three measurement techniques at the phasematched angle, $\theta = 55.02^0$.

Measurement Technique	Angular Acceptance	Divergence of the input beam
Non-focussed energy measurements	$0.292^0 \pm 0.03$	1.85 mrad
Non-focussed power measurements	$0.333^0 \pm 0.04$	1.85 mrad
Focussed energy measurements, $f = 12.5$ cm	$0.656^0 \pm 0.03$	10.39 mrad

With the sensitivity of this axis characterized, we were able to begin studies of the dependence of the conversion efficiency on the intensity of the focussed beam. This was accomplished by fixing the angular position in the phase-matched direction and translating the crystal along the axis z_3 with respect to the focal point. This was accomplished for several combinations of average power levels and the two lenses used in the focussed experiments.

For the 12.5 cm focal length lens, the efficiency as a function of distance behind the lens is shown in Figures 46, 47 and 48 for with an average power at the crystal of 0.30 W, 2.22 W and 5.45 W respectively. The peak and average powers were attenuated using various filters. Note the plot of the peak intensity at the center of the crystal shown against the secondary y-axis in each of the figures. It is clear that in this arrangement, the peak efficiency occurs when the focus lies at the center of the crystal.

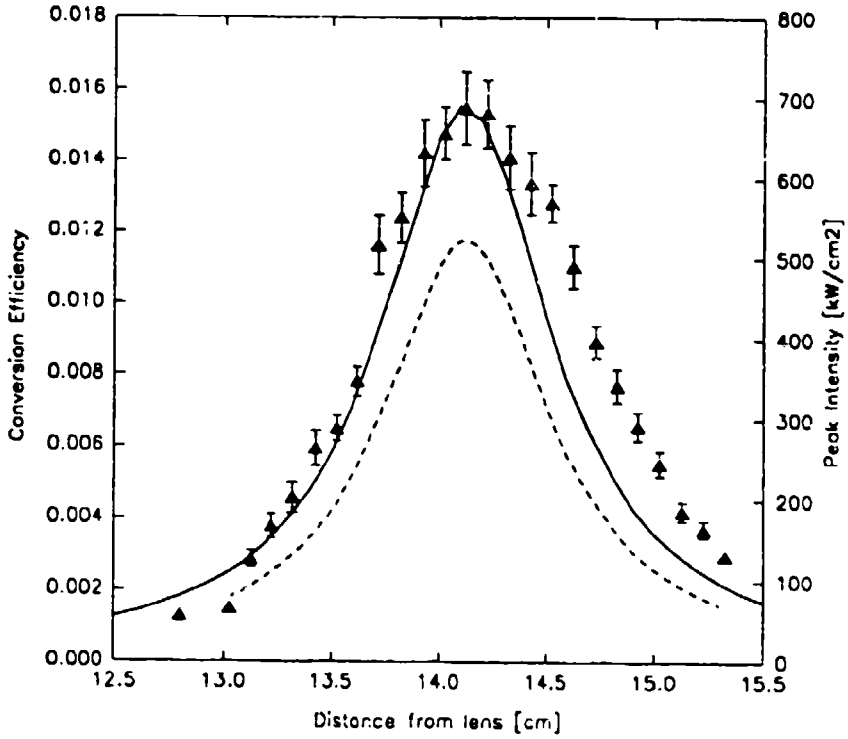

Figure 46. Efficiency as a function of the distance from the focussing lens, z_3, f = 12.5 cm, at the phase matched angle, θ_m. Distance from the laser to the lens, z_2 = 50 cm, with a nominal average power of 0.30 W. The data points are shown as the filled triangles with the calculated error bars. (———) Fit to the data using Eq.(4.38) modified by a factor of 0.385. (---------) Calculated peak intensity at the center of the crystal used in theoretical calculation of the efficiency.

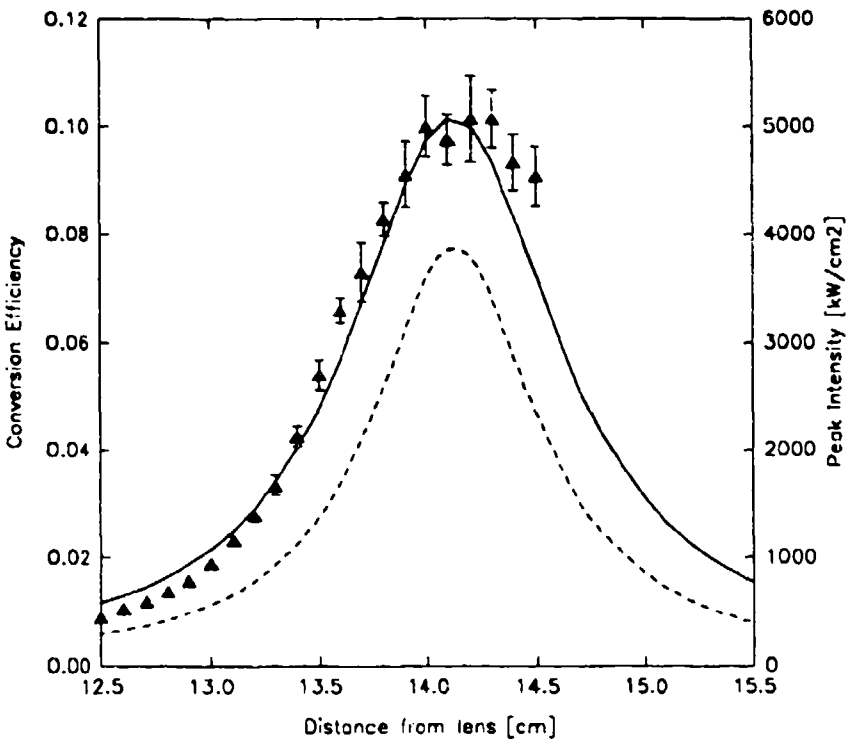

Figure 47. Efficiency as a function of the distance from the focussing lens, z_3, f = 12.5 cm, at the phase matched angle, θ_m. Distance from the laser to the lens, z_2 = 50 cm, with a nominal average power of 2.22 W. The data points are shown as the filled triangles with the calculated error bars. (———) Fit to the data using Eq.(4.38) modified by a factor of 0.5. (---------) Calculated peak intensity at the center of the crystal used in theoretical calculation of the efficiency.

Restricting our attention to the case of highest efficiencies, the calculated values can be improved by incorporating the radially dependent intensity profile, Eqs.(4.55-56), with Eq.(4.38) as shown in Figures 38 and 37. Using the far field half angle divergence of the beam inside the crystal in the dephasing term, $\delta = 1.363\text{rad}^2$ (also note Eq.(4.48)), we can calculate the efficiency as a function of the distance between the crystal and the lens, z_3, to yield an excellent approximation to this efficiency (see Figure 49).

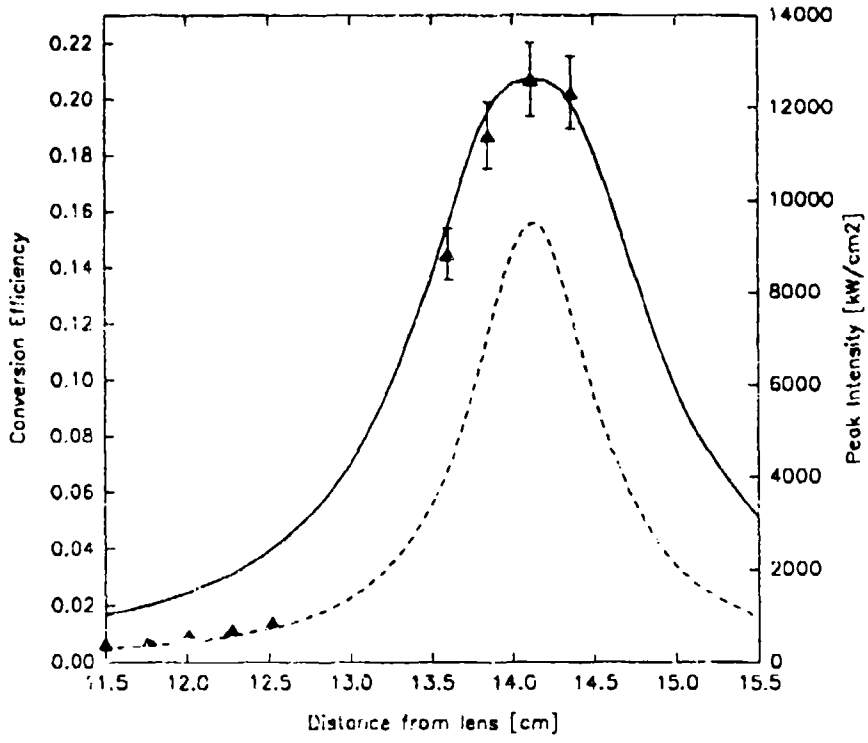

Figure 48. Efficiency as a function of the distance from the focussing lens, z_3, f = 12.5 cm, at the phase matched angle, θ_m. Distance from the laser to the lens, z_2 = 50 cm, with a nominal average power of 5.45 W. The data points are shown as the filled triangles with the calculated error bars. (———) Fit to the data using Eq.(4.38) modified by a factor of 0.72. (---------) Calculated peak intensity at the center of the crystal used in theoretical calculation of the efficiency.

The 6.05 cm focal length Ge positive meniscus lens had the tightest focus of the elements used in these measurements. In its use, we must be particularly careful about the position of the focus and the corresponding intensity levels to avoid damage to the crystal. The minimum spot size of 55.61μm is much smaller than optimum, as described by Eq.(4.63), and we expect relatively poor efficiency. The results for an average input power of 0.19 W and 0.40 W are shown in Figures 50 and 51 respectively. The short focal length leads to a large divergence and the beam is actually clipped by the 10.6 μm attenuator prior to striking the detector at Position I in Figure 34. This aperaturing is taken into account when calculating the power in the

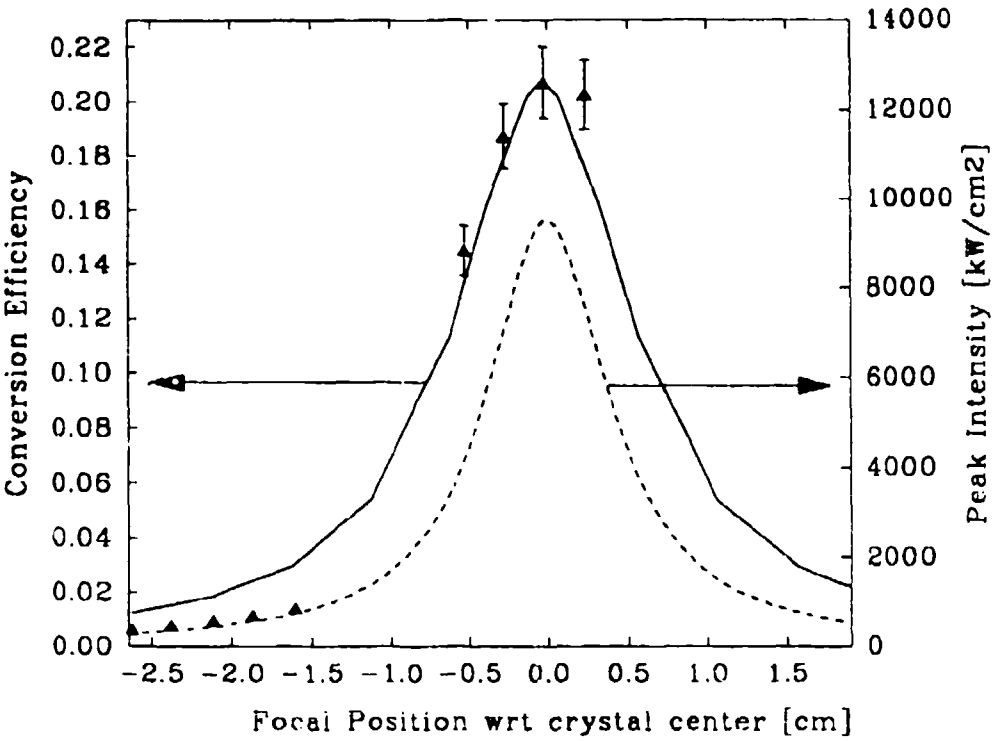

Figure 49. Measured and calculated conversion efficiency (Eq.(4.56)) as a function of the position of the focussed beam waist with respect to the center of the crystal. f = 12.5 cm, at the phase matched angle, θ_m. Distance from the laser to the lens, z_2 = 50 cm, with a nominal average power of 5.45 W. (---------) Peak intensity at the center of the crystal (note relation to z_3 in Figure 48).

second harmonic as the crystal is moved in relation to the focus. Although the peak of the efficiencies still correspond to the focus at the center of the crystal, the values vary a great deal. This can mostly be attributed to changes in the output power of the laser over time.

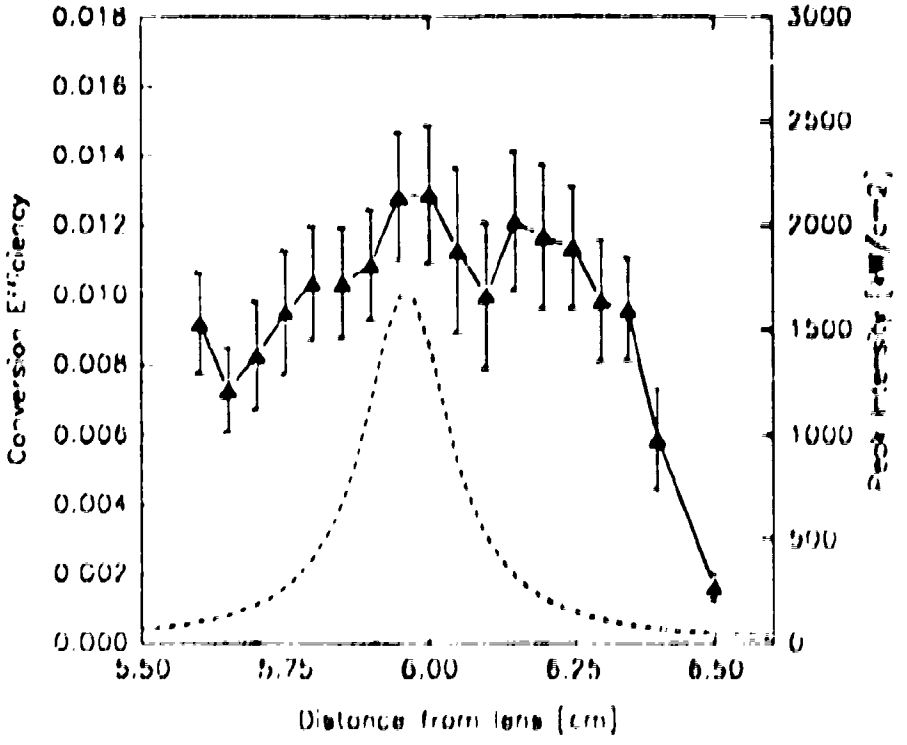

Figure 50. Measured conversion efficiency as a function of the distance from the focussing lens, z_f, f = 6.05 cm, at the phase matched angle, θ_m. Distance from the laser to the lens, z_l = 50 cm, with a nominal average power of 0.19 W. Error bars for each of the data points are included and the calculated peak intensity at the center of the crystal appears as the dashed line.

In the mathematical estimates of the efficiency, all of the input power at the fundamental frequency is assumed to be parallel to polarization required to excite the dipole oscillators at the frequency of the second harmonic. Deviations in the input polarization result in less power being applied to this solution. The power produced at the second harmonic frequency will fall off as the cos^2 of this angular deviation. We were able to observe this effect with the shorter focal length lens by rotating the crystal about its central axis (axis E in Figure 33). The results for relatively low input power levels in shown in Figure 52. Note the peak of this function does not lie parallel the vertical polarization axis (0°) and can be attributed to a slight deviation

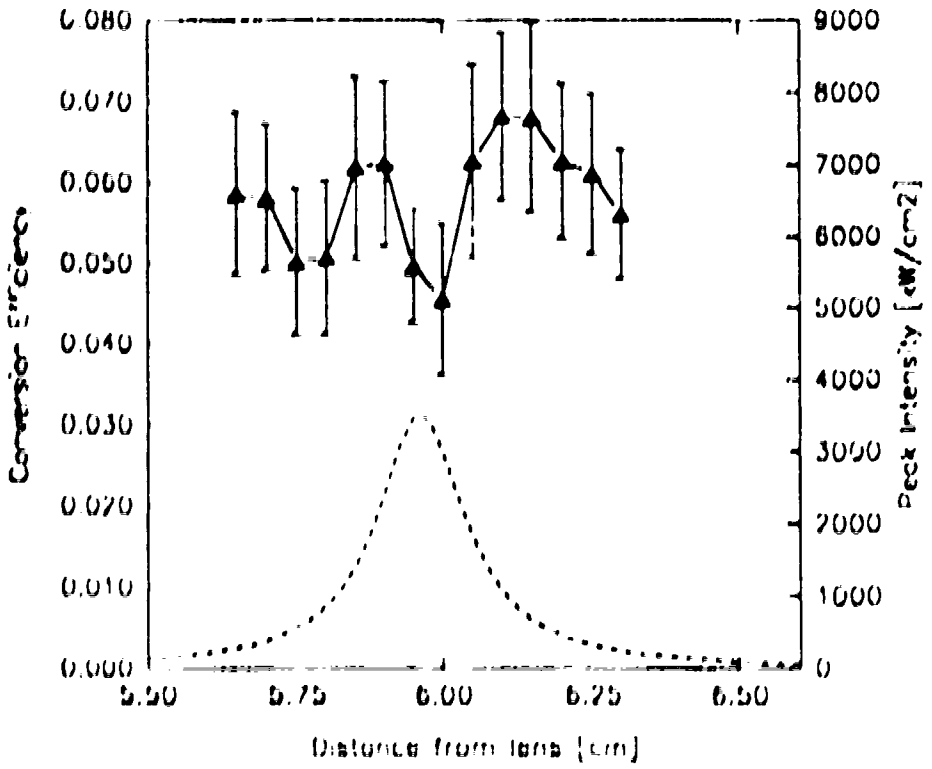

Figure 31. Measured conversion efficiency as a function of the distance from the focussing lens, z_2, $f = 6.05$ cm, at the phase matched angle, θ_m. Distance from the laser to the lens, $z_1 = 50$ cm, with a nominal average power of 0.40 W. Error bars for each of the data points are included and the calculated peak intensity at the center of the crystal appears as the dashed line. Note the average power from the laser was probably the main source of variability in these efficiencies.

of the output polarization of the laser from vertical at this point (see Figure 4). The drop off is quite a bit steeper than $\cos^2$, but due to the odd entry angles, accurate θ alignment was not always possible.

In several sets of the these measurements, particular concern was paid to keeping the peak and average powers well below known damage thresholds for the material. By incorporating a chopper into the experimental setup, as shown in Figure 34, the anticipated high average intensity levels could be reduced to safe levels. A 50% duty cycle chopper blade with 10 opens was used to chop the beam at frequencies from 50 to 1000 Hz. Chopping the beam provided a way

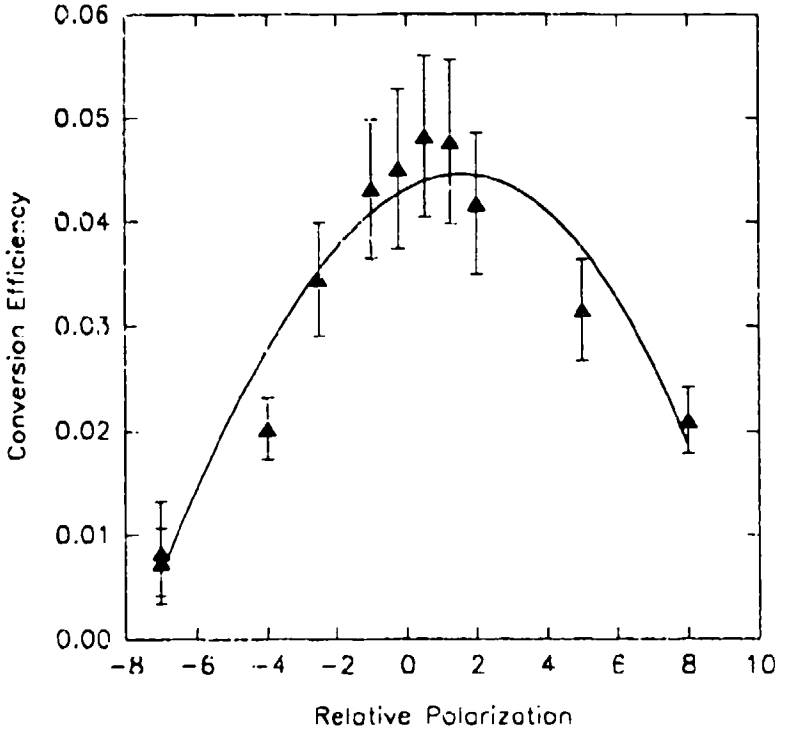

Figure 52. Measured and calculated conversion efficiency as a function of the deviation about axis E, f = 6.05 cm, at the phase matched angle, θ_m. Distance from the laser to the lens, z_2 = 50 cm, distance from the lens to the crystal, z_3 = 6.3 cm, with a nominal average power of 0.19 W. Error bars the measurements are shown for each of the data points.

to maintain the peak intensity values of the pulses, and therefore the peak conversion efficiencies, while reducing the thermal load (and average intensities).

An interesting trend was observed that was not accounted for by these predictions. There was a marked decrease in the observed conversion efficiency when the beam was chopped as opposed to allowed to run unhindered. The first set of measurements were taken as a function of z_3 for several chopping frequencies with the blade described above and is shown in Figure 53. The average power of the non-chopped beam was 3.95 W during this set of measurements

and we note the measurements at the distances further from the focal length become independent of the chopping frequency. The readings at the lower chopping frequencies were discontinued due to a lack of time.

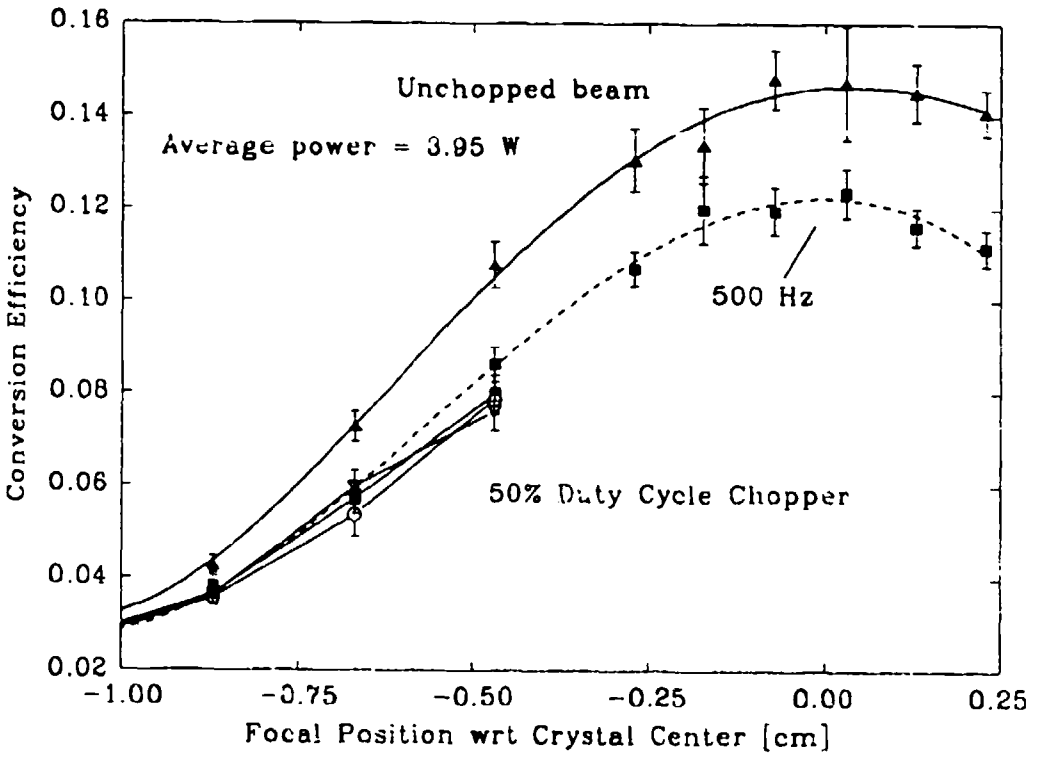

Figure 53. Measured and calculated conversion efficiency as a function of the distance from the focussing element, z_3, for several chopping frequencies. f = 12.5 cm, at the phase matched angle, θ_m, distance from the laser to the lens, z_2 = 50 cm, with a nominal average power of 3.95 W. Error bars for a typical measurement are shown for one of the data points.

Because of the slow variations in the output power of the laser as a function of time (due to cooling water temperature, power surges, etc.), a probe HeNe laser and photovoltaic detector were incorporated to measure the exposure time of the shutter mechanism directly. This allowed us to back out the average power in the beam when it struck the crystal and track this variation without incorporating errors in the mechanical shutter exposure time.

This also allowed us to investigate the effect of exposure duration on conversion efficiency

for the chopped and non-chopped beam. These results, for one chopping frequency are shown in Figure 54. The average power of the laser is shown as the series of unfilled symbols corresponding to the y-axis on the right side of Figure 54. The average power fluctuations are relatively minor. It is interesting to note the trend in the efficiency falls off with longer exposures. This can be expected since the induced thermal gradients will generally lead to greater dephasing of the fundamental beam over the length of the crystal.

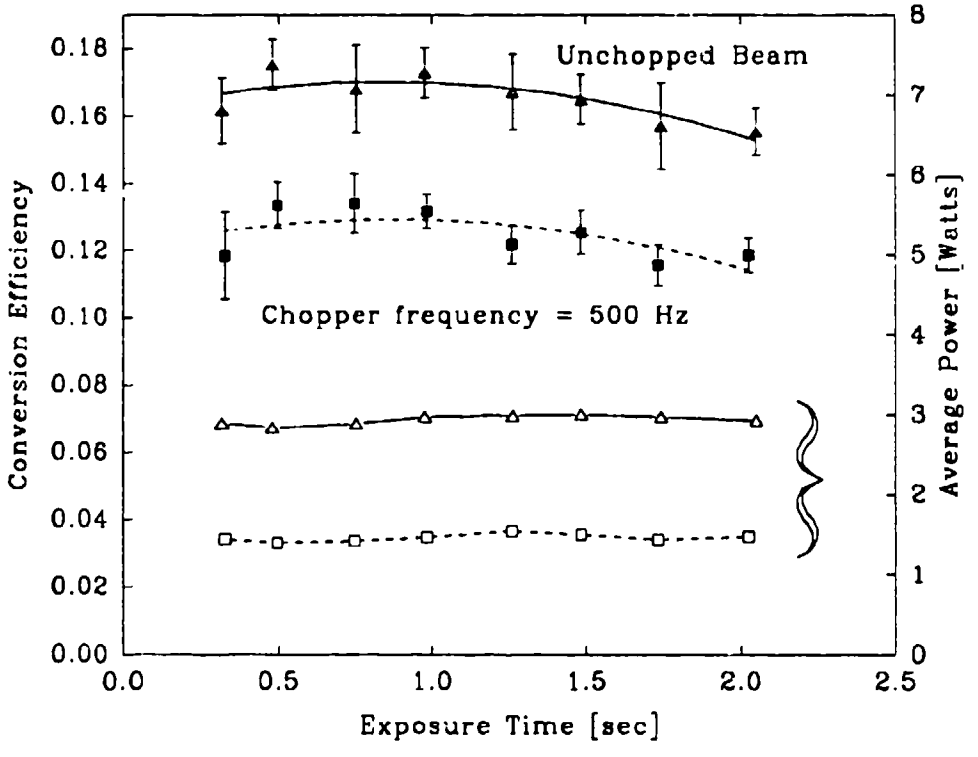

Figure 54. Measured and calculated conversion efficiency as a function of the exposure duration at a fixed distance from the focussing element, z_3, for 0 Hz (no chopping) and 500 Hz chopping frequencies. f = 12.5 cm, at the phase matched angle, θ_m, distance from the laser to the lens, z_2 = 50 cm, with a nominal average power of 3.0 W. Error bars for the measurements are shown for each of the data points. The hollow symbols of the same shape as the data points correspond to the average input power of the laser during those exposures.

The drop off near the shorter exposures is due to the limitations of the mechanical shutter reaction time, however, the difference between the chopped and non-chopped measurements is not as easily explained. The corrected average powers indicate that the peak intensities for each is approximately the same, but when chopped, the efficiency drops significantly. Thermal lensing may help to reduce the divergence of the beam inside the crystal to a limited degree in the non-chopped mode, leading to better overall conversion.

Focussed Second Harmonic Generation with $ZnGeP_2$

As an estimate of the second harmonic power we expected to observe using the configuration specified in Chapter V, we can use Eq.(4.56) where the effective nonlinear coefficient will be

$$d_{eff} = (111\text{pm/V})\sin(2 \cdot 85.16^0)\cos(2 \cdot 90^0) = 18.7\text{pm/V} \qquad (6.2)$$

Using the same configuration as in the previous experiments, where $z_2 = 65$cm and $z_3 = 13.6$cm, and an input power of approximately 2 Watts, the calculated efficiency is 1.4%. We noted in the comparison of the calculated values at the lower efficiencies with Eq.(4.56) were generally much higher than actually observed.

No second harmonic power was observed using $ZnGeP_2$ with either the calorimeters or the very sensitive HgCdTe detectors. This may be due to several sources. At these oblique angles of incidence, 15^0, the amount of energy coupled into the crystal through the uncoated surface is decreased by 25%, while the dephasing introduced at this angle was not considered in the estimates of the efficiency. d_{eff} is still relatively small at this angle, and the crystal is now critically phase matched which would lead us to reconsider the accuracy of the temperature dependent Sellmeier coefficients (Table 3).

Continued experimental work may achieve very low efficiencies at best if the crystal temperature is increased even further. The oven used in this experiment cannot achieve temperatures much above 250^0C.

Damage Studies with $AgGaSe_2$

Planned as the final stage of the series of experiments to characterize the $AgGaSe_2$ crystal, damage occurred at power levels below those anticipated from published values. The damage to the main crystal is summarized first followed by the results from the exposures of the witness samples.

Damage to the crystal occurred at three separate places on the crystal face after a series of exposures prior to the breakdown of the surface. Bulk damage was not observed on any of the damage points, and in fact, several data points in the previous analysis were taken in the unaffected areas after the surface had been marred. The first of the damage points was at the center of the crystal face and occurred after approximately seven exposures on the same order of magnitude as the published damage threshold of 19.7 kW/cm^2 for repetitively pulsed sources (12:10).

Figure 55 shows the entire face of the crystal and the effect of the anti-reflection coating flaking away near the damage point. Figure 55 is a close-up of the damage point itself.

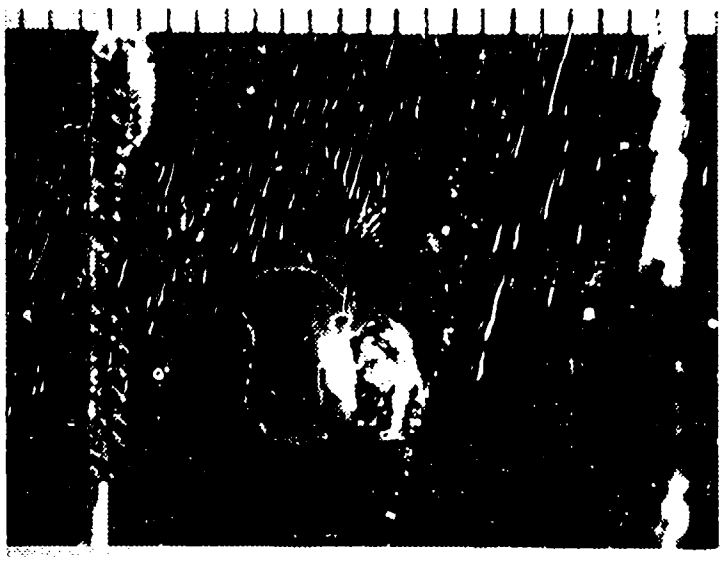

Figure 55. Damage to the face of the $AgGaSe_2$ crystal occurred at distance from the focussing element, z_3 = 14.05 cm, f = 12.5 cm, at θ_m, distance from the laser to the lens, z_2 = 50 cm, with a nominal average power of 5.45 W at a PRF of 30 KHz. The tick marks across the top of the photograph correspond to increments of 0.5 mm.

Figure 56. Damage to the face of the $AgGaSe_2$ crystal occurred at distance from the focussing element, z_3 = 14.05 cm, f = 12.5 cm, at θ_m, distance from the laser to the lens, z_2 = 50 cm, with a nominal average power of 5.45 W at a PRF of 30 KHz. The tick marks across the top of the photograph correspond to increments of 0.5 mm.

The results of these damage points are shown in Table 7 and include the peak and average powers at the damage point, the pulse repetition frequency, the spot size of the beam and an estimate of the radius of the burn spot.

Table 6.

Results of the damage points to the $AgGaSe_2$ crystal (Damage point 1 is shown in the Figures 55 and 56).

Damage Point	Average Intensity (kW/cm^2)	Peak Intensity (kW/cm^2)	PRF (kHz)	Spot size (μm)	Burn spot Radius (μm)
1 (Figures 55-56)	9.06	7794	30	138	379
2	4.59	1458	100	221	288
3	4.92	4240	30	155	252

The witness samples were mounted perpendicular the input beam, backed through the focus of the lens and subjected to a series of one second exposures. At the point of damage, the spot size and intensity levels were recorded for the coated and uncoated sides of the samples. The

results are summarized in Table 8. The damage points for the coated surfaces were restricted to the first surface and the results are shown in the upper portion of the table. The damage to the uncoated surfaces, however, reached through the depth of the witness samples to form a burn spot on the opposite side as well. It appears that the bulk damage limits were rarely met due to the low threshold values of the antireflection coatings.

Table 7.

Results of the damage studies with the $AgGaSe_2$ witness samples.

Damage Point	PRF (kHz)	Average Intensity (kW/cm^2)	Peak Intensity (MW/cm^2)	Spot size (μm)	Burn spot Radius (μm)
Antireflection coated surface	30	3.1 ± 0.3	2.7 ± 0.3	209 ± 21	304 ± 53
	50	4.6 ± 1.0	1.6 ± 0.3	193 ± 17	447 ± 18
	100	5.0 ± 1.1	1.6 ± 0.4	229 ± 33	661 ± 125
Uncoated surface	30	2.4 ± 0.7	2.1 ± 0.7	349 ± 30	607 ± 30
	50	10.8 ± 9.6	3.7 ± 3.4	228 ± 99	571 ± 67
	100	10.8 ± 1.3	3.4 ± 0.4	153 ± 10	571 ± 30
Opposing coated surface	30	2.4 ± 0.7	2.0 ± 0.5	315 ± 30	178 ± 30
	50	7.7 ± 6.1	2.7 ± 2.1	208 ± 83	154 ± 39
	100	13.3 ± 1.8	4.2 ± 0.6	124 ± 9	125 ± 18

An interesting trend in the size of the damage points to the coated surfaces is shown in Figure 57. The average damage threshold of the coated surface was 4.85 ± 1.81 kW/cm^2 (average intensity). In Figure 57, the ratio of the measured to the calculated spot size gives a rough measure of the level above the damage threshold was achieved during that exposure. The minimum threshold for damage is approximately 2.5 kW/cm^2. The damage threshold for the bulk can be inferred from the three highest intensity levels achieved during these exposures to be 16 ± 8 kW/cm^2 which is within the error bounds of the previously published levels.

The surface of the crystal has a threshold for damage which may vary a function of the fatigue of the surface induced by several exposures over time. This was observed in the varia-

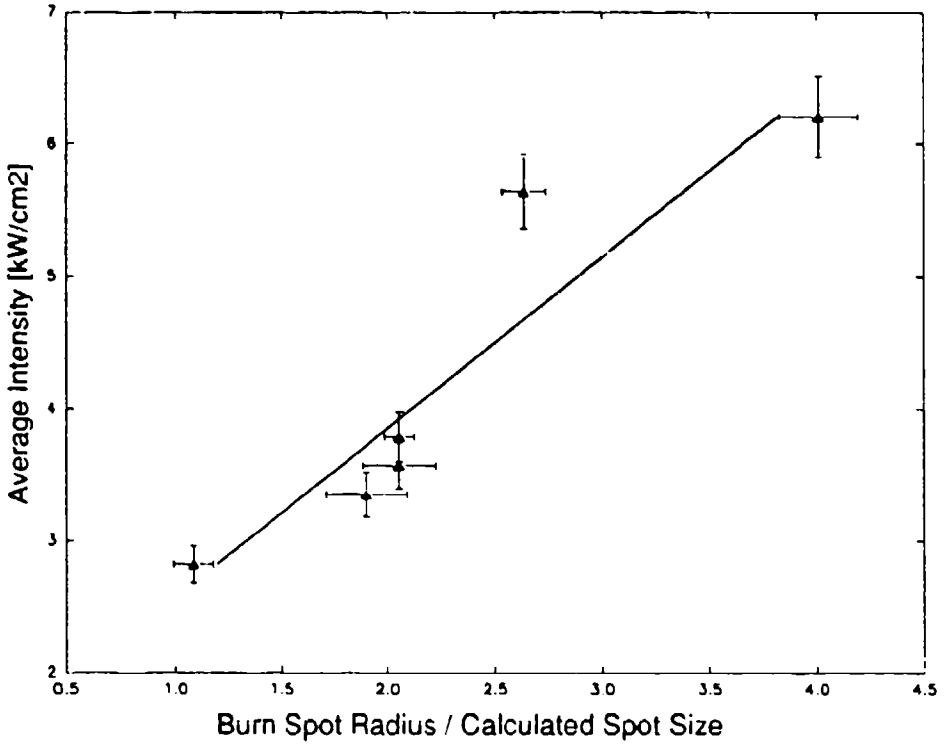

Figure 57. Average intensity levels for damage versus the ratio of the measured burn radius to the calculated spot sizes at the face of the crystal. This gives a rough measure of minimum levels for damage to the antireflection coated surface.

tion of the damage points to the main crystal. The peak intensity levels during the exposures of the witness samples averaged to a value of 2.0 ± 0.5 MW/cm^2 which is well below the published limits and it is unlikely that the peak intensity was mechanism for damage.

VII. Summary

The results of this study showed that high-average power second harmonic generation using $AgGaSe_2$ provides an efficient source of mid-infrared radiation at 5.3 μm. The work with $ZnGeP_2$ revealed that this material may be more appropriate for other applications such as OPO or SHG at shorter fundamental wavelengths. The TEM_{00} output mode of the CO_2 laser source at a pulse repetition frequency of 30 kHz (Gaussian temporal profile with $FWHM$ = 36.4 ns) was used in all of the measurements.

The absorptivity, $\alpha = 0.027 cm^{-1}$, of the $AgGaSe_2$ crystal was very low compared to those used in previous studies, (11:786) and (12:1). Measurements were made using a low power CW beam 10.6 μm. The lead and thorium fluoride based $\lambda/4$ anti-reflection coatings reduced surface losses to less than 0.5% at both the fundamental and second harmonic. Therefore, all efficiency measurements are given as external values.

The non-focussed efficiency measurements near the output port of the laser were conducted using two different methods. The first involved measurement of the energy produced at the second harmonic during 0.5 second exposures of the crystal. The far-field divergence half-angle of the beam inside the crystal, $\delta\theta = 1.85$mrad, with an average input power of 9.53 watts and $w = 2.35$mm at the face of the crystal, yielded a peak efficiency of 0.12%. The phase matched angle, $\theta_m = 55.14^0$, and angular acceptance, $\Delta\theta = 0.292^0$, compared very well with the values, $\theta_m = 55.02^0$ and $\Delta\theta = 0.300^0$, calculated using the Sellmeier coefficients (Table 3).

The crystal was provided from the manufacturer cut such that $\theta = 57.17^0$. Since $\theta_m \cong 55^0$, the fundamental was incident on the crystal face at 5.25^0 with respect to the normal direction. The theoretical estimates of the conversion efficiency using Eq.(4.1) and Eq.(4.38) were on the same order of magnitude as the measured values. The most exhaustive computation, Eq.(4.56), incorporating the radially dependent intensity profile of the Gaussian beam yielded a peak efficiency estimate of 0.29% which is in fair agreement at these very low values. Some of the deviation may be attributed to the oblique angle of incidence as noted above.

The second method of measuring the non-focussed efficiency involved recording the average power of the second harmonic produced during 30 second exposures of the crystal. With an average input power of 7.0 watts, all other factors the same as above, the efficiency at θ_m was 0.11%. Here we begin to notice the effects of heating on the crystal with an increase in the angular acceptance, $\Delta\theta = 0.333^0$. Theoretical estimates of the efficiency were comparable to those above.

Comparison of the temporal profiles of the fundamental and second harmonic revealed the $(P^{(\omega)})^2$ dependence of the power produced at the second harmonic. This lends support to approximation incorporated in the development of Eq.(4.57) which allows the CW theory for focussed SHG to be applied to the pulsed case (given a Gaussian shaped temporal profile).

The focussed SHG experiments were conducted using a 1" diameter *ZnSe* lens placed 50 cm from the output port of the laser such that $\delta\theta = 10.39$ mrad inside the crystal. Measurements of the angular acceptance with the focus of the beam far from the center of the crystal showed an increase with this divergent input beam to $\Delta\theta = 0.656^0$.

Efficiency was recorded using energy measurements where the exposure duration was generally limited to one second to avoid possible damage to the crystal or coatings. At θ_m, the distance between the focussing element and the crystal face was varied in order of track the dependence of the power produced at the second harmonic as a function of peak and average intensity incident. Plots of the results versus the position of the beam focus inside the crystal with respect to the center of the crystal showed that the peak occurred when the two coincided.

The highest efficiency recorded was 20.7% and occurred with an average input power of 5.45 watts with the focus at the center of the crystal. Note, this value is an average external SHG conversion efficiency. At this position, the average output power observed at 5.3 μm was 1.13 watts. External efficiencies as high as 18.7% have been previously reported for SHG of CO_2 output with an antireflection coated samples of $AgGaSe_2$ (12:1). This work represents a 2% increase in the absolute efficiency and a 10% increase relative to the published values. A

longer crystal length, lower absorptivity and larger focussed spot size, $w_b = 125$ μm, were all contributing factors to this improvement.

The theoretical estimates of the efficiency using Eq.(4.56) yielded excellent agreement with the measured values as well as the shaped of function produced when moving the position of the focus. Estimates using the numerically derived approximation (Pascal program in Appendix B) agreed with the peak of the tuning curves as well.

An unusual drop on in energy produced at the second harmonic was observed when a 50% duty cycle chopper was placed in path of the fundamental. The purpose of the chopper was to reduce the average intensity of the beam on the crystal while maintaining the peak intensity values of the pulses. Since conversion efficiency is solely a function of the instantaneous power, it should not have been effected by the chopper (or a drop in average power). However, given an average input power of 3.0 watts, with the focus at the center of the crystal, a 15% drop in the efficiency was observed when the chopper was in place (operating at 500 Hz). Further studies are proposed to determine the cause of this decrease.

Damage studies revealed that the antireflection coatings placed on the crystal significantly lowered the thresholds for catastrophic breakdown of the surface. The damage threshold for average intensity was approximately $2.5 kW/cm^2$ and that for the peak intensity was 2.0 MW/cm^2. These are much lower than previously reported values for the uncoated (11:788) and coated crystal (12:5).

VIII. Suggestions and Recommendations

In the continuation of this work with $AgGaSe_2$, better overall efficiencies may be achieved by using higher peak intensities in conjunction with a larger focussed spot sizes. This will serve to increase the overall output power and avoid the damage thresholds of the material. The crystal must first be recoated if the same sample is to be used in these studies. Developing antireflection coatings which do not lower the damage thresholds for the material is of primary concern. As noted in the short series of studies above, the bulk threshold for damage was rarely encountered due to the weakness of the coating.

The computational effort should be continued to complete the codes required numerically integrate the indefinite integral shown in Eq.(4.57). It should be robust enough to work over all limits of the integration encountered for various crystal lengths and orientations. This would provide a very useful tool in determining the optimum experimental arrangements for focussed second harmonic generation in a variety of crystals.

Of particular interest are the transient heating effects on the conversion efficiencies as noted with the introduction of the chopper in the Figures 53 and 54. This unexpected drop in the second harmonic output at lower average powers may lend clues to the problems of scaling these devices to higher levels.

The work with $ZnGeP_2$ for doubling of 10.6μm radiation would appear to be of interest to the research community only. The attraction of a non-critically phase matched material is countered by very poor performance (low d_{eff}) at these wavelengths. For practical purposes it is much better suited for optical parametric amplification at shorter wavelengths in the mid to far infrared spectrum.

The use of $AgGaSe_2$ as a doubling material for CO_2 lasers is a promising candidate for an efficient laser source in the 5 μm range. With optimum conversion efficiencies in excess of 20% and routine efficiencies above 10%, the material possesses the qualities of hardness, resistance to humidity and damage necessary for use in several applications.

Appendix A: Anisotropic Materials

In an anisotropic medium, we can characterize the speed of propagation of different frequencies and polarizations of light as the solutions to the Fresnel equations in the medium. In developing these solutions, the relevant aspects of crystal symmetry and the theory of anisotropic crystals are presented below.

Crystal Symmetry

The notation of crystal symmetry is often referred to in classifying various nonlinear material and a review is useful. A crystalline solid is composed of an orderly array of identical building blocks. The requirement that the structure be repetitive restricts the shape of basic units to those which can fill a three dimensional space without leaving gaps. There are seven basic systems which meet this requirement and are described by a set of three characteristic lengths and respective angles (Note Figure 58).

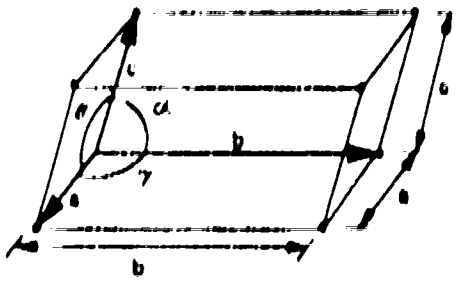

Figure . 3. Notation for angles and dimensions within a unit cell (18.5).

In the system of the crystallographic axes (a, b and c), directions and planes may be described in terms of the number basic unit lengths to travel in each of the three (not necessar

Table 8. The Seven Crystal Systems

System	Characteristic Symmetry Element	Unit Cell Characteristic	Crystal Point Group
Triclinic	None	$a \neq b \neq c$ $\alpha \neq \beta \neq \gamma \neq 90°$	1, $\bar{1}$
Monoclinic	One 2-fold rotation axis	$a \neq b \neq c$ $\alpha = \beta = 90° \neq \gamma$	2, m, 2/m
Orthorhombic	Three mutually perpendicular 2-fold rotation axes	$a \neq b \neq c$ $\alpha = \beta = \gamma = 90°$	222, mm2, mmm
Tetragonal	One 4 fold rotation axis or a 4 fold rotation-inversion axis	$a = b \neq c$ $\alpha = \beta = \gamma = 90°$	4, $\bar{4}$, 4/m, 422, 4mm, $\bar{4}$2m, 4/mmm
Cubic	Four 3 fold rotation axes (diagonals)	$a = b = c$ $\alpha = \beta = \gamma = 90°$	23, m3, 432, $\bar{4}$3m, m3m
Hexagonal	One 6 fold rotation axis	$a = b \neq c$ $\alpha = \beta = 90°$ $\gamma = 120°$	6, $\bar{6}$, 6/m, 622, 6mm, $\bar{6}$m2, 6/mmm
Trigonal (Rhombohedral)	One 3-fold rotation axis	$a = b = c$ $\alpha = \beta = \gamma \neq 90°$ $\alpha = \beta = \gamma \neq 120°$	3, $\bar{3}$, 32, 3m, $\bar{3}$m

Adapted from McKelvey (18:5) and Wood (21:55)

lly orthogonal) directions and the reciprocal of these values are referred to as the Miller indices. An example of a direction in Miller indices would be [112]. We take the reciprocal of this set, $\frac{1}{1},\frac{1}{1},\frac{1}{2}$ ➡ 2, 2, 1 , and this would describe a vector mapped from the origin of the system to a point two basic units along axis a, two along axis b and one along axis c. Simi-

larly, the description of the plane (112) would intersect the respective axes at each of these unit distances and if the system were cubic, would lie perpendicular to the direction [112]. Note Figure 59 where this direction and plane are described for a system with a cubic structure.

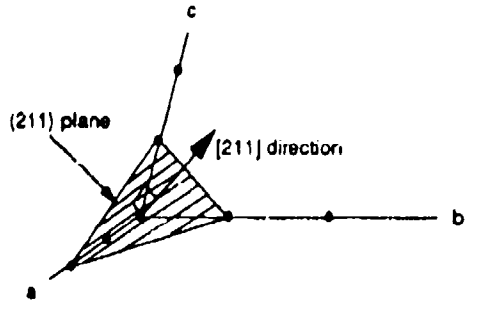

Figure 59. Miller indices and planes.

Each of these basic units possesses certain elements of symmetry which include mirror planes, rotational axes and inversion axes (21:10). A mirror plane exists if the system can be divided along a direction that would allow one half to be reflected through a mirror to reproduce the other. A rotational axis is an axis around which the system may be rotated to reproduce a system identical to that with which one started. These are limited to 1, 2, 3, 4 and 6-fold axes (generally, recent evidence of 5-fould symmetry is still under investigation). An inversion axis (often referred to as an improper rotation axis) is present if the system may be rotated by $2\pi/n$ and then inverted through the center of symmetry (center of the basic system or reflected through the horizontal plane of the system) to reproduce the original system. The combination of these elements of symmetry and the seven basic units leads to the 32 crystallographic point groups.

In this study, both crystals have a tetragonal basis and fall into the $\bar{4}2m$ point group. These

possess three two-fold rotation axes, two diagonal reflection planes and two inversion axes.

We note that these axes are useful for describing physical distances within the crystal but will often lack general utility because they are not always a mutually orthogonal set which can cover all of three dimensional space within the crystal. For this reason, we refer to the polarizability of the material since it is a physical property which will lend itself to designating an appropriate coordinate system.

Principal Coordinate System

The induced polarization of an isotropic medium is always parallel to the direction of an applied electric field and is related to it by a constant factor, the susceptibility, χ, (23:69) and is a measure of the net displacement of the electrons in a material under the influence of an optical $\vec{E}$ field.

$$\vec{P} = \varepsilon_0 \chi \vec{E} \tag{A.1}$$

In isotropic materials, the crystallographic axes are a mutually exclusive set of orthogonal directions. In an anisotropic dielectric material (where we assume the conductivity and free charge to be zero), however, this is not the case. The displacement current, $\vec{D}$, may be expressed as

$$\vec{D} = \varepsilon_0 \vec{E} + \vec{P} \tag{A.2}$$

where the polarization will not be parallel to the electric field expect for certain cases.

The linear polarization will depend upon the direction and magnitude of the applied field and will be related by

$$\begin{aligned} P_x &= \varepsilon_0(\chi_{11}E_x + \chi_{12}E_y + \chi_{13}E_z) \\ P_y &= \varepsilon_0(\chi_{21}E_x + \chi_{22}E_y + \chi_{23}E_z) \\ P_z &= \varepsilon_0(\chi_{31}E_x + \chi_{32}E_y + \chi_{33}E_z) \end{aligned} \tag{A.3}$$

where P and E are complex field quantities and the electric susceptibility becomes a second order tensor, $\bar{\chi}$ (in tensor notation, χ_{ij}). From Eq.(A.2) and Eq.(A.3) above, we may define the relative dielectric tensor, $\bar{\varepsilon}_R$

$$\vec{D} = \varepsilon_0\vec{E} + \varepsilon_0\bar{\chi}\vec{E} = \varepsilon_0(1 + \bar{\chi})\vec{E} = \varepsilon_0\bar{\varepsilon}_R\vec{E} \tag{A.4}$$

The nine components make up $\bar{\varepsilon}_R$ are assumed to be real and the tensor is required by the conservation of energy to be Hermitian and therefore symmetric. This means that there will at most be six independent terms that make up the second order tensor.

$$\bar{\varepsilon}_R = \begin{pmatrix} \varepsilon_{11} & \varepsilon_{12} & \varepsilon_{13} \\ \varepsilon_{12} & \varepsilon_{22} & \varepsilon_{23} \\ \varepsilon_{13} & \varepsilon_{23} & \varepsilon_{33} \end{pmatrix} \tag{A.5}$$

Recall from matrix theory that if a given matrix, B, is real and symmetric, there exists an orthogonal matrix, A, such that

$$ABA^T = \begin{pmatrix} \lambda_1 & 0 & 0 \\ 0 & \lambda_2 & 0 \\ 0 & 0 & \lambda_3 \end{pmatrix} \tag{A.6}$$

which is a diagonal matrix and the λ_i's are the eigenvalues of matrix B and the row vectors of A are the orthogonal eigendirections of B.

Since the relative dielectric tensor is real and symmetric, a coordinate transformation may be found which allows the system to be described by three independent components. The reference coordinate system is established by chosing the axes parallel to these eigendirections, x, y and z, such that the off-axis components vanish. This axis system is called the principal coordinate system and is not necessarily parallel to the crystallographic axes. In the principal coordinate system the dielectric tensor appears as

$$\bar{\varepsilon}_R = \begin{pmatrix} \varepsilon_1 & 0 & 0 \\ 0 & \varepsilon_2 & 0 \\ 0 & 0 & \varepsilon_3 \end{pmatrix} = \begin{pmatrix} n_1^2 & 0 & 0 \\ 0 & n_2^2 & 0 \\ 0 & 0 & n_3^2 \end{pmatrix} \tag{A.7}$$

where the diagonal components are related to the indices of refraction of the material by $\varepsilon_i = n_i^2$.

With this, we are able to define the optic axes, although their significance will not be established until the analytic solution to the Fresnel equations is shown below. When $n_1 \neq n_2 \neq n_3$, the two optic axes lie in a plane containing two of the eigendirections and the crystal is biaxial. Similarly, when $n_1 = n_2 \neq n_3$, the optic axis is parallel to one of the eigendirections and the crystal is uniaxial. If $n_1 = n_2 = n_3$, the crystal is isotropic.

Waves in an Anisotropic Medium

Now that a description of the medium is available, it is possible to derive its effect on incident radiation by considering the solution to Maxwell's equations given here in their general form

$$\nabla \cdot \vec{D} = \rho \tag{A.8}$$

$$\nabla \times \vec{E} = \frac{-\partial \vec{B}}{\partial t} \tag{A.9}$$

$$\nabla \cdot \vec{B} = 0 \tag{A.10}$$

$$\nabla \times \vec{H} = \frac{\partial \vec{D}}{\partial t} + \vec{J} \tag{A.11}$$

where in a dielectric medium, $\rho = 0$, $\sigma = 0$ and $\mu = \mu_0$. We assume a monochromatic plane wave of frequency ω propagating in the anisotropic medium with an electric field

$$\vec{E} e^{[i(\omega t - \vec{k} \cdot \vec{r})]} \tag{A.12}$$

and a magnetic field

$$\vec{H} e^{[i(\omega t - \vec{k} \cdot \vec{r})]} \tag{A.13}$$

Here $\vec{k}$ is the propagation or wave vector, $\vec{k} = (\omega/c) n \hat{s}$, where n is the index of refraction to be solved for and $\hat{s}$ is the unit vector in the direction of propagation. Substituting these forms into Maxwell's equations for an anisotropic dielectric medium

$$\vec{k} \cdot \vec{D} = 0 \tag{A.14}$$

$$\vec{k} \times \vec{E} = \omega \mu_0 \vec{H} \tag{A.15}$$

$$\vec{k} \cdot \vec{B} = 0 \tag{A.16}$$

$$\vec{k} \times \vec{H} = -\omega \vec{D} \tag{A.17}$$

where the geometric relations between the various field quantities is shown in Figure 60. Note $\vec{S}$, the Poynting vector, is defined by $\vec{S} = \vec{E} \times \vec{H}$, and is the direction of energy propagation, not the unit propagation vector $\hat{s}$.

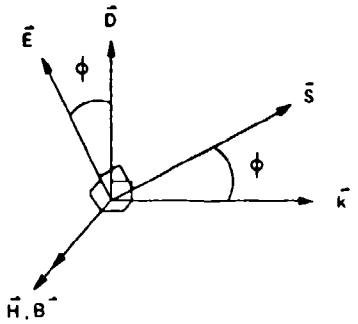

Figure 60. Representation of relations between the field vectors.

To obtain a relationship between the $\vec{E}$ and $\vec{D}$, we can eliminate $\vec{H}$ from Eq.(A.17) by substitution from Eq.(A.15) to obtain

$$\vec{k} \times \vec{k} \times \vec{E} = -\omega^2 \mu_0 \vec{D} \tag{A.18}$$

By the use of the vector identity $\vec{A} \times \vec{B} \times \vec{C} = \vec{B}(\vec{A} \cdot \vec{C}) - \vec{C}(\vec{A} \cdot \vec{B})$, and solving for $\vec{D}$

$$\vec{D} = \frac{1}{\omega^2 \mu_0}[|\vec{k}|^2 \vec{E} - \vec{k}(\vec{k} \cdot \vec{E})] \tag{A.19}$$

which is expressed in terms of the propagation vector explicitly. We can eliminate the magnitude of this component and express $\vec{D}$ in terms of the direction of propagation alone, where $\vec{k} = [k_1, \ k_2, \ k_3]$, by the relations

$$|\vec{k}| = \frac{\omega}{c} n \quad \text{and} \quad \frac{\vec{k}}{|\vec{k}|} = \hat{s} = [s_1, \ s_2, \ s_3] \tag{A.20}$$

By substitution into Eq.(A.19), the displacement vector can be expressed as

$$\vec{D} = \varepsilon_0 n^2[\vec{E} - \hat{s}(\hat{s} \cdot \vec{E})] \tag{A.21}$$

where $\hat{s}$ is the unit vector in the direction of propagation of the plane wave and n is the index of refraction or the wave property in the $\hat{s}$ direction.

At this point there are several approaches available for finding the solutions to this equation (23:77), the n's associated with the two possible orthogonal polarizations of the incident plane represented by $\vec{E}$. An analytic approach involving the simultaneous solution of three equations followed by the geometric representation is the most convenient of these methods.

By the linearity assumption, $\vec{D} = \varepsilon_0 \bar{\varepsilon}_R \vec{E}$, Eq.(A.21) may be readily expressed in terms of the material property $\bar{\varepsilon}_R$,

$$\varepsilon_0 \bar{\varepsilon}_R \vec{E} = \varepsilon_0 n^2[\vec{E} - \hat{s}(\hat{s} \cdot \vec{E})] \tag{A.22}$$

Assuming that we are working in the principal coordinate system where the dielectric tensor is a diagonal matrix, we are able to sum like vectorial components on both sides of this equation and represent it in the general form below where

$\delta_{ij} = 0$ when $i \neq j$ and $\delta_{ij} = 1$ when $i = j$,

$$\sum_j [\varepsilon_{ij} - n^2(\delta_{ij} - s_i s_j)] E_j = 0 \tag{A.23}$$

This represents a set of three homogeneous equations for the values in E_1, E_2, and E_3, one for each value of $i = 1$, 2, and 3. These may be written in full form, where the indices of refraction have been substituted for the eigenvalues ε_1, ε_2, and ε_3,

$$\begin{aligned}
[n_1^2 - n^2(1 - s_1^2)]E_1 + [n^2 s_1 s_2]E_2 + [n^2 s_1 s_3]E_3 &= 0 \\
[n^2 s_1 s_2]E_1 + [n_2^2 - n^2(1 - s_2^2)]E_2 + [n^2 s_2 s_3]E_3 &= 0 \\
[n^2 s_1 s_3]E_1 + [n^2 s_2 s_3]E_2 + [n_3^2 - n^2(1 - s_3^2)]E_3 &= 0
\end{aligned} \tag{A.24}$$

For the nontrivial solution to this set of homogeneous equations the determinant must equal zero. This is the Fresnel equation (note this must be in the principal coordinate system)

$$\begin{vmatrix} n_1^2 - n^2(1-s_1^2) & n^2 s_1 s_2 & n^2 s_1 s_3 \\ n^2 s_1 s_2 & n_2^2 - n^2(1-s_2^2) & n^2 s_2 s_3 \\ n^2 s_1 s_3 & n^2 s_2 s_3 & n_3^2 - n^2(1-s_3^2) \end{vmatrix} = 0 \qquad \text{(A.25)}$$

Given a particular direction of propagation with respect to the principal axes, the determinant will reduce to the general form $An^6 + Bn^4 + Cn^2 + D = 0$ where $A = 0$. Thus the solution is quadratic in n^2 and will yield at most two independent solutions, the eigenindices, n' and n''. Substitution of each of these solutions into Eqs.(2.24) will yield the eigenpolarization directions, E' and E'', which are the orthogonal linearly polarized eigenmodes for this direction of propagation. The crystal will break up the incident radiation into these two orthogonal polarizations with respect to the principal coordinate system. Each polarization will travel at a speed dictated by the respective index. The direction of propagation for both is considered to be the same, the direction of energy flow may be different.

Recall from Figure 60 and that Maxwell's equations imply that $\vec{D}$, $\vec{E}$ and $\vec{H}$ are related by

$$\vec{D} = -\frac{n}{c} \hat{s} \times \vec{H} \quad \text{and} \quad \vec{H} = \frac{n}{\mu c} \hat{s} \times \vec{E} \qquad \text{(A.26)}$$

According to these equations, $\vec{D}$ and $\vec{E}$ are both perpendicular to the direction of propagation $\hat{s}$ and the resulting direction of the energy flow, the Poynting vector, $\vec{E} \times \vec{H}$, is not, in general, parallel to $\hat{s}$ (23:75).

The Index Surface Representation

This last statement is easier to visualize once an understanding of the fact that the different polarizations of light within the media travel at different speeds has been developed. Consider that the index of refraction for each of the two eigenpolarizations can be represented as a three dimensional surface as depicted in Figure 61. Given the general case that $n_1 < n_2 < n_3$, these will be two separate index surfaces or ellipsoids which are the normalized $\vec{k}$ surfaces (recall Eq.(A.20)).

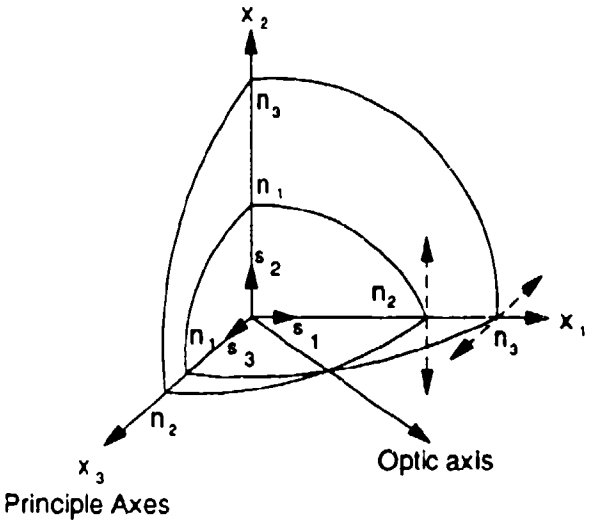

Figure 61. First quadrant of a biaxial index surfaces.

This may be interpreted best by considering the example polarizations shown as the dashed lines with the arrow heads. For both of these polarizations, the propagation is in the x_1 direction. The polarization parallel to the x_2 direction is subject to the n_2 index. Similarly, the orthogonal polarization (parallel to x_3) sees the n_3 index. This is the most general case of a biaxial crystal which has two optic axes as defined previously and shown in the diagram as that axis along which the two surfaces meet. For a biaxial crystal, there are only four such points which define the two axes.

In the course of this study, only uniaxial crystals were characterized, which is the case when $n_1 = n_2 \neq n_3$. The index surfaces then share a common boundary in the x_1-x_2 plane. In addition, the surfaces will be ellipsoids of revolution about the x_3 axis (the optic axis) and the surface defined by n_1 and n_2 will be a sphere. n_1 and n_2 are called the ordinary indices of refraction, n_o, and n_3 is called the extraordinary index, n_e.

It can be shown that the direction of energy propagation will be perpendicular to the index surface normal defined by the direction of the propagation through the media. In a uniaxial

material, Figure 62 depicts the two index surfaces present and the manner in which the orthogonally polarized components of the incident ray are broken up with respect to optic axis, x_3. Note that the angle of incidence with the crystal interface is normal.

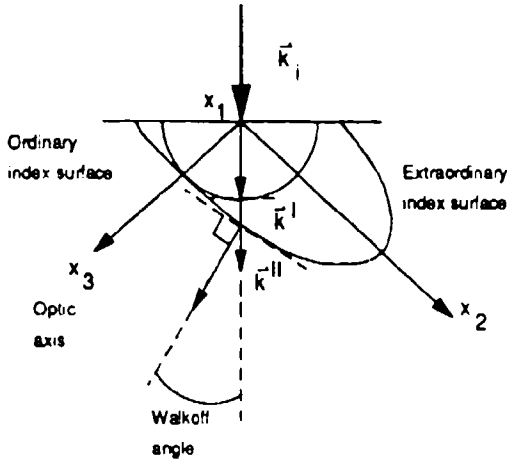

Figure 62. Propagation of two polarizations of an incident ray in a uniaxial material where the orientation of the index surfaces produces walkoff of the polarization in the plane of incidence.

The deviation of the energy flow of one of the polarizations with respect to the other is called walkoff, and is a result of the relations between the Poynting vector and propagation vector in an anisotropic media. Keep in mind that the normal boundary conditions, Snell's law, is still applicable, with the result that the two different eigenpolarizations will be deviated at different angles due to the two eigenindices as shown in Figure 63. This is an example of double refraction.

This review of the properties of anisotropic material properties provides the basis upon which the theory of nonlinear optics may be developed.

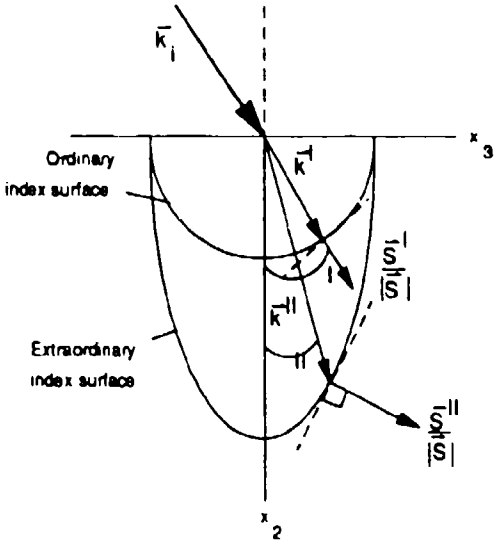

Figure 63. Propagation in a uniaxial crystal showing the effect of double-refraction at the interface and walkoff of the polarization in the plane of incidence (in the plane of the optic axis and the propagation vector).

Appendix B: Numerical Computation of SHG Efficiency

This program follows the development outlined in Chapter IV beginning with Eq.(4.57). The indefinite and definite integrals are evaluated using Romberg integration routines given the user inputs. The values calculated agree with those previously published (5:3600).

The program was written in Turbo Pascal, Version 5.5, for MS DOS based machines. The source code follows a brief summary of the required inputs and operation of the program in its present form. Reference Chapter IV for the definitions of the variables.

Upon compilation and execution of the source code, you have the option to specify the inputs for σ, β, κ, ξ and μ in a number of ways. When the program is initiated, the first column of characters on the lower left side of the screen, as shown in Figure 64, will accept one of four characters which determine how the values are calculated. These character responses are:

Character	*Description*
C	Calculate the value directly from inputs to the right (note definition of the variables). - The value to the right in immediately calculated and the cursor skips down to the next field.
I	Input the value directly (be wise in this choice due to the interplay between some of the variables). - The cursor moves to the right and requests the desired value.
O	Optimum value for the parameter (specified in Boyd (5:3602)). - Only useful for σ at this point.
R	Repeat the computation over a range of values for the specific variable (all others fixed). - Only use this option for one of the five variables at a time! - Must be aware of the interplay between variables in this case as well. - When you have completed all other inputs, the program will ask for the lower and upper limits of the variable range and the number of points to take between those limits. - After the series has run, the program asks for a filename under which to save the data and allows you to continue.

The input screen appears as shown in Figure 64. Upon completion of the computation, the value of σ, β, κ, ξ and μ and the conversion efficiency are displayed with the options to continue.

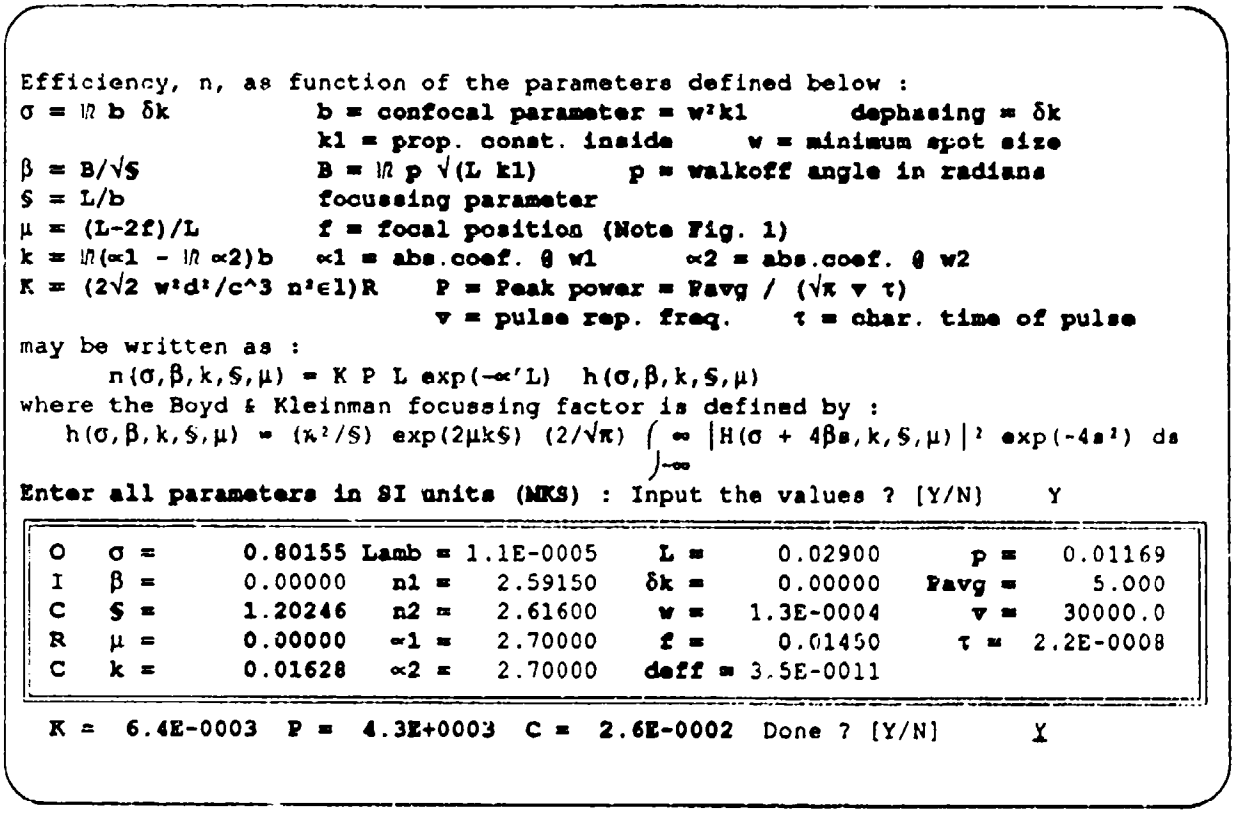

Figure 64. Appearance of the input screen to numerical calculate the conversion efficiency following the developments in Boyd (5:3600) and Eckardt (12:5).

```
PROGRAM BKF_Factor;      (*  Borland Turbo Pascal Version 5.5 *)

(* Program to numerically integrate the the double integral required to
estimate the SHG power as outlined in the article:

Boyd, G.D. and D.A. Kleinman, "Parametric Interaction of Focussed Gaussian
 Light Beams," Journal of Applied Physics, Vol. 39, No. 8: 3597-3639
 (July 1968).

This theory takes into account the focussed Gaussian nature of the beam,
walkoff, double refraction, position of the focus and absorption of the
fundamental and integrates the far field irradiance pattern to evaluate
the total second harmonic power generated.  The original program was
written in Pascal for the Macintosh by Mr. Robert Eckardt of Standford
University using a combination of Romberg and Gaussian quadrature routines.
It converges well for values of the double refraction parameter less than
two.  I hope to improve the model by adding other types of integration to
extend the range of convergence.
                                                                    *)
Uses PRINTER,CRT;

CONST   BEEP = 07;
        MAXNUMVAR = 24;

TYPE    STRING15 = STRING[15];
        STRING60 = STRING[60];
        SETOFCHAR = SET OF CHAR;
        PARAMETERS = ARRAY [1..MAXNUMVAR] OF REAL;

VAR     Continue : Char;

(* ------------------------------------------------------ *)

PROCEDURE RombH2(sigma,beta,xi,mu,kappa,s,lower,upper,tol:real;
                         q:integer; var h:real); FORWARD;

(* ------------------------------------------------------ *)

FUNCTION Getchar (X,Y:INTEGER;QUICK,DEFAULT:BOOLEAN;
          OKSET:SETOFCHAR; DF:CHAR; BLINE:STRING15) :CHAR;

(* Reads the response at the screen coordinates X,Y, QUICK toggles whether
it is a single character response or one followed by a CR, DEFAULT toggles
the default response DF, and the function checks to see if the input is
in the acceptable set of characters, SETOFCHAR.    *)

VAR     CH : CHAR;
        SHRT : STRING [2];
        GOOD : BOOLEAN;

BEGIN       (* GETCHAR *)
 REPEAT
  GOTOXY (X,Y); WRITE (BLINE); GOTOXY (X,Y);
  WRITE (DF); GOTOXY (X,Y);
  IF QUICK THEN BEGIN
    CH := ReadKey; GOTOXY (X,Y); WRITE (CH) END
   ELSE BEGIN
    READLN (SHRT);
    IF LENGTH (SHRT) < 1 THEN CH := '#'
     ELSE CH := SHRT[1];
```

```
    END;
   CH := UPCASE (CH);
   IF ((CH IN [CHR(13),'#']) AND (DFAULT = TRUE)) THEN BEGIN
     GOOD := TRUE; CH := DF  END
   ELSE GOOD := CH IN OKSET;
   IF NOT GOOD THEN WRITE (CHR(BEEP));
  UNTIL GOOD;
  GETCHAR := CH;
END;        (* GETCHAR *)

(* ..... *)

PROCEDURE GetNumber (X,Y:INTEGER; VAR DF:REAL);
VAR   HOLD : String[10];
     HOLDReal : real;
     GOOD : BOOLEAN;
     IChar : CHAR;
     Numbers, Arrows, Directs, Options : SETOFCHAR;
     Code : Integer;

BEGIN        (* GETNumber *)
  TextBackground(Cyan);
  TextColor(Blue);
  GOTOXY (X,Y); WRITE ('          ');
  GOTOXY (X,Y); WRITE (DF:10:5); GOTOXY (X,Y);
  READLN (HOLD);
  IF LENGTH(HOLD) <> 0 THEN BEGIN
   VAL(HOLD,HOLDReal,Code);
   IF Code = 0 THEN DF := HOLDReal;
  END;
  GOTOXY (X,Y); WRITE (DF:10:5); GOTOXY (X,Y);
  TextBackground(Black);
  TextColor(White);
END;        (* GETNumber *)

(* ..... *)

  FUNCTION fx2(x:real;q:integer;sigma,beta,xi,mu,kappa,s:real):real;

  (* Evaluates the real and imaginary parts of H^2 depending upon
  the toggle q.      *)

  VAR  Holdvar, H2,Rh,Ih,  sigmaP,R,I : real;
  BEGIN       (* fx2 *)
   sigmaP := sigma + 4 * beta * s;
   IF q = 2 THEN BEGIN
     R := exp(-kappa*x)/(1+x*x) * (x*sin(sigmaP*x)+cos(sigmaP*x));
     Holdvar := R   END
   ELSE BEGIN
     I := exp(-kappa*x)/(1+x*x) * (sin(sigmaP*x)-x*cos(sigmaP*x));
     Holdvar := I   END;
   fx2 := Holdvar;
  END;        (* fx2 *)
(* ..... *)

  FUNCTION fx1(x:real;q:integer;sigma,beta,xi,mu,kappa:real):real;
```

```
(* Function that returns the value of the function F and makes
two calls to the second Romberg integration routine which separately
evaluates the real an imaginary parts of H^2 *)
VAR  Holdvar, H2,Rh,Ih,  sigmaP,R,I : real;
BEGIN       (* fx1 *)
 (* Calls to the second Romberg integration routine RombH2 *)
 RombH2(sigma,beta,xi,mu,kappa,x,-xi*(1-mu),xi*(1+mu),1E-05,2,Rh);
 RombH2(sigma,beta,xi,mu,kappa,x,-xi*(1-mu),xi*(1+mu),1E-05,3,Ih);
 H2 := (Rh * Rh + Ih * Ih)/(4 * pi *pi);
 Holdvar := H2 * exp(-4 * x * x);
 fx1 := Holdvar;
END;       (* fx1 *)

(* ------------------------------------------------- *)
PROCEDURE ErrorMessage(q:integer);
BEGIN     (* ErrorMessage *)
 TextColor(Yellow);
 GOTOXY(42,16); Write('                    ');
 GOTOXY(42,16);
 CASE q OF
  1 : write ('Error: Loop for exp(-4s^2)');
  2 : write ('Error: REAL part of H^2');
  3 : write ('Error: IMAGINARY part of H^2');
 END;
 TextColor(White);
 Readln; Exit
END;      (* ErrorMessage *)

(* ------------------------------------------------- *)

PROCEDURE RombH2; (* (sigma,beta,xi,mu,kappa,lower,upper,tol:real;
                          q:integer; var h:real); *)

(* Romberg integration of H^2 components, declared above by a
FORWARD declaration. Both of the Romberg integration routines,
RombH2 and Romb are identical expect for the calls the inner
and outer functions. They were taken from:

 Alan R. Miller, Pascal Programs for Scientists and Engineers,
 Sybex Inc. (1981)

The only change is in the convergence criteria, as noted below.  *)

VAR   NX : array[1..16] of integer;
     T : array[1..136] of real;
     done, error : boolean;
     steps, NT, I, II, N, NN, L, NTRA, K, M, J : integer;
     delta_x, C, sum, fotom, X : real;

BEGIN        (* RombH2 *)
 done := false;   error := false;
 steps := 1;      NX[1] := 1;
 delta_x := (upper-lower)/steps;
 C:= (fx2(lower,q,sigma,beta,xi,mu,kappa,s)
    + fx2(upper,q,sigma,beta,xi,mu,kappa,s))*0.5;
 T[1] := delta_x*C;
 N := 1;         NN :=2;        sum := C;
```

```
  REPEAT
   N:= N+1;
   fotom := 4.0;
   NX[N]:= NN;
   steps := steps*2;
   L:= steps-1;
   delta_x:=(upper-lower)/steps;
   FOR II := 1 TO (L+1) div 2 DO BEGIN
    I := II * 2 - 1;
    X:= lower + I*delta_x;
    sum := sum+fx2(X,q,sigma,beta,xi,mu,kappa,s)  END;
   T[NN] := delta_x*sum;
   NTRA := NX[N-1];
   K:=N-1;
   FOR M:= 1 TO K DO BEGIN
    J:= NN + M;
    NT := NX[N-1]+M-1;
    T[J]:=(fotom*T[J-1]-T[NT])/(fotom-1.0);
    fotom := fotom*4.0  END;
   IF N>4 THEN BEGIN
    IF T[NN+1] <>0.0 THEN
     IF (abs(T[NTRA+1]-T[NN+1])<=abs(T[NN+1]*tol))
       OR (abs(T[NN-1]-T[J]) <= tol) THEN done := true
(* In the source for this code segment, the tolerance is checked according to
  OR (abs(T[NN-1]-T[J]) <= abs(T[J]*tol)) THEN done := true
instead of the above.  I found that the routines would not converge for
imaginary part of the H^2 because it is often very close to zero to
begin with.  Multiplying T[J] by tol  drives the value so close to
zero that we start seeing limits in the REAL variable type (16 bits).
The results with this converge test works great.  *)
      ELSE IF N > 15 THEN BEGIN
       done:=true;   error := true
      END;
    END; (*if*)
    NN := J+1;
   UNTIL done;
   h :=T[J];
   IF error THEN ErrorMessage(q);
 END;       (* RombH2 *)

(* ------------------------------------------------------------ *)

 PROCEDURE Romb (sigma,beta,xi,mu,kappa,lower,upper,tol:real;
                                q:integer; var h:real);
 VAR    NX : array[1..16] of integer;
      T : array[1..136] of real;
      done, error : boolean;
      steps, NT, I, II, N, NN, L, NTRA, K, M, J : integer;
      delta_x, C, sum, fotom, X : real;
```

```
BEGIN    (* Romb *)
 done := false;   error := false;
 steps := 1;      NX[1] := 1;
 delta_x := (upper-lower)/steps;
 C:= (fx1(lower,q,sigma,beta,xi,mu,kappa)
    + fx1(upper,q,sigma,beta,xi,mu,kappa))*0.5;
 T[1] := delta_x*C;
 N := 1;          NN :=2;         sum := C;
 REPEAT
  N:= N+1;
  fotom := 4.0;
  NX[N]:= NN;
  steps := steps*2;
  L:= steps-1;
  delta_x:=(upper-lower)/steps;
  FOR II := 1 TO (L+1) div 2 DO BEGIN
   I := II * 2 - 1;
   X:= lower + I*delta_x;
   sum := sum+fx1(X,q,sigma,beta,xi,mu,kappa)  END;
  T[NN] := delta_x*sum;
  NTRA := NX[N-1];
  K:=N-1;
  FOR M:= 1 TO K DO BEGIN
   J:= NN + M;
   NT := NX[N-1]+M-1;
   T[J]:=(fotom*T[J-1]-T[NT])/(fotom-1.0);
   fotom := fotom*4.0  END;
  IF N>4 THEN BEGIN
   IF T[NN+1] <>0.0 THEN
    IF (abs(T[NTRA+1]-T[NN+1])<=abs(T[NN+1]*tol))
      OR (abs(T[NN-1]-T[J]) <= abs(T[J]*tol)) THEN done := true
    ELSE IF N > 15 THEN BEGIN
     done:=true; error := true
    END;
  END; (*if*)
  NN := J+1;
 UNTIL done;
 h :=T[J];
 IF error THEN ErrorMessage(q);
END;     (* Romb *)
(* ------------------------------------------------------ *)
 PROCEDURE InputParms(VAR sigma:real; VAR beta:real; VAR xi:real;
              VAR mu:real; VAR kappa:real;
              VAR FwdConst:real; VAR DFV:PARAMETERS);
(* Allows you to input some or all of the variables used to calculate
the efficiency *)
 VAR   Entervalues : CHAR;
     DONE : BOOLEAN;
     P, K, Cst : real;
(* ..................................................... *)
```

```
PROCEDURE DfaultVals;
BEGIN   (* DfaultVals *)
 DFV[1]:= 1.0; DFV[2]:= 1.0; DFV[3]:= 1.0; DFV[4]:= 1.0; DFV[5]:= 1.0;
 DFV[6] := 0.57; DFV[7] := 0.0;  DFV[8] := 2.84; DFV[9] := 0.0;
 DFV[10] := 0.0; DFV[11] := 10.6E-6;  DFV[12] := 2.5915; DFV[13] := 2.616;
 DFV[14] := 2.7; DFV[15] := 2.7; DFV[16] := 0.029; DFV[17] := 0.0;
 DFV[18] := 125.3E-6; DFV[19] := DFV[16]/2;
 DFV[20] := (43e-12) * Sin(55.02*Pi/180); DFV[21] := 0.67*Pi/180;
 DFV[22] := 5.0; DFV[23] := 30000.0;  DFV[24]:=21.86E-9;
END;    (* DfaultVals *)

(* ..... *)

PROCEDURE TextBox(UpleftX, UpLeftY, LoRightX, LoRightY : integer);

const
  UpLfCh  = #201 ;   LoLfCh  = #200 ;
  UpRtCh  = #187 ;   LoRtCh  = #188 ;
  HorizCh = #205 ;   VertCh  = #186 ;

var
  X, Y, NumToDoX, CursorX, CursorY: integer;

begin
  if (UpLeftX >= LoRightX) or (UpLeftY >= LoRightY) or
        (UpLeftX < 1) or (LoRightX > mem[0:$44A]) or
        (UpLeftY < 1) or (LoRightY > 25) then
    exit;
  CursorX := wherex;
  CursorY := wherey;
  gotoxy(UpLeftX, UpLeftY);
  write(UpLfCh);
  NumToDoX := LoRightX - UpLeftX - 1;
  for X := 1 to NumToDoX do
    write(HorizCh);
  write(UpRtCh);
  for y:= UpLeftY + 1 to LoRightY - 1 do
    begin
      gotoxy(LoRightX, Y);
      write(VertCh);
      gotoxy(UpLeftX,Y);
      write(VertCh);
    end;
  gotoxy(UpLeftX, LoRightY);
  write(LoLfCh);
  for x := 1 to NumToDoX do
    write(HorizCh);
  write(LoRtCh);
  gotoxy(CursorX, CursorY)
end;

{ ..... }
```

```
PROCEDURE WriteEqus;
BEGIN   (* WriteEqus *)
 Clrscr;
 Writeln; Textcolor(Green);
 Writeln('Efficiency, ',CHR(252),', as function of the parameters defined below :');
 TextColor(White);
 Writeln(CHR(229),' = ',CHR(171),' b ',CHR(235),'k',
 '        b = confocal parameter = w',CHR(253),
 'k1      dephasing = ',CHR(235),'k');
 Writeln('                k1 = prop. const. inside    w = minimum spot size');
 Writeln(CHR(225),' = B/',CHR(251),CHR(21),'          B = ',CHR(171),
 ' p ',CHR(251),'(L k1)     p = walkoff angle in radians');
 Writeln(CHR(21),' = L/b           focussing parameter');
 Writeln(CHR(230),' = (L-2f)/L       f = focal position (Note Fig. 1)');
 Writeln('k = ',CHR(171),'(',CHR(224),'1 - ',CHR(171),' ',CHR(224),'2)b',
 '  ',CHR(224),'1 = abs.coef. @ w1      ',CHR(224),'2 = abs.coef. @ w2');
 Writeln('K = (2',CHR(251),'2 w',CHR(253),'d',CHR(253),'/c^3 n',CHR(253),
 CHR(238),'1)R   P = Peak power = Pavg / (',CHR(251),CHR(227),' v ',CHR(231),')');
 Writeln('                        v = pulse rep. freq.    ',
 CHR(231),' = char. time of pulse');
 TextColor(Cyan); Writeln('may be written as : '); TextColor(Green);
 Writeln('      ',CHR(252),'(',CHR(229),',',CHR(225),',k,',CHR(21),',',CHR(230),
 ') = K P L exp(-',CHR(224),''''L)  h(',CHR(229),',',CHR(225),',k,',CHR(21),
 ',',CHR(230),')');
 TextColor(Cyan);
 Writeln('where the Boyd & Kleinman focussing factor is defined by :');
 Textcolor(Green);
 Writeln('   h(',CHR(229),',',CHR(225),',k,',CHR(21),',',CHR(230),') = ',
 '(',CHR(227),CHR(253),'/',CHR(21),') exp(2',CHR(230),'k',CHR(21),') (2/',
 CHR(251),CHR(227),') ',CHR(244),' ',CHR(236),' ',CHR(179),'H(',CHR(229),
 ' + 4',CHR(225),'s,k,',CHR(21),',',CHR(230),')',CHR(179),CHR(253),
 ' exp(-4s',CHR(253),') ds');
 Writeln('                                    ',CHR(245),'-',CHR(236));
 TextColor(White);
 Writeln('Enter all parameters in SI units (MKS) :');
END;    (* WriteEqus *)

{ ..... }

PROCEDURE WriteValues;
VAR I : integer;
(* ..... *)
 PROCEDURE LineupChar;
 BEGIN (* LineupChar *)
  GOTOXY (7,18); Write(CHR(229),' = '); GOTOXY(24,18); Write('Lamb = ');
   GOTOXY (43,18); Write(' L = ');  GOTOXY(62,18); Write('   p = ');
  GOTOXY (7,19); Write(CHR(225),' = '); GOTOXY(24,19); Write('  n1 = ');
   GOTOXY (43,19); Write(CHR(235),'k = '); GOTOXY(62,19); Write('Pavg = ');
  GOTOXY (7,20); Write(CHR(21),' = '); GOTOXY(24,20); Write('  n2 = ');
   GOTOXY (43,20); Write(' w = '); GOTOXY(62,20); Write('   v = ');
  GOTOXY (7,21); Write(CHR(230),' = '); GOTOXY(24,21); Write('  ',CHR(224),'1 = ');
   GOTOXY (43,21); Write(' f = '); GOTOXY(62,21); Write('  ',CHR(231),' = ');
  GOTOXY (7,22); Write('k = '); GOTOXY(24,22); Write('  ',CHR(224),'2 = ');
   GOTOXY(43,22); Write('deff = ');
```

```
    GOTOXY(3,24); Write('K = '); GOTOXY(19,24); Write('P = ');
    GOTOXY(35,24); Write('C = ');
   END;  (* LineupChar *)
(* ..... *)
 PROCEDURE CalcVals (VAR Peak:Real; VAR KConst:Real; VAR LConst:Real);
 VAR cnter : integer;
    Db, b, alpha1, alpha2, rho : real;
 BEGIN
  b := Sqr(DFV[18])*2*Pi*DFV[12]/DFV[11];
  alpha1 := DFV[14] - DFV[15]/2;
  alpha2 := DFV[14] + DFV[15]/2;
  Db := DFV[21]*Sqrt(DFV[16]*2*Pi*DFV[12]/DFV[11])/2;
  KConst := 2*Sqrt(2)*Sqr((2*Pi*3E8/DFV[11])*DFV[20]/(DFV[13]*3E8));
  KConst := KConst/(8.8542E-12*3E8*DFV[11]);
  LConst := DFV[16]*exp(-alpha2*DFV[16]);
  Peak := DFV[22]/(Sqrt(Pi)*DFV[23]*DFV[24]);
  FOR cnter := 1 TO 5 DO BEGIN
   IF DFV[cnter] <> 1.0 THEN BEGIN
    CASE cnter OF
     1 : DFV[6] := b*DFV[17]/2;
     2 : DFV[7] := Db/Sqrt(DFV[8]);
     3 : DFV[8] := DFV[16]/b;
     4 : DFV[9] := (DFV[16] - 2*DFV[19])/DFV[16];
     5 : DFV[10] := alpha1*b/2;
    END;
   END;
  END;
  IF DFV[1] = 2.0 THEN
   DFV[6] := 1/DFV[8] * (exp(-Sqrt(DFV[8])/2) *  arctan(DFV[8]) +
          (1 - exp(-Sqrt(DFV[8])/2)) * 2 * arctan(DFV[8]/2));
 END;
(* ..... *)
 BEGIN      (* WriteValues *)
  Calcvals(P,K,Cst);
  FOR I := 1 TO 7 DO BEGIN
   GOTOXY(1,16+I); ClrEol End;
  TextColor(Red); TextBox(1,17,80,23);  TextColor(White);
  LineupChar;
  TextBackground(Black); TextColor(White);
  FOR I := 1 TO 5 DO BEGIN
   GOTOXY(3,17+I);
   CASE TRUNC(DFV[I]) OF
    0 : Write('C');
    1 : BEGIN
         TextBackground(Cyan); TextColor(Blue);
         Write('I'); GOTOXY (13,17+I); Write(DFV[5+I]:10:5);
         TextBackground(Black); TextColor(White);
        END;
    2 : Write('O');
    3 : Write('R');
   END;
   GOTOXY(13,17+I);
```

```
    IF DFV[I] <> 1.0 THEN Write(DFV[5+I]:10:5);
  END;
  TextBackground(Cyan); TextColor(Blue);
  GOTOXY(30,18); Write(DFV[11]:10); GOTOXY (49,18); Write(DFV[16]:10:5);
   GOTOXY(68,18); Write(DFV[21]:10:5);
  GOTOXY(30,19); Write(DFV[12]:10:5); GOTOXY (49,19); Write(DFV[17]:10:5);
   GOTOXY(68,19); Write(DFV[22]:10:3);
  GOTOXY(30,20); Write(DFV[13]:10:5); GOTOXY (49,20); Write(DFV[18]:10);
   GOTOXY(68,20); Write(DFV[23]:10:1);
  GOTOXY(30,21); Write(DFV[14]:10:5); GOTOXY (49,21); Write(DFV[19]:10:5);
   GOTOXY(68,21); Write(DFV[24]:10);
  GOTOXY(30,22); Write(DFV[15]:10:5); GOTOXY (49,22); Write(DFV[20]:10);
  TextBackground(Black); TextColor(White);
   GOTOXY(7,24); Write(K:10);
   GOTOXY(23,24); Write(P:10);
   GOTOXY(39,24); Write(Cst:10);
 END;       (* WriteValues *)
{ ..... }
 PROCEDURE GetKeys(VAR Complete:BOOLEAN);
 VAR  Arrows, Numbers, Direct, Characters : SETOFCHAR;
    TEMP : CHAR;
    X,Y,I : Integer;
 BEGIN    (* GetKeys *)
  DONE := False;
  Characters := ['I','i','C','c','O','o','R','r'];
  FOR I := 1 TO 5 DO BEGIN
   CASE TRUNC(DFV[I]) OF
    0 : TEMP := 'C';
    1 : TEMP := 'I';
    2 : TEMP := 'O';
    3 : TEMP := 'R';
   END;
   TEMP := GETCHAR(3,17+I,True,True,Characters,TEMP,TEMP);
   CASE TEMP OF
    'C' : DFV[I] := 0.0;
    'I' : BEGIN
          DFV[I] := 1.0;
          GetNumber(13,17+I,DFV[5+I]);
         END;
    'O' : DFV[I] := 2.0;
    'R' : DFV[I] := 3.0;
   END;
   WriteValues;
  END;
  FOR I := 1 TO 5 DO BEGIN
   GetNumber(30,17+I,DFV[10+I]);
   WriteValues;
  END;
  FOR I := 1 TO 5 DO BEGIN
   GetNumber(49,17+I,DFV[15+I]);
   WriteValues;
  END;
  FOR I := 1 TO 4 DO BEGIN
```

```
    GetNumber(68,17+I,DFV[20+I]);
    WriteValues;
   END;
   TextColor(Yellow);
   GOTOXY(51,24); Write('Done ? [Y/N] ');
   TEMP := GetChar(69,24,True,True,['Y','y','N','n'],'Y','Y');
   IF TEMP = 'Y' THEN  Done:=True;
   TextColor(White);
 END;     (* GetKeys *)
{ ..... }
 BEGIN     (* InputParms *)
  TextBackground(Black); TextColor(White);
  DfaultVals;
  WriteEqus;
  WriteValues;
  TextColor(Yellow);
  GOTOXY(42,16); Write('Input the values ? [Y/N] ');
  EnterValues := GETCHAR(70,16,True,True,['Y','y','N','n'],'Y','Y');
  TextColor(White);
  IF EnterValues = 'Y' THEN BEGIN
   REPEAT
    Getkeys(DONE)
   UNTIL DONE;
  END;
  FwdConst := P*K*Cst;
  Sigma := DFV[6];
  Beta :=  DFV[7];
  xi :=    DFV[8];
  mu :=    DFV[9];
  kappa := DFV[10];
 END;    (* InputParms *)
(* ---------- *)
 PROCEDURE CallInteg;
 (* Calls the numerical integration routines given the user inputs *)
 VAR  sigma, beta, B, xi, mu, kappa, h, FwdConst  : real;
    ok : char;
    DFV : PARAMETERS;
    Cycle : BOOLEAN;
    cnt : integer;
(* ..... *)
   PROCEDURE CycleThru;
   VAR cyclevar,numcycles,cyclecount : integer;
     upper, lower, tnum, range, spacing, cyclevalue, Effic : real;
     resultants : ARRAY[1..200] OF REAL;
   (*.....*)
```

```
PROCEDURE Getrange;
VAR j : integer;
BEGIN       (* GetRange *)
  FOR J := 1 TO 200 DO Resultants[J] := 0.0;
  TextColor(LightRed);
  GOTOXY(42,16); Write('                    ');
  GOTOXY(42,16);
  CASE cyclevar OF
    1 : Write ('Input range of values for ',CHR(229));
    2 : Write ('Input range of values for ',CHR(225));
    3 : Write ('Input range of values for ',CHR(21));
    4 : Write ('Input range of values for ',CHR(230));
    5 : Write ('Input range of values for k');
  END;
  Readln;
  numcycles := 1;
  GOTOXY(42,16); Write('                    ');
  TextColor(LightRed);
  GOTOXY(42,16); write('Lower = '); GetNumber (50,16,Lower);
  GOTOXY(42,16); Write('                    ');
  TextColor(LightRed);
  GOTOXY(42,16); write('Upper = '); GetNumber (50,16,Upper);
  GOTOXY(42,16); Write('                    ');
  TextColor(LightRed);
  GOTOXY(42,16); write('Number of points = ');
  GetNumber (62,16,tnum);
  IF ((tnum > 0.0) AND (tnum < 200.0)) THEN  BEGIN
    numcycles := Round(tnum);
    spacing := (Upper - Lower)/numcycles;  END
  ELSE spacing := (Upper - Lower);
  GOTOXY(42,16); Write('                    ');
  TextColor(Yellow);
  GOTOXY(42,16); write('Beginning the calculations ....  ');
  TextColor(White);
 END;       (* GetRange *)

(* . . . . . *)

PROCEDURE Saveresults;
VAR Saveit : Char;
  Savename,Tempstr : String60;
  DestFile : Text;
  j,multdelay : integer;
BEGIN       (* Saveresults *)
 TextColor(LightRed);
 GOTOXY(42,16); Write('                    ');
 GOTOXY(42,16); write('Save the results ? [Y/N] ');
 Saveit := GetChar(70,16,True,True,['Y','y','N','n'],'Y','Y');
 IF Saveit = 'Y' THEN BEGIN
  GOTOXY(42,16); Write('                    ');
  GOTOXY(42,16); write('Filename: ');
  Readln(Savename);
  Assign(DestFile,Savename);
  Rewrite(DestFile);
```

```
      CASE Cyclevar OF
        1 : TempStr := 'sigma varied';
        2 : Tempstr := 'beta varied';
        3 : Tempstr := 'kappa varied';
        4 : Tempstr := 'xi varied';
        5 : Tempstr := 'mu varied';
      END;
      Writeln(DestFile,TempStr);
      Str(Lower:10:5,Tempstr); Writeln(DestFile,'Lower = ' + TempStr);
      Str(Upper:10:5,Tempstr); Writeln(DestFile,'Upper = ' + TempStr);
      Str(Spacing:10:5,Tempstr); Writeln(DestFile,'Spacing = ' + TempStr);
      Str(numcycles,Tempstr); Writeln(DestFile,'Num.Pt.= ' + TempStr);
      Str(FwdConst:10:6,Tempstr); Writeln(DestFile,'Const = ' + TempStr);
      FOR j := 1 TO numcycles DO BEGIN
        Str(Resultants[j]:10:6,TempStr);
        Writeln(DestFile,TempStr);
      END;
      Close(DestFile);
    END;
    TextColor(White);
  END;      (* Saveresults *)
(* . . . . . *)
BEGIN      (* CycleThru *)
  Lower := 0.0; Upper := 1.0; tnum := 1.0;
  FOR cyclevar := 1 to 5 DO
    IF DFV[cyclevar] = 3.0 THEN BEGIN
      TextColor(LightRed);
      GetRange;
      cyclevalue := Lower;
      FOR cyclecount := 1 TO numcycles DO BEGIN
        CASE cyclevar OF
          1 : sigma := cyclevalue;
          2 : beta := cyclevalue;
          3 : xi := cyclevalue;
          4 : mu := cyclevalue;
          5 : kappa := cyclevalue;
        END;
        Romb(sigma,beta,xi,mu,kappa,-5,5,1E-04,1,h);
        cyclevalue := cyclevalue + spacing;
        h := (2/Sqrt(pi))*h*(pi * pi/xi)*exp(2*mu*kappa*xi);
        Effic := FwdConst*h;
        Effic := Effic/(1+Effic);   (* Accounts for Rsat *)
        Resultants[cyclecount] := Effic;
        GOTOXY(42,16); Write('                    ');
        GOTOXY(42,16); write('h = ',h:10:6);
        GOTOXY(58,16); write('Eff. = ',Effic:10:6);
      END;
      Saveresults;
    END;
  END;      (* CycleThru *)
(* ..... *)
```

```
 BEGIN  (* CallInteg *)
  Cycle := False;
  InputParms(sigma,beta,xi,mu,kappa,FwdConst,DFV);
  FOR cnt := 1 TO 5 DO
   IF DFV[cnt] = 3.0 THEN Cycle := True;
  GOTOXY(51,24); Write('                    ');
  TextColor(Yellow);
  GOTOXY(51,24); Write('Continue ? [Y/N] ');
  ok := GetChar(73,24,True,True,['Y','y','N','n'],'Y','Y');
  TextColor(White);
  IF ok = 'Y' THEN
   IF Cycle THEN CycleThru
    ELSE BEGIN
     Romb(sigma,beta,xi,mu,kappa,-5,5,1E-04,1,h);
     h := (2/Sqrt(pi))*h*(pi * pi/xi)*exp(2*mu*kappa*xi);
     GOTOXY(42,16); Write('                          ');
     write(CHR(BEEP));
     TextColor(LightRed);
     GOTOXY(42,16); write( h = ',h:10:6);
     GOTOXY(58,16); write('Eff. = ',FwdConst*h:10:6);
     TextColor(White);
    END;
 END;   (* CallInteg *)

(* ------------------------------------------------- *)

BEGIN    (* MAIN *)
 REPEAT
  ClrScr;
  CallInteg;
  GOTOXY(51,24); Write('                    ');
  TextColor(Yellow);
  GOTOXY(51,24); Write('Run again ? [Y/N] ');
  Continue := GETCHAR(73,24,True,True,['Y','y','N','n'],'Y','Y');
  TextColor(White);
 UNTIL Continue = 'N';
END.    (* MAIN *)

(* ------------------------------------------------- *)
```

Bibliography

1. Armstrong, J. A. *et al.* "Interactions between Light Waves in a Nonlinear Dielectric," *Physical Review*, 127(6): 1918-1939 (September 15, 1962).

2. Bevington, Philip R. *Data Reduction and Error Analysis for the Physical Sciences*. New York: McGraw-Hill Book Company, 1969.

3. Bhar, Gopal C. and G. C. Ghosh. "Temperature Dependent Phase-Matched Nonlinear Optical Devices Using CdSe and $ZnGeP_2$," *IEEE Journal of Quantum Electronics*, QE-16(8): 838-843 (August 8, 1980).

4. Boyd, G. D. and E. Buehler. "Linear and Nonlinear Optical Properties of $ZnGeP_2$ and CdSe," *Applied Physics Letters*, Volume 18, No. 7: 301-304 (April 1, 1971).

5. Boyd, G. D. and D. A. Klienman. "Parametric Interaction of Focussed Gaussian Light Beams," *Journal of Applied Physics*, Volume 39, No. 8: 3597-3639 (July 1968).

6. Boyd, Gary D. *et al.* "Linear and Nonlinear Optical Properties of Some Ternary Selenides," *IEEE Journal of Quantum Electronics*, QE-8, No. 12: 900-908 (December 12, 1972).

7. Butcher, Paul N. and David Cotter. *The Elements of Nonlinear Optics*. New York: Cambridge University Press, 1990.

8. Choy, Micheal M. and Robert L. Byer. "Accurate Second-order Susceptibility Measurements of Visible and Infrared Nonlinear Crystals," *Physical Review B*, Volume 14, No. 4: 1693-1706 (December 12, 1972).

9. *CRC Standard Math Tables, 28th Edition.* Edited by William H. Beyer. Boca Raton, Florida: CRC Press, Inc., 1988.

10. Eckardt, Robert C. *et al.* "Absolute and Relative Nonlinear Optical Coefficients of KDP, KD^*P, BaB_2O_4, $LiIO_3$, MgO:$LiNbO_3$, and KTP Measured by Phase-Matched Second-Harmonic Generation," *IEEE Journal of Quantum Electronics*, Volume 26, No. 5: 922-933 (May 1990).

11. Eckardt, Robert C. *et al.* "Efficient Second Harmonic Generation of 10 μm Radiation in $AgGaSe_2$," *Applied Physics Letters*, 47(8): 786-788 (October 15, 1985).

12. Eckardt, Robert C. *et al.* "High-average-intensity Nonlinear Infrared Frequency Conversion in $AgGaSe_2$," *Conference on Lasers and Electro-Optics, 1988 Technical Digest Series, Volume 7.* WM33 (April 25, 1988).

13. Eimerl, David. "High Average Power Harmonic Generation," *IEEE Journal of Quantum Electronics*, QE-23(5): 575-592 (May 1987).

14. Franken, P. A. et al. "Generation of Optical Harmonics," *Physics Review Letters*, Volume 7, No. 7: 118-119 (1961).

15. *Handbook of Mathematical Functions with Formulas, Graphs, and Mathematical Tables.* Edited by Milton Abramowitz and Irene A. Stegun. National Bureau of Standards, Applied Mathematics Series, No. 55, U. S. Government Printing Office, 1972.

16. Kildal, H. and Mikkelsen, J. C. "The Nonlinear Optical Coefficient, Phasematching and Optical Damage in the Chalcopyrite $AgGaSe_2$," *Optics Communications*, Volume 9, No. 3: 315-318 (November 1973).

17. Kleinman, D. A. *et al.* "Second-Harmonic Generation of Light by Focused Laser Beams," *Physical Review*, Volume 145, No. 1: 338-379 (6 May 1966).

18. McKelvey, John P. *Solid State and Semiconductor Physics*. Robert E. Malabar, Florida: Krieger Publishing Company, 1986.

19. Schepler, Kenneth L. and N. P. Barnes. "Nonlinear Optical Processes for the Mid-IR Region," *Laser Applications in Meteorology and Earth and Atmospheric Remote Sensing*, Edited by Martin M. Sokoloski, SPIE Proceedings No. 1062 (1989).

20. Suzaki, Yasuzi and Atsushi Tachibana. "Measurement of the μm sized Radius of Gaussian Laser Beam using the Scanning Knife-Edge," *Applied Optics*, Volume 14, No. 12: 2809-2810 (December 1975).

21. Wood, Elizabeth A. *Crystals and Light: An Introduction to Optical Crystallography. 2nd Edition.* Dover Publications, Inc. (1977).

22. Yariv, Amnon. *Optical Electronics*. New York: John E. Wiley & Sons, Inc., 1987.

23. Yariv, Amnon and Pochi Yeh. *Optical Waves in Crystals*. New York: John Wiley & Sons, Inc., 1984.

24. Yao, J. Q. and Theodore S. Fahlen. "Calculations of Optimum Phase Match Parameters for the Biaxial Crystal $KTiOPO_4$," *Journal of Applied Physics*, 55(1): 65-68 (January 1, 1984).

25. Zernike, Frits and John E. Midwinter. *Applied Nonlinear Optics*. New York: John E. Wiley & Sons, Inc., 1973.

26. Ziegler, Betsy C. and Kenneth L. Schepler. "Improved IR Transmission and Damage Threshold in $AgGaSe_2$," Submitted to *Applied Optics*, July 1990.

Vita

Captain Monte D. Turner was born on 11 December 1963 in Washington, D.C. He graduated from Northern High School in Owings, Maryland in 1981 and attended the U.S. Air Force Academy, graduating with a Bachelor of Science (specialty: Optical Physics) in June 1985. Upon graduation, he received a regular commission in the USAF and served his first tour of duty at Brooks AFB, Texas. He began as a Research Physicist for the School of Aerospace Medicine's Radiation Sciences Division where he conducted and directed research in the development of laser protective materials. His efforts led to the successful initiation of an extensive test program to characterize the standard for laser protective visors used in active duty units of the Air Force today. In December 1987 he was reassigned to the Air Force Astronautics Laboratory, Edwards AFB, California as a member of the Advanced Research in Energetic Systems branch. His responsibilities as a Manager, Energetic Physics Technology, included overseeing the basic research efforts in the development of novel rocket propellant concepts until entering the School of Engineering, Air Force Institute of Technology, in May 1989.

Permanent Address: 3191 Hunting Creek Road
Huntingtown, Maryland 20639

UNCLASSIFIED
SECURITY CLASSIFICATION OF THIS PAGE

REPORT DOCUMENTATION PAGE

Form Approved
OMB No. 0704-0188

1a REPORT SECURITY CLASSIFICATION: Unclassified	1b RESTRICTIVE MARKINGS
2a SECURITY CLASSIFICATION AUTHORITY	3 DISTRIBUTION/AVAILABILITY OF REPORT: Approved for Public Release Distribution Unlimited
2b DECLASSIFICATION/DOWNGRADING SCHEDULE	
4 PERFORMING ORGANIZATION REPORT NUMBER(S): AFIT/ENP/GEP/90D	5 MONITORING ORGANIZATION REPORT NUMBER(S)
6a NAME OF PERFORMING ORGANIZATION: Air Force Institute of Technology; 6b OFFICE SYMBOL (If applicable): ENP/GEP	7a NAME OF MONITORING ORGANIZATION
6c ADDRESS (City, State, and ZIP Code): Wright-Patterson AFB OH 45433-6583	7b ADDRESS (City, State, and ZIP Code)
8a NAME OF FUNDING/SPONSORING ORGANIZATION (In-house): Electro-Optics Sources Branch; 8b OFFICE SYMBOL (If applicable): WRDC/ELOS	9 PROCUREMENT INSTRUMENT IDENTIFICATION NUMBER
8c ADDRESS (City, State, and ZIP Code): WRDC/ELOS WPAFB OH 45433-6543	10 SOURCE OF FUNDING NUMBERS: PROGRAM ELEMENT NO 62204F; PROJECT NO 2001; TASK NO 05; WORK UNIT ACCESSION NO 01

11 TITLE (Include Security Classification)
Characterization of $AgGaSe_2$ and $ZnGeP_2$ for Frequency Doubling CO_2 Laser Output (Unclassified)

12 PERSONAL AUTHOR(S)
Monte D. Turner, Captain, USAF

13a TYPE OF REPORT	13b TIME COVERED	14 DATE OF REPORT (Year, Month, Day)	15 PAGE COUNT
Masters' Thesis	FROM _____ TO _____	1990 September	118

16 SUPPLEMENTARY NOTATION

17 COSATI CODES		
FIELD	GROUP	SUB-GROUP
20	05	
20	06	

18 SUBJECT TERMS (Continue on reverse if necessary and identify by block number)
$AgGaSe_2$, $ZnGeP_2$, CO_2 Laser, Frequency Doubling, Chalcopyrite, (JN)

19 ABSTRACT (Continue on reverse if necessary and identify by block number)

This experiment was to characterize the nonlinear performance of $AgGaSe_2$ and $ZnGeP_2$ for frequency doubling CO_2 laser output at 10.6 um. The experiments included a series of theoretical estimates of the source and crystal performance to define the measurements to be performed. The parameters of interest were the phase matching angles, angular acceptance, conversion efficiency and damage thresholds. The 9mmX9mmX29mm antireflection coated sample of $AgGaSe_2$, with a phase matching angle of θ=55.02°, and an internal acceptance bandwidth ($\Delta\theta$=0.298°, achieved a maximum second harmonic conversion efficiency of 20.5%. Surface damage limited the improvement of the efficiency and the threshold for the coated surface was near 4.5kW/cm . Further damage studies were conducted using small witness samples from the same crystal boule. For the case of the uncoated sample of $ZnGeP_2$, the theoretical computations pointed out that the performance would have been poor at best due to an extremely small effective nonlinear coefficient at the temperature tuned phase matching angles. These calculations are presented, though no output at 5.3 um was observed during these experiments. Improvements to the experimental designs and theoretical estimates

20 DISTRIBUTION/AVAILABILITY OF ABSTRACT	21 ABSTRACT SECURITY CLASSIFICATION	
☒ UNCLASSIFIED/UNLIMITED ☐ SAME AS RPT ☐ DTIC USERS	UL	
22a NAME OF RESPONSIBLE INDIVIDUAL: Capt Monte D. Turner	22b TELEPHONE (Include Area Code): (513)255-2012	22c OFFICE SYMBOL: AFIT/ENP

DD Form 1473, JUN 86 — Previous editions are obsolete — SECURITY CLASSIFICATION OF THIS PAGE

UNCLASSIFIED